



Implementation of a photovoltaic power diagnostic tool in the Meso-NH atmospheric model

CONFIDENTIAL REPORT

Master thesis

Environmental Sciences and Engineering – EPFL

Nicole LINDSAY

CNRM supervisor	Quentin LIBOIS
EPFL supervisor	Alexis BERNE
Master thesis period	11 September 2017 – 9 March 2018
Host laboratory	Météo-France/CNRM GMME Phy-NH 42, avenue Gaspard Coriolis 31057 Toulouse CEDEX 1 France
Submission date	5 March 2018

ACKNOWLEDGEMENTS

First, my special gratitude goes to Quentin LIBOIS for his insight and knowledge from which I have greatly benefited. His guidance throughout this master project has been precious to me.

I am also deeply grateful to Christine LAC for giving me the opportunity of performing this project in her research team. I would also like to thank her and Gaëlle DELAUTIER for their help with my Meso-NH simulations.

I am thankful to Alexis BERNE for following this project from a distance and guaranteeing a constant link with the EPFL.

My thanks also go to all the members of the PHY-NH and PRECIP corridor as well as all the PhD students at the CNRM, for their help, and most of all for their friendliness and kindness. I really enjoyed my time working at the CNRM and their company will surely be missed.

Last but not least, since this master thesis marks the end of long years of higher education, I would like to thank my family for their constant support.



ABSTRACT

With the current transition towards a more sustainable energy system, solar photovoltaics and more generally renewable energy sources have been gaining significance year by year. However, photovoltaic (PV) energy production, like many renewable energy sources, is highly dependent on weather conditions. Accurately predicting the photovoltaic power production is therefore becoming of the utmost importance, especially in remote locations, to ensure grid stability, reduce the risk of unreliability of electricity supply and enhance PV power penetration.

In this work, a PV model that converts atmospheric quantities into PV power has been developed. Although several processes are accounted for in the model, a special focus has been put on the impact of the spectral and angular distribution of incident radiation on photovoltaic performance. The model is aimed at being physically accurate and encompasses the modelling of irradiance transposition, optical losses and the impact of module temperature. Several options are offered to model certain processes, such that the determined default options are considered unless specified otherwise by the user. The flexibility of the PV model also means it can be applied to narrow- or broadband atmospheric model outputs or measurements, for any type of PV module and in any geometrical configuration, provided detailed characteristics of the module are available.

The evaluation of the model has been carried out thanks to exhaustive atmospheric and PV measurements performed on the SIRTA site in June and December 2017. Simulations based on the measured atmospheric conditions lead to a mean relative error in PV power of 0.2% in June and 3.7% in December for the monocrystalline silicon module installed on site, whereas a commonly used simple model leads to 3.4% and 8.4% error for the same months.

The role of spectral and angular properties of radiation have then been further investigated with the validated PV model. It has been shown that the presence of clouds can increase PV performance by up to 5%. Also, the deterioration of the spectral resolution of the irradiance input has been found to change the PV power by 10.8% in overcast conditions compared to a reference with fourteen bands. More generally, global horizontal irradiance which is output by atmospheric models is proven to be far from sufficient for accurate PV modelling, highlighting the need for spectrally resolved inputs.

Last, the performance of the coupled Meso-NH – PV model has been evaluated at the SIRTA in June 2017, resulting in an error of 1.5% in clear-sky and 13.8% in all sky conditions. Further analysis has shown that clouds in Meso-NH are poorly represented and overall too optically thin. Errors in clear-sky conditions could be explained by the use of inappropriate climatologies for aerosols and ozone, or by caveats in the radiative transfer model.

The results of the developed PV model coupled with Meso-NH pave the way for improved PV power forecasting at Météo-France. New prospects have also arisen, for research thanks to the potential use of PV power for data assimilation, and for operational purposes, where climatologies can be used to design PV potential atlases and help planning PV farms development.

Key words: photovoltaic power, numerical weather prediction, radiative transfer, cloud-radiation interactions, *in situ* radiation measurements.

RÉSUMÉ

Avec la transition vers un système énergétique plus durable, le solaire photovoltaïque (PV), et les sources d'énergie renouvelable en général, ne cessent de gagner en importance. Toutefois, la production PV, tout comme la plupart des énergies renouvelables, dépend fortement des conditions météorologiques. Or, la capacité à prévoir précisément la production PV devient cruciale, surtout dans les endroits reculés, afin de garantir la stabilité du réseau, améliorer la fiabilité de l'approvisionnement en électricité et accroître la pénétration de la puissance PV.

Dans le cadre du présent travail, un modèle PV convertissant les grandeurs atmosphériques en puissance PV a été développé. Ce modèle tient compte de nombreux phénomènes, et se concentre en particulier sur l'impact de la distribution spectrale et angulaire du rayonnement incident sur la performance PV. Le modèle vise à être au plus proche de la physique et comprend la modélisation de la transposition de l'irradiance, les pertes optiques et les effets de la température du module. Plusieurs options sont offertes pour modéliser certains processus, mais en l'absence de choix de l'utilisateur, un paramétrage par défaut est appliqué. Le modèle PV peut fonctionner à partir de mesures ou de sorties de modèles atmosphériques à bandes étroites ou larges, pour tous types de panneaux et dans toutes configurations géométriques.

L'évaluation du modèle a été menée grâce aux mesures atmosphériques et PV exhaustives effectuées sur le site du SIRTA en juin et décembre 2017. Les simulations basées sur ces mesures atmosphériques mènent à une erreur relative moyenne en puissance de 0.2% en juin et 3.7% en décembre pour le module en silicium monocristallin installé sur site, tandis qu'un modèle simple couramment utilisé aboutit à 3.4% and 8.4% d'erreur pour les mêmes mois.

Le rôle des propriétés spectrales et angulaires du rayonnement a aussi été investigué avec le modèle PV validé. Il a été constaté que la présence de nuages peut augmenter la performance PV de 5% et que le passage de quatorze bandes spectrales à une pour l'irradiance en entrée de modèle peut modifier la puissance PV de 10.8% en ciel nuageux. Plus généralement, il a été montré que l'irradiance globale horizontale en sortie des modèles atmosphériques ne suffit pas pour une modélisation PV précise, d'où le besoin de sorties à résolution spectrale plus fine.

Enfin, la performance du modèle couplé Meso-NH – PV a été évaluée au SIRTA en juin 2017, et une erreur de 1.5% en ciel clair et 13.8% en ciel quelconque ont été observées. Une analyse plus poussée montre que les nuages dans Meso-NH sont mal représentés et leur épaisseur optique est globalement sous-estimée. Les erreurs par ciel clair pourraient s'expliquer par l'utilisation de climatologies inappropriées pour les aérosols et l'ozone, ou par des défauts du modèle de transfert radiatif.

Les résultats du modèle PV développé couplé avec Meso-NH ouvrent la voie à l'amélioration de la prévision de puissance PV chez Météo-France. De nouvelles perspectives ont également émergé, que ce soit pour la recherche grâce à l'utilisation potentielle de la puissance PV pour l'assimilation de données, ou pour l'opérationnel où les climatologies peuvent servir à concevoir des atlas de potentiel PV ou aider à la planification de nouveaux parcs PV.

Mots clés: puissance photovoltaïque, prévision numérique du temps, transfert radiatif, interactions nuages-rayonnement, mesures in situ du rayonnement.

CONTENTS

Acknowledgements	iii
Abstract	v
Notations	xvii
1. Introduction	1
1.1. Background	1
1.1.1. Context	1
1.1.2. Forecasting methods	1
1.2. Research project objectives	3
1.2.1. Motivation	3
1.2.2. Challenges for physical PV models	4
1.2.3. Strategy of the present work	5
1.3. Research methodology	6
2. Theoretical background	9
2.1. Basics in atmospheric radiation	9
2.1.1. Solar spectrum	9
2.1.2. Mechanisms affecting the available solar radiation at the surface	10
2.1.3. Direct and diffuse irradiance	11
2.2. Theory of photovoltaics	12
2.2.1. Photovoltaic devices	12
2.2.2. Ideal equivalent solar cell circuit	14
2.2.3. Short circuit density and open circuit current	15
2.2.4. Maximum power point and fill factor	16
2.2.5. Equivalent solar cell circuit with a series and shunt resistance	16
2.2.6. Current and density current	17
2.2.7. Influence of the incoming radiation: photocurrent, spectral response and quantum efficiency	17
2.2.8. Influence of the temperature	19
2.2.9. Reference conditions	20
2.2.10. From solar cells to modules and arrays	21
2.3. Impact of the spectral and angular distributions of incident radiation on photovoltaic performance	22
2.3.1. With <i>in situ</i> observations	22
2.3.2. With radiative transfer simulations	23

3. Tools and data	27
3.1. Radiative transfer models	27
3.1.1. The MODerate resolution atmospheric TRANsmission (MODTRAN)	27
3.1.2. ecRad	27
3.2. Assessing the optical thickness of clouds	28
3.3. The Meso-NH atmospheric model	31
3.4. Available data	32
3.4.1. Measurements on the SIRTA site	32
3.4.2. PV module manufacturer’s datasheet	33
4. Photovoltaic production modelling	35
4.1. Main components of PV modeling	35
4.2. Description of the subcomponents and the different options available	37
4.2.1. Cell-impacting irradiance	37
4.2.2. Spectral response	42
4.2.3. Cell temperature	43
4.2.4. Series resistance	43
4.3. Overview	43
5. Validation of the photovoltaic model	47
5.1. Calibration and evaluation of the PV model	47
5.1.1. Methodology	47
5.1.2. Cell-incident irradiance calibration	48
5.1.3. Cell temperature modelling calibration	53
5.1.4. From irradiance and temperature to power calibration	57
5.1.5. Evaluation of the overall code	63
5.1.6. Summary of the default options	65
5.2. Validation over a winter month : example of December 2017	65
6. Further investigation of the spectral and angular effects on PV performance	67
6.1. Impact of clouds on PV performance	67
6.1.1. Influence of clouds on the radiation incident on a tilted surface	67
6.1.2. ecRad simulations coupled with the PV model	67
6.1.3. Observed phenomena	70
6.2. Influence of the spectral resolution of the irradiance input	71
6.3. Comparison with a simple PV model	73
7. The coupled Meso-NH – PV model	77
7.1. Method	77
7.1.1. The grid – PREP_PGD step in MESO_NH	77
7.1.2. Initial and boundary conditions – PRE_REAL_CASE step in MESO_NH	78
7.1.3. Meso-NH simulation – MESO_NH step in MESO_NH	78
7.1.4. Coupling method	79
7.2. Accuracy of the coupled model	79
7.3. Sources of error in Meso-NH simulations	81
7.3.1. Clear-sky conditions	82

7.3.2. All conditions	83
8. Conclusion	87
8.1. Synthesis	87
8.2. Outlook	88
Bibliography	90
A. Cloud optical thickness from the physical properties of clouds	97
A.1. Deriving the optical thickness physical expression	97
A.2. Deriving the liquid water content from the liquid water mixing ratio	97
B. Review of PV technologies	99
B.1. First generation technologies	99
B.1.1. Monocrystalline silicon m-Si	99
B.1.2. Polycrystalline silicon p-Si (or multicrystalline silicon mc-Si)	99
B.1.3. Thin films	100
B.1.4. Amorphous silicon (a-Si)	100
B.1.5. Micro-amorph silicon (a-Si/ μ c-Si)	100
B.1.6. Cadmium telluride (CdTe)	100
B.1.7. GaAs	101
B.1.8. Copper indium selenide (CIGS) and copper, indium gallium dieseline (CIS)	101
B.1.9. Thin film c-Si, pc-Si	101
B.2. Third generation	101
B.2.1. Organic cells	101
B.2.2. Dye-Sensitized Solar Cells (DSSC)	102
C. SIRTA dataset	103
D. PV model: scientific documentation	105
D.1. Main components of PV modeling	105
D.2. Modelling the cell-impacting irradiance	105
D.2.1. Spectralisation	105
D.2.2. Transposition models	109
D.2.3. Optical losses	115
D.3. Cell temperature	121
D.3.1. A simplified approach to steady-state energy balance	121
D.3.2. Considered temperature models	121
D.3.3. Detailed temperature models	122
D.4. Spectral response and cell photocurrent in STC conditions	124
D.5. Photocurrent	125
D.6. Operating power	125
D.6.1. Computing V_{OC} for different temperatures and irradiances to STC conditions	125
D.6.2. Fill factor	126
D.7. Series resistance	127
D.8. Overview	128

E. Further into the validation of cell temperature models	129
E.1. Converting wind speeds for the King model	129
E.2. Adapting the NOCT for the Skoplaki model	130

LIST OF FIGURES

1.1.1.	Model classification based on spatial and temporal resolution, taken from <i>Diagne et al.</i> (2013)	2
2.1.1.	Global energy budget of the Earth	10
2.1.2.	Top-of-atmosphere and ground-level solar spectra, simulated by MODTRAN for US Standard Atmosphere 1976, and absorption bands of water vapour and ozone following <i>Liou</i> (2002)	10
2.1.3.	Imaginary part of the complex refractive index and corresponding absorption coefficient of ice and water	11
2.1.4.	Direct and diffuse solar spectra normalised over the shortwave domain, simulated with MODTRAN considering US Standard Atmosphere 1976 and Solar Zenith Angle $SZA = 48.2^\circ$	12
2.2.1.	The photovoltaic effect	13
2.2.2.	PV technologies	13
2.2.3.	Best lab cells and modules efficiency depending on the technology. Graph taken from <i>Fraunhofer Institute for Solar Energy Systems</i> (2017) using data from <i>Green et al.</i> (2017)	13
2.2.4.	Equivalent ideal circuit of a solar cell	14
2.2.5.	(a) I-V curve and (b) operating point defined by the resistive load and the I-V curve	15
2.2.6.	More realistic equivalent circuit of a solar cell.	16
2.2.7.	Typical and ideal external quantum efficiency, http://www.pveducation.org/	18
2.2.8.	Real and ideal spectral response for different PV technologies	19
2.2.9.	Influence of temperature on the I-V curve (solid) and P-V curve (dotted)	20
2.2.10.	PV cell, module, string and array illustration	21
2.2.11.	I-V curve for cells in series and in parallel	21
2.3.1.	Observed module power as a function of (a) measured global horizontal or (b) POA irradiance. The power in (c) is corrected by $(1 - C_{T,P_{MPP}} \cdot (T_c - T_{c,STC}))$ to account for the expected influence of the temperature.	22
2.3.2.	Ratio of the irradiance measured by the spectrometer (300–1050 nm) and the pyranometer (200 – 3600 nm) on the SIRTA site over the month of June 2017.	23
2.3.3.	Atmospheric transmittance (global) and partition into direct and diffuse irradiance as a function of cloud optical thickness, simulated with ecRad.	24
2.3.4.	Global horizontal irradiance at the surface as a function of optical depth in the shortwave band and in the wavelength band absorbed by a silicon cell.	24
2.3.5.	Normalised spectral irradiance for a clear and cloudy-sky	25
3.2.1.	Retrieved optical thickness as a function of the optical thickness computed from the physical properties of the cloud for various SZA with ecRad simulations	30

3.2.2.	Retrieved optical thickness from the transmittance per ecRad band as a function of the optical thickness computed from the physical properties of the cloud for various SZA.	31
3.4.1.	Instruments localisation, adapted from SIRTA.	32
4.1.1.	Simplified diagram of the PV code	36
4.2.1.	MODTRAN-simulated spectra considering the USSA conditions with SZA varying between 10 and 80° and the same spectra normalised by their integral between 200nm and 1100nm.	38
4.2.2.	Global spectral irradiance for different wavelengths and solar zenith angles.	38
4.2.3.	Spectralisation method for a global irradiance. The example for an irradiance measured over 200-1100nm is given.	39
4.2.4.	Spectralisation method for given spectral irradiance. The dotted lines correspond to the different bands measured	39
4.2.5.	Contribution of direct, diffuse and ground-reflected irradiance to POA irradiance	40
4.2.6.	Different subcomponents of the sky-scattered irradiance and beam irradiance	40
4.2.7.	Ideal, real and modelled quantum efficiency of a solar cell.	42
4.3.1.	Detailed diagram of the PV code	44
4.3.2.	Structure of the user-friendly version of the PV model	45
5.1.1.	Measurements available from the SIRTA in June 2017 for the PV model evaluation and calibration.	47
5.1.2.	Methodology used to assess the accuracy of spectralisation method.	49
5.1.3.	Comparison of the 10 minute-averaged measured spectral irradiance by the SIRTA on June 10 2017 at noon and the spectral irradiance deduced from the measured GHI and DHI by MODTRAN-spectralisation of direct and diffus components brought to the same spectral resolution as the measurements.	49
5.1.4.	Methodology used to assess the accuracy of the transposition models.	50
5.1.5.	Errors in POA irradiance modelling for different SZA.	51
5.1.6.	Absorption-transmission coefficient for the beam, sky-scattered and ground-reflected components considering the four optical losses methods	52
5.1.7.	Modelled transmitted irradiance to the solar cell normalised to STC conditions for different methods considering the MODTRAN-equivalent ASTM G173-03 spectrum. Refer to the colour legend of the previous figure.	52
5.1.8.	Methodology used to assess the accuracy of T_c models.	53
5.1.9.	Modelled versus measured module temperature (FranceWatts monocrystalline module) depending on the empirical coefficients provided by <i>King et al.</i> (2004). The numbering corresponds to the rows in Table D.3.1.	54
5.1.10.	Error in module temperature as a function of the date, air temperature, wind speed and plane-of-array irradiance with the optimal King parameters (FranceWatts monocrystalline module)	55
5.1.11.	Modelled versus measured module temperature (FranceWatts monocrystalline module) depending on the Skoplaki model.	56
5.1.12.	Modelled cell temperature versus the measured temperature for the different models considered for the France Watts module.	56
5.1.13.	Methodology used for validating the I_{SC} modelling	57

5.1.14. Simulated and measured I_{SC} of the module on a clear-sky and cloudy day . . .	58
5.1.15. Difference between the simulated and measured I_{SC} on a clear-sky and cloudy day with trapezoidal quantum efficiencies	59
5.1.16. Methodology used for validating the V_{OC} modelling.	59
5.1.17. Simulated and measured V_{OC} of the module on a clear-sky and cloudy day . . .	60
5.1.18. Methodology used for validating the FF modelling.	60
5.1.19. Simulated and measured FF of the module on a clear-sky and cloudy day	61
5.1.20. Simulated and measured FF on a clear-sky day (10 June 2017), including a method accounting for the temperature dependance of the series resistance. . .	61
5.1.21. Methodology used to assess the accuracy of the power, with the I_{SC} modelled following Figure 5.1.13	62
5.1.22. Simulated and measured P of the module on a clear-sky and cloudy day with measured T_c and corrected POA	63
5.1.23. Simulated and measured P of the module on a clear-sky and cloudy day considering the measured module temperature. All variables are simulated and cascaded down except the cell temperature.	64
5.1.24. Simulated and measured P of the module on a clear-sky and cloudy day. All variables are simulated.	64
5.1.25. Modeled versus measured module temperature (FranceWatts monocrystalline module): comparison between the simple model and the King model (module temperature).	65
5.2.1. Density function of the modelled power as a function of the measured power . .	66
6.1.1. Simulation protocole	68
6.1.2. Efficiency of monocrystalline solar cell as a function of the cloud optical thickness and SZA.	68
6.1.3. Variation in effective POA irradiance with optical thickness and solar zenith angle. .	69
6.1.4. Contribution of the beam radiation in the overall POA irradiance.	69
6.1.5. Normalised irradiance over 200–2500nm for SZA = 1 or 60° and $\tau = 0$	70
6.1.6. Measured efficiency as a function of the optical depth deduced from measurements	70
6.2.1. Illustration of the incoming irradiance integrated over each band for different levels of knowledge	71
6.2.2. Relative error in modelled power with varying SZA and τ for the 7-band, 1-band and 1-band global inputs	72
6.2.3. Direct and diffuse irradiance normalised over the SW domain from MODTRAN and ecRad for the clear-sky USSA and SZA = 30°C	73
6.3.1. Relative error in modelled power with the newly developed versus a classical model. The grey zone represents the region where the developed models performs better.	74
6.3.2. Measured and modelled module power with newly developed or classically used PV model	75
7.1.1. Grid setup for Meso-NH simulations	77
7.2.1. Modeled (Meso-NH + PV) versus measured power in June at the SIRTAs	80
7.2.2. Measured and modeled by the coupled MesoNH-PV model from 10 to 20 June at the SIRTAs	80

7.2.3.	Measured and modeled power with the coupled MesoNH-PV model for June 2 and 3 at the SIRTA	80
7.2.4.	Relative error in power as a function of the modelled total cloud cover and optical thickness from Meso-NH simulations.	81
7.3.1.	Modeled (Meso-NH + PV) versus measured power and irradiance under clear-sky conditions in June at the SIRTA. Each square has a resolution of 5 W for the power and 10 W m^{-2} for the irradiances	82
7.3.2.	Modeled (Meso-NH + PV) versus measured spectral irradiance under clear-sky conditions in June at the SIRTA, with a resolution of 5 W m^{-2}	83
7.3.3.	Modeled (MesoNH + PV) versus measured irradiance for all sky conditions in June at the SIRTA. Each square has a resolution of 20 W m^{-2} for the irradiances	84
7.3.4.	Modeled optical thickness from Meso-NH simulations and from observations for all sky conditions in June at the SIRTA. Each square has a resolution of 0.25	85
7.3.5.	Modeled (MesoNH + PV) versus measured temperature and windspeed at 2m for all sky conditions in June at the SIRTA. Each square has a resolution of $0.5 \text{ }^\circ\text{C}$ or 0.1 m s^{-1}	85
D.1.1.	Simplified diagram of the PV code	106
D.2.1.	MODTRAN-simulated spectra considering the USSA conditions with SZA varying between 10 and 80° and the same spectra normalised by their integral between 200nm and 1100nm.	107
D.2.2.	Global spectral irradiance for different wavelengths and solar zenith angles.	107
D.2.3.	Spectralisation method for a global irradiance. The example for an irradiance measured over 200-1100nm is given.	108
D.2.4.	Spectralisation method for given spectral irradiance. The dotted lines correspond to the different bands measured	108
D.2.5.	Parameters defining the position of the sun and the orientation of the photovoltaic panel, adapted from <i>Duffie & Beckman (2013)</i>	109
D.2.6.	Different subcomponents of the sky-scattered irradiance	110
D.2.7.	Notations used for deriving the 2D and 3D isotropic diffusion formulation, adapted from <i>Badescu (2002)</i>	113
D.2.8.	Angles of incidence and refraction, adapted from <i>Krauter & Hanitsch (1996)</i>	116
D.2.9.	Angles of incidence and refraction in a “three slab optical system” of a Si solar cell	116
D.2.10.	Transmission coefficients relative to STC as a function of angle of incidence for different wavelengths, (<i>Sjerps-Koomen et al. 1996</i>)	117
D.2.11.	Transmission coefficient relative to STC as a function of the angle of incidence for the simple air-glass and more complex “three-slab-layer” models, (<i>Sjerps-Koomen et al. 1996</i>)	117
D.2.12.	Coefficient de transmission relatif aux STC (standard test conditions) en fonction de l’angle d’incidence selon différentes méthodes, (<i>Sjerps-Koomen et al. 1996</i>)	118
D.2.13.	Effective beam radiation incidence angle of sky-scattered and ground-reflected irradiances on a tilted surface	120
D.4.1.	Ideal, real and modelled quantum efficiency of a solar cell.	124
D.8.1.	Detailed diagram of the PV code	128

- E.1.1. Modeled module temperature for different values of α and corresponding bias and standard deviation. 129
- E.2.1. Errors in cell temperature modelling using Skoplaki 2 model over a range of NOCTs. 130
- E.2.2. Errors in cell temperature modelling using Skoplaki 2 model, without (a) or with (b) $\Delta\text{NOCT} = 10^\circ\text{C}$ 131

LIST OF TABLES

2.2.1.	Main PV technologies : advantages and drawbacks	14
2.2.2.	Energy band gap E_{gap} (<i>Dupré et al.</i> 2016) and λ_{gap} of different solar cells.	18
3.1.1.	Wavelength and wavenumber of the 14 SW bands in ecRad	28
3.3.1.	The six SW bands of the radiative transfer model currently used in Meso-NH	31
3.4.1.	Variables commonly provided by the manufacturer’s datasheet	33
4.3.1.	Available options in the developed PV model	45
5.1.1.	MRE and RMSE due to spectralisation	49
5.1.2.	Error in G_{POA} for the different transposition methods, for $G_{\text{POA,meas}} > 200 \text{ W m}^{-2}$	50
5.1.3.	Bias and standard deviation in module temperature for the six sets of King parameters and all four modules. The mount type numbering (1 to 6) refers to the rows in Table D.3.1	54
5.1.4.	Bias and standard deviation in cell temperature for the four Skoplaki models and all four modules.	55
5.1.5.	Error in I_{SC} of the module for the different optical losses methods.	58
5.1.6.	Error in V_{OC} of the module for the two formulations.	60
5.1.7.	Error in FF of the module for the two fill factor expressions.	61
5.1.8.	Error in P of the module by using the simulated I_{SC} , V_{OC} , FF. The nominal power of the panel is 250 W.	62
5.1.9.	Error in I_{SC} , V_{OC} , FF and P of the module by using all simulated variables except the cell temperature. The nominal power of the panel is 250W.	63
5.1.10.	Error in P of the module by using all simulated variables. The nominal power of the panel is 250W.	64
5.1.11.	Options applied by default in the PV model	65
7.1.1.	SIRTA site location	77
C.0.1.	Installed instruments, corresponding variables and accuracies	104
D.2.1.	Discrete sky clearness categories (<i>Perez et al.</i> 1990)	113
D.2.2.	Empirical values f_{ij} depending on the clearness category defined Table D.2.1 found in <i>Perez et al.</i> (1990)	113
D.3.1.	Empirically determined a , b and ΔT coefficients for given module-types and mounts, (<i>King et al.</i> 2004)	124
E.1.1.	Optimised α for the different modules, based on the optimisation criteria (bias or standard deviation).	129
E.2.1.	Optimised ΔNOCT for the different modules, based on the optimisation criteria (bias or standard deviation).	130

NOTATIONS

arr	Array
ASTM	American Society for Testing Materials – referring to the ASTM G173-03 solar spectrum
<i>b</i>	Beam or direct
<i>c</i>	Cell
<i>d</i>	Diffuse or scattered
DHI	Diffuse Horizontal Irradiance
DNI	Diffuse Normal Irradiance
FF	Fill Factor
GHI	Global Horizontal Irradiance
<i>i</i>	Incident
mod	Module
MPP	Maximum Power Point
MRE	Mean Relative Error
NOCT	Normal Operating Cell Temperature
NTE	Nominal Terrestrial Environment
OC	Open Circuit
POA	Plane-Of-Array (normal to the PV module)
PV	Photovoltaic
<i>r</i>	Refracted
ρ	Ground reflected
RMSE	Root Mean Square Error
SAA	Solar Azimuth Angle
SC	Short Circuit
STC	Standard Test Conditions
str	String
SW	Shortwave
SZA	Solar Zenith Angle
TOA	Top-Of-Atmosphere

PART 1

INTRODUCTION

1.1 Background

1.1.1 Context

With the increasing energy demand and the necessity of reducing fossil fuel consumption, energy production is turning towards renewable energy sources. Renewables thus represented two-thirds of new electricity capacity installed in 2016 (*IEA 2017*). Solar photovoltaic (PV) capacity grew from 228 to 303 GW worldwide between 2015 and 2016, meaning that the installation of new PV capacity soared by 50% in a year (*REN21 2017*), representing the source of energy with the highest net energy growth, even overtaking coal. Solar PV energy is therefore expected to represent the renewable energy with the largest capacity evolution in the upcoming years. However, as most renewable energy sources, PV production is highly dependent on weather conditions, which is an issue from several perspectives. First, an accurate prediction of the PV potential during the development phase can minimize the investment risk. Furthermore, grid stability requires a balance between the electricity supplied and consumed. Yet, ensuring this stability is becoming more and more challenging with the current transition towards decentralised energy production, where production has to be adapted to consumption on a smaller scale. An accurate production forecast would allow PV energy to be more reliable and thus be better integrated in these so-called “smart-grids”. Furthermore, if independent system operators and utilities are interested in solar power forecasts, producers are also concerned when negotiating power purchase agreements (*Kostylev & Pavlovski 2011*). Indeed, in certain countries – such as France since the “Loi relative à la transition énergétique pour la croissance verte” (Law relative to energy transition for green growth) adopted in 2015 – renewable energy is traded on the power market, and producers face penalties in case of imbalance between the contracted and delivered energy. PV production forecasting has therefore great economic repercussions though these are not necessarily easy to assess (*Antonanzas et al. 2016, 2017*). This economic interest in accurate PV power forecasting has thus motivated research on the topic and is at the origin of start-ups (like SteadySun or Reuniwatt in France) who are tackling this issue.

1.1.2 Forecasting methods

Different time-scales can be used for photovoltaic power forecasting and have different applications (*Kostylev & Pavlovski 2011*):

1. Intra-hour – from a few minutes to two hours ahead with second to 5-minute resolution, *e.g.* variability related to real-time grid operations;
2. Hour-ahead – from one hour to several hours ahead with an hourly resolution, *e.g.* for load dispatch and real-time grid operation;

3. Day-ahead – from one day to three days ahead with an hourly resolution, *e.g.* for transmission scheduling, day ahead markets, switching sources, programming backup, planning reserve usage;
4. Medium-term forecasting – from a week to two months ahead with a daily-resolution, *e.g.* planning, asset optimisation, risk assessment;
5. Long term forecasting – from one to several years with monthly or yearly resolution, *e.g.* for resource assessment, feasibility study during the design of the photovoltaic farm, bankable documentation, optimal operating costs.

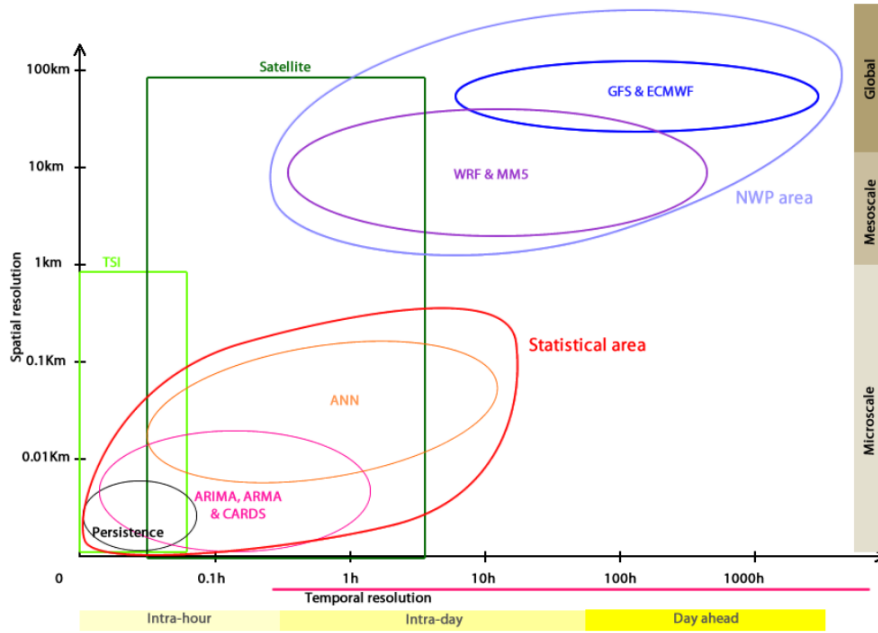


Figure 1.1.1: Model classification based on spatial and temporal resolution, taken from *Diagne et al. (2013)*

When PV forecasting, the primary focus is on accurately forecasting the solar irradiance, as it is a critical but highly variable parameter (due to clouds in particular). Different methods can be used depending on the horizon of forecast and can be categorized into seven types (*Kostylev & Pavlovski 2011, Diagne et al. 2013, Antonanzas et al. 2016, Das et al. 2018*) as shown in Figure 1.1.1:

- The persistence method is the simplest and most economical method, it assumes that the forecast variables are similar to the current ones (no change assumption). The accuracy in forecast therefore rapidly decreases with time as cloudiness evolves. This method is generally considered as inaccurate for more than one-hour ahead forecasting and is commonly used as a reference to assess the performance of commercial forecast models.
- Total Sky Imagery (TSI) or ground-based sky imagery considers sky images taken from the ground to estimate upcoming radiation. Images are analysed to detect the presence of clouds on each pixel and the cloud motion vector is computed by cross-correlating consecutive images. One of the main issues is to go beyond distinguishing clear and cloudy sky by differentiating between thin and opaque clouds (*Inman et al. 2013*). This method allows high spatial and temporal resolution and is mainly used for timescales shorter than five minutes.

- Satellite-based forecasting methods process cloud cover imagery to estimate the solar radiation reaching the surface. It is for instance the case of the Heliosat methods, which started more than 30 years ago ([Cano et al. 1986](#)). The latest version, Heliosat-4, assesses the direct and diffuse components of the downwelling shortwave irradiance reaching the ground by combining a clear-sky model and a overcast-sky model ([Qu et al. 2017](#)). Both models are based on look-up tables built with the libRadtran radiative transfer model ([Mayer & Kylling 2005](#)). Satellite-based forecasting methods in general perform better than the persistence and NWP-based methods from one to six hours ahead.
- Statistical methods include approaches such as Autoregressive (AR), Moving Average (MA), ARMA or AR Integrated MA (ARIMA) models ([Diagne et al. 2013](#), [Antonanzas et al. 2016](#), [Das et al. 2018](#)). Such statistical methods rely on historical data to deduce a site-dependent relationship between a set of input variables and the expected output. Past and present observations then allow to predict for the future radiation reaching the ground.
- Machine learning models and artificial intelligence (AI) techniques can handle linear or non-linear and non-stationary data patterns ([Diagne et al. 2013](#), [Antonanzas et al. 2016](#), [Das et al. 2018](#)). AI methods are benefiting from the recent development of this field and enable to find hidden dependencies between different variables through a training process.
- Numerical Weather Prediction (NWP) based models can provide solar radiation forecasts thanks to a physical description of the atmosphere and the site. Forecasts from mesoscale models (WRF ([Skamarock et al. 2005](#)), MM5 ([Grell et al. 1994](#)), *etc.*) or global weather models are used. This method is known to be optimal for forecasts from 6 hours and longer ([Kostylev & Pavlovski 2011](#), [Diagne et al. 2013](#)).
- Hybrid methods consist in a combination of two or more of the previous methods. By using the advantages of each method, an optimal forecast should be achieved. For instance, NWP outputs can be post-processed by statistical or AI methods to counterbalance models biases.

Two main methodologies can therefore be distinguished for photovoltaic power forecasting: a one-stage approach where PV power is directly computed from atmospheric conditions, or a two-stage approach where relevant quantities are computed then fed into a photovoltaic model ([Antonanzas et al. 2016](#), [Jimenez et al. 2016](#)). One-stage approaches typically consist in AI or statistical methods that do not necessarily explicitly calculate the physically relevant atmospheric conditions. A two-step approach on the other hand consists in coupling one of the methods mentioned above to accurately assess the solar irradiance with a photovoltaic model. The latter can either be based on physical modelling or on statistical or AI methods simulating the response of the photovoltaic module.

1.2 Research project objectives

1.2.1 Motivation

Being able to correctly predict the power production of a solar farm has thus become a topical issue in the past decade. The aim of this project is to develop the first physical PV model of Météo-France enabling photovoltaic production forecasting thanks to its NWP models.

The motivation behind the choice of a physical model is double. First, models developed thanks to machine learning or statistical approaches require historical data and the resulting optimized models are specific to the module considered, the origin of the inputs (whose bias is implicitly corrected during training or optimisation) and the localisation. A change in one of these elements thus requires a new model. On the contrary, a physical model does not have such inconveniences and can be universally applied.

Second, the fact that a physical photovoltaic model does not correct the inputs, information about the performance of the atmospheric model can be retrieved with an accurate physical PV model and PV power measurements, as most errors in the forecasts must originate from the atmospheric model. This means that better forecasts can overall be achieved by appropriately improving parametrisations in the atmospheric model (cloud optical properties, radiative transfer parameters, aerosols climatology, *etc*) and a better understanding of the atmospheric conditions is enabled. As such, PV forecasts assessment provides feedback on the performance of the atmospheric model used, which can in turn be refined to improve PV forecast.

Therefore, developing a physical photovoltaic model does not only lay the groundwork for site and module independent PV forecasting at Météo-France, it also opens up many new perspectives in terms of improving atmospheric models.

1.2.2 Challenges for physical PV models

1.2.2.1 Observed dependence of PV performance with atmospheric conditions

A physical approach presents its own inconveniences as it must accurately simulate the physical behaviour of a PV module. Yet, atmospheric characteristics can have intricate effects on PV performance. Studies have already clearly highlighted the effect of temperature and spectral irradiance on PV performance.

Almonacid et al. (2011) recalls that angular and spectral properties of radiation and temperature contribute to energy losses (respectively 4% and 15%). For instance, *Ghitas (2012)* observed for a same irradiance within a day a difference in PV production of up to 8.3% and highlights the effects of the solar spectrum on the performance of multicrystalline modules. Many other studies have pointed out the impact of spectral irradiance on photovoltaic performance and analysed this impact in terms of technology and location (*Jardine et al. 2001, Huld & Amillo 2015, Amillo et al. 2015*). Differences in performance have been explained by the seasonal variation of spectral irradiance (*Gottschalg et al. 2004*) and by the sensitivity of PV cells to different wavelengths (*Dirnberger et al. 2015*). This difference in sensitivity between technologies also implies that their increase in efficiency under cloudy skies can be more or less important (*Jardine et al. 2001, Nofuentes et al. 2014*) and has motivated studies on the impact of air mass, aerosol optical depth and precipitable water – which also affect the spectral properties of radiation – on the performance of different technologies (*e.g. Stark & Theristis (2015)*).

1.2.2.2 Limitations of current models

Though the spectral effect on PV performance is well known by the PV community, many models currently do not account for it (*e.g. Jerez et al. (2015)*) or at best apply a correcting factor (*e.g. King et al. (2004)*), but do not attempt to physically take it into account.

A major limitation to the application of physical models including spectral effects originates from the rare access to spectral irradiances as inputs: atmospheric models output by default broadband values and spectral irradiance measurements are rare. Photovoltaic models must therefore correct the production modelled with the broadband irradiance thanks to other indicators. For example, when considering open-source documentation for PV models including;

- the PlantPredict¹ - a PV modelling software based on meteorological inputs and a physical PV model;
- the PV_LIB Toolbox² which is in the idea similar to PlantPredict and is available thanks to the PV Performance Modeling Collaborative (PVPMC), a group of PV professionals who, with the Sandia National Laboratories, aim at improving current PV performance models;

the change in spectrum is accounted for thanks to a spectral mismatch factor which is computed with the modelled or provided precipitable water and air mass.

Besides, facilities are often only supplied with the global irradiance from the atmospheric models. In this case, the PV models mentioned above must estimate the direct and diffuse components from the global horizontal irradiance, following more or less elaborate methods (*Erbs et al. (1982)*, DIRINT (*Ineichen et al. 1992*), *Reindl et al. (1990b)*). Yet, direct and diffuse radiation differ in their angular properties, thus impacting the effective radiation impacting an inclined surface, but also in their spectral signature. *Kirn & Topic (2017)* aim at achieving higher power prediction accuracy by distinguishing the contribution of diffuse and direct solar irradiance: power gains of up to 10% for direct irradiance and losses of up to 24% for diffuse irradiance compared to the nominal power considering the global reference PV spectrum were experimentally observed.

Certain models are however starting to address some of these issues. WRF-SOLAR has recently been developed with the aim of providing the appropriate variables for solar forecasting, including the direct and diffuse components of radiation (*Jimenez et al. 2016*). However, these components are more sensitive to aerosol and cloud properties than the global horizontal irradiance (GHI) such that a more precise model including a better representation of aerosol–cloud–radiation has been developed for solar application purposes. The effect of aerosols on photovoltaic power generation has for example been proven by *Rieger et al. (2017)* where over-estimations of PV production during a Saharan dust outbreak were reduced by considering the forecast mineral dust rather than climatological maps of aerosols which are generally used in NWP models. Nevertheless, the extra variables provided by WRF-SOLAR do not include any information on the spectral distribution of radiation, which is an important property for photovoltaic modelling.

1.2.3 Strategy of the present work

The access to appropriate variables turns out to be a main issue for physically modelling PV performance. Besides, the spectral effect has proven to be an important topic for PV power forecasting.

¹<https://plantpredict.com/algorithm/introduction/>

²<https://pvpmc.sandia.gov/>

Hence, implementing a physical PV model in Meso-NH tackles many of these issues as internal variables which are not generally output by atmospheric models (including radiation per spectral band) can be accessed. This means that a physical PV model with limited assumptions and fully benefiting from the knowledge of direct and diffuse components as well as the irradiances for each spectral band of the radiative transfer model can be developed. Modelling the repartition of the radiation between the direct and diffuse components is no longer necessary, and spectral mismatch factors no longer need to be applied. Such a model is also independent of the location and can be applied for user-specified PV modules.

Although the physical PV model is initially intended to be coupled with Meso-NH, it should be self-standing and operational for any source of inputs (narrow or broadband irradiance, variable spectral bands, *etc.*), thus including the possibility to be integrated into other atmospheric models or applied to measurements.

1.3 Research methodology

This research project aims at implementing a PV power diagnostic tool in the Meso-NH atmospheric model. Three underlying challenges must therefore be tackled:

- Understanding the key input parameters for PV modelling;
- Developing a PV model which can be coupled to any atmospheric model;
- Assessing the performance of the coupled Meso-NH–PV model.

In order to meet these goals, this report will follow the structure presented here-below:

- The theory behind atmospheric radiation and PV which is required for understanding photovoltaic modelling is first presented in Part 2. Standalone radiative transfer simulations and observations have also been analysed and highlight important characteristics of solar radiation and photovoltaic power. Part 2 therefore offers a first insight into key parameters for PV modelling.
- Part 3 presents the tools and data used throughout this study.
- Given the key variables spotted in Part 2, the PV model has been developed accordingly and is briefly presented in Part 4. A scientific documentation of this PV model and the options it includes is herein enclosed (Appendix D). Readers are therefore invited to refer to Appendix D for a more in-depth explanation or description of any part of the photovoltaic model.
- The PV model is then thoroughly evaluated in Part 5 by decomposing it into many sub-components which are all individually tested against *in situ* observations at the SIRTAsite. This evaluation phase also enables the calibration of the model when different options are available. Then, the calibrated PV model is validated against an independent set of measurements.
- Part 6 proposes a more thorough investigation of the spectral and angular effects on photovoltaic performance thanks to the validated PV model. The impact of clouds on PV performance is first analysed, then a sensitivity analysis of PV power to the spectral and angular resolution of the irradiance provided to the PV model is carried out. Finally,

a comparison between the PV model and a more widely used simple model neglecting spectral effects is provided.

- Part 7 assesses the performance of the coupled Meso-NH–PV model. To do so, Meso-NH simulations are performed at the SIRTAs site. The errors in the coupled model are analysed and possible explanations are provided. Last, changes in parametrisation which may improve the performance of the atmospheric model are given.

PART 2

THEORETICAL BACKGROUND

This part provides the basics required in terms of atmospheric radiation and photovoltaics. *In situ* observations and radiative transfer simulations are also analysed in order to highlight the influence of angular and spectral properties of the incoming radiation on PV performance. This part therefore enables a better understanding of the key phenomena and variables for photovoltaic modelling.

2.1 Basics in atmospheric radiation

2.1.1 Solar spectrum

The Sun continuously emits electromagnetic radiation which partly reaches the surface of the Earth ([Liou 2002](#)). This electromagnetic radiation can be described thanks to the wave-particle duality concept: incident solar radiation can be viewed as consisting of “packets” or particles of energy, called photons ([Duffie & Beckman 2013](#)). The energy of a photon is a function of its frequency ν (or wavelength λ) and is related to Planck’s constant h :

$$E_\lambda = h\nu = \frac{hc}{\lambda}, \quad (2.1.1)$$

meaning that the energy of a photon increases with frequency (and decreases with wavelength). The spectral distribution of the electromagnetic radiation emitted by the sun is called the solar spectrum. This distribution over wavelengths introduces the important notion of spectral irradiance which consists in the energy of all photons for a given wavelength which fall on a square meter each second, and is expressed in $\text{W nm}^{-1} \text{m}^{-2}$. The spectral irradiance is negligible outside the short-wave (SW) domain (200-4000 nm), which is where the main solar radiation occurs. The broadband irradiance G is simply the integral of the spectral irradiance over wavelength.

The solar radiation reaching the top of the atmosphere, called extra-terrestrial or top-of-atmosphere (TOA) radiation, can be computed at all time thanks to the relative position of the Sun and the Earth. Its mean value – the solar constant – was established in the 1990s to be approximately 1366 W m^{-2} , though more recent measurements by the NASA’s Solar Radiation and Climate Experiment (SORCE) indicate that its current value (1361 W m^{-2}) is lower ([Kopp & Lean 2011](#)).

2.1.2 Mechanisms affecting the available solar radiation at the surface

Before reaching the ground, the solar radiation is attenuated by several processes.

2.1.2.1 Reflection

First, the radiation can be reflected, as shown in Figure 2.1.1 – in average, around 7% is reflected by the surface of the Earth and 23% by the clouds and atmosphere. Clouds are known to greatly contribute to the reflection of solar flux back to space, known as the “solar albedo effect” (Liou 2002). The ratio of flux reflected back to space to the incoming solar flux defines the planetary albedo, which varies between 0 and 1.

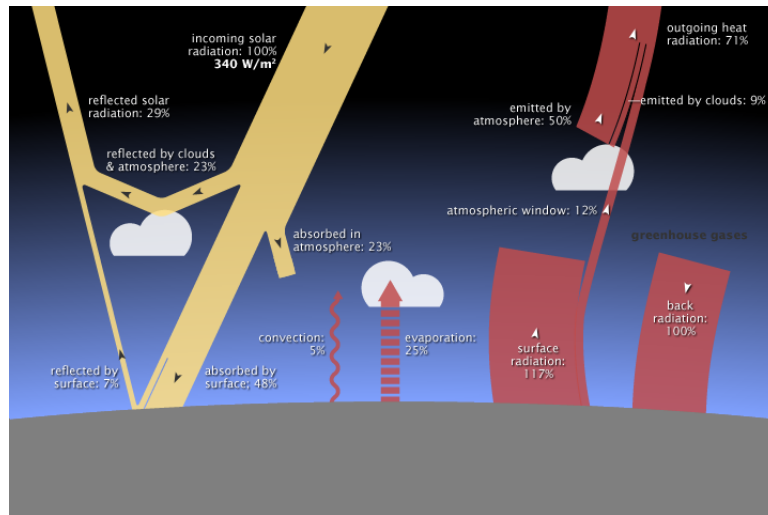


Figure 2.1.1: Global energy budget of the Earth¹. NASA illustration by Robert Simmon, adapted from Trenberth et al. (2009)

2.1.2.2 Absorption

The solar radiation can also be absorbed – around 23% by the atmosphere. Absorption in the atmosphere depends on the nature and concentration of gas which act as spectral filters thus distorting the shape of the solar spectrum as shown in Figure 2.1.2. Water vapour and ozone are the gas with the highest absorption rates along with molecular oxygen and carbon dioxide.

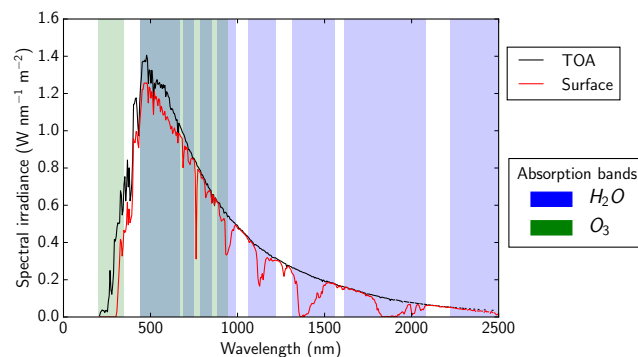


Figure 2.1.2: Top-of-atmosphere and ground-level solar spectra, simulated by MODTRAN for US Standard Atmosphere 1976, and absorption bands of water vapour and ozone following Liou (2002)

¹Given the incidence angle of the rays and the fact the only half the planet is illuminated at one moment, the spatial average of solar radiation is one-fourth the solar constant thus explaining the value of 340 W m^{-2} in Figure 2.1.1.

Clouds also alter the spectral distribution of the solar spectrum as different wavelengths are not evenly absorbed by liquid water and ice absorb as highlighted in Figure 2.1.3²: for instance, water is transparent for blue light for thicknesses up to several meters, whereas it becomes increasingly opaque in the near-infrared (NIR).

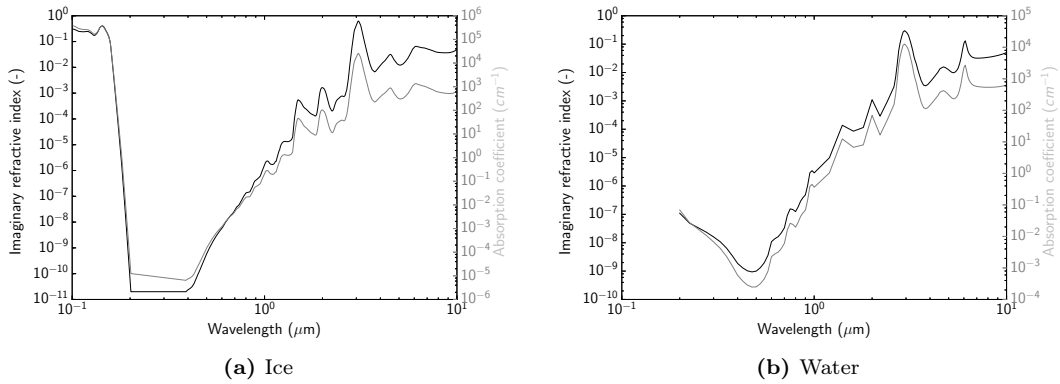


Figure 2.1.3: Imaginary part of the complex refractive index and corresponding absorption coefficient of ice and water. Data taken from [Warren & Brandt \(2008\)](#) for the ice and [Hale & Querry \(1973\)](#) for water.

2.1.2.3 Scattering

Solar radiation can also be scattered by the atmosphere, leading to diffuse radiation ([Liou 2002](#)), which is partly sent back to the outer space. Scattering occurs when the solar radiation encounters on its path a particle which changes the direction of light propagation. This particle could be for instance a gas molecule, an aerosol, a water droplet or an ice crystal.

Scattering efficiency depends on particle size. The size parameter x is defined in the case of a spherical particle (which is assumed for most particles) as the ratio between the particle circumference r and the incident wavelength λ ($x = \frac{2\pi r}{\lambda}$).

If $x \ll 1$, *i.e.* the particle size is small compared to the electromagnetic wavelength, so-called Rayleigh scattering occurs. Rayleigh theory indicates that the intensity scattered by a particle follows a λ^{-4} law. In other terms, the blue region of the visible spectrum is scattered $(\lambda_{red}/\lambda_{blue})^4 \approx 5.5$ times more than the red domain, thus explaining why the sky is blue.

When the size of the particle is comparable or larger to the electromagnetic wavelength ($x \gtrsim 1$), the scattering follows Lorenz-Mie theory. According to Lorenz-Mie theory, a small spherical particle globally scatters evenly between both forward and backward directions. As the size of the particle increases, the particle tends to increasingly scatter forwards.

Therefore, if clouds and aerosols result in Mie scattering, Rayleigh scattering also occurs in the atmosphere due to the presence of air molecules.

2.1.3 Direct and diffuse irradiance

The solar radiation that reaches the ground is therefore the sum of two contributions:

- the direct (or beam) radiation which comes directly from the sun, without being scattered or absorbed before reaching the ground;
- the diffuse (or sky-scattered) radiation incoming from all directions of the sky dome.

²The imaginary part of the complex refractive index n_i quantifies the absorption of the medium and is related to the absorption coefficient following $\alpha(\lambda) = \frac{4\pi n_i}{\lambda}$.

As illustrated in Figure 2.1.4, clear-sky diffuse radiation is heavily distributed in the blue domain but is close to zero in the NIR which is a direct consequence of Rayleigh scattering by the air molecules. On the contrary, direct radiation is more evenly distributed over the wavelengths.

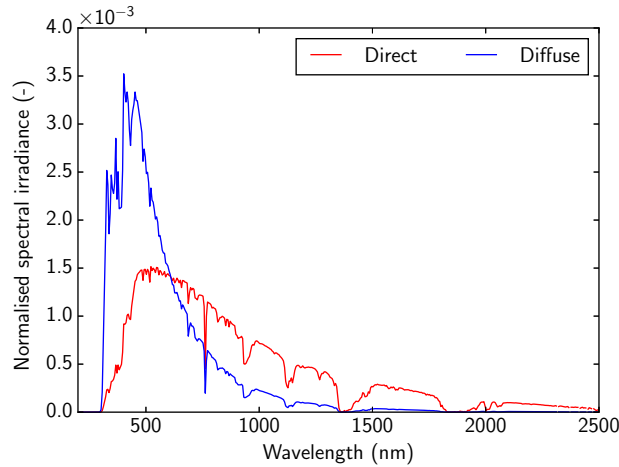


Figure 2.1.4: Direct and diffuse solar spectra normalised over the shortwave domain, simulated with MODTRAN considering US Standard Atmosphere 1976 and Solar Zenith Angle SZA = 48.2°

Therefore, direct and diffuse radiation differ by their effective angle and spectrum which both have a crucial impact on PV production. Furthermore, these angular and spectral properties of radiation are thus expected to be affected by the optical thickness of clouds.

2.2 Theory of photovoltaics

2.2.1 Photovoltaic devices

2.2.1.1 The photovoltaic effect

Photovoltaic technologies are based on a simple principle: when an incoming photon on a semiconductor has energy superior to the energy gap, electrons from the semiconductor can be excited from a ground to an excited state, creating a hole-electron pair, a hole being the lack of an electron in the structure (Figure 2.2.1a). This pair would normally disappear spontaneously as the electron and hole recombine. However, the recombination can be reduced by introducing a potential barrier (typically, a p-n junction) in the solar cell. The electrons can no longer move freely, which creates positive and negative layers. When these layers are connected thanks to an external circuit, the free electrons can flow through the system thus creating a current (2.2.1b).

2.2.1.2 Photovoltaic technologies

Various types of technologies, including different cell materials, designs, and manufacturing processes exist. The different PV technologies can be divided into three main groups, as illustrated in Figure 2.2.2 (Sampaio & González 2017) :

1. First generation technologies which are now fully commercialised and are based on silicon-crystalline technologies (Si);
2. Second generation technologies or thin film PV technologies, which are new on the market;
3. Third generation technologies, which are still being developed or in demonstration, such as organic PV technologies.

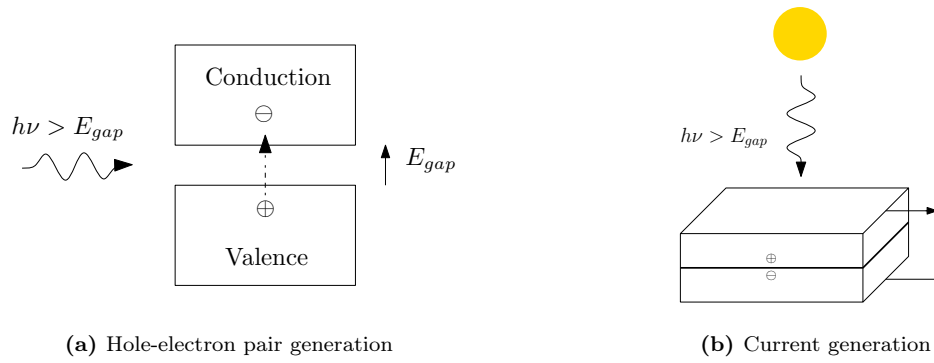


Figure 2.2.1: The photovoltaic effect

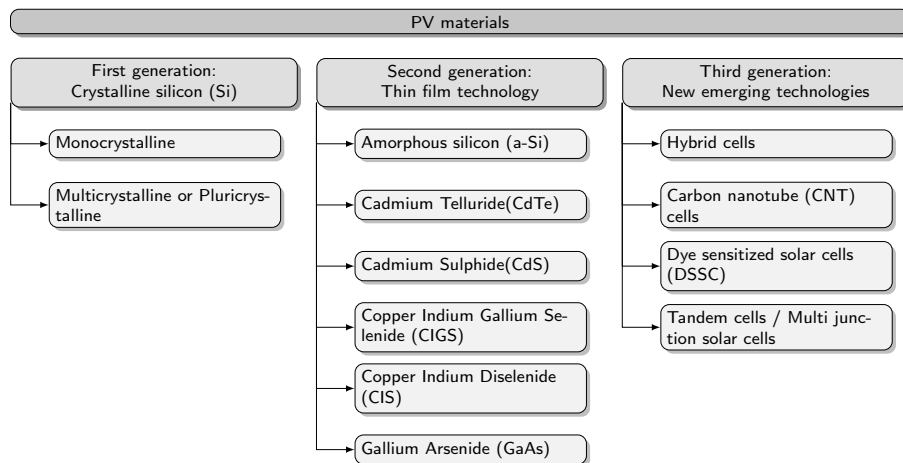


Figure 2.2.2: PV technologies

The different technologies rely on different semi-conductors able to exploit the photovoltaic effect. They differ by their efficiency, spectral response, their physical resistance (to heat, etc.) and their price. Appendix B provides an overview of the main technologies, a brief summary of their main advantages and disadvantages is provided in Table 2.2.1. Figure 2.2.3 provides the best cells and module efficiencies reached in laboratories for different PV technologies.

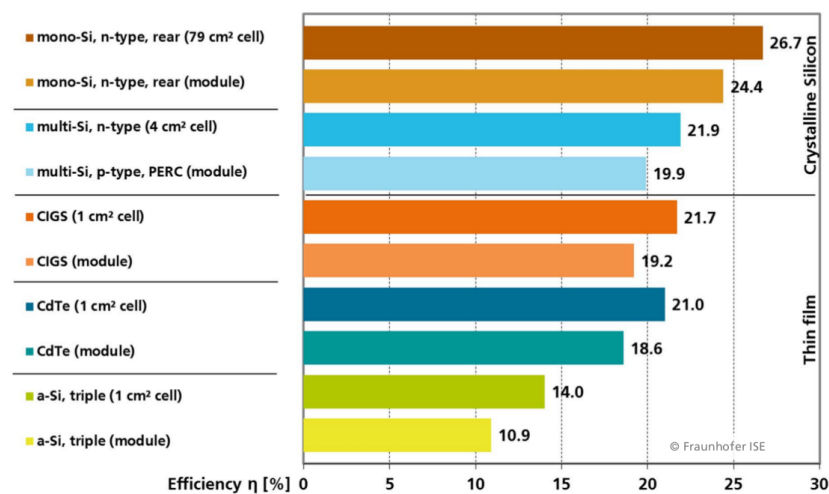


Figure 2.2.3: Best lab cells and modules efficiency depending on the technology. Graph taken from *Fraunhofer Institute for Solar Energy Systems* (2017) using data from *Green et al.* (2017)

Table 2.2.1: Main PV technologies : advantages and drawbacks

Technology	Advantages	Drawbacks
First generation		
Mono-crystalline silicon c-Si	high efficiency	expensive to manufacture, long energy return time
Polycrystalline p-Si, or mc-Si	easier to manufacture than c-Si	not as efficient as c-Si
Second generation		
thin film c-Si, pc-Si	reduced thickness, deposited on low-cost substrates	reduced efficiency
a-Si	easier to manufacture than c-Si	initial degradation induced by light, lower efficiency (lower cell quality)
CdTe	cost-effective production	toxicity of cadmium and environmental issues related to the use of Cd
CuInSe2 or CIS	high throughput processing, low cost of overall system, flexible and roll on – roll off substrate	issue for scaling up CIGS production (scarcity of In)
GaAs	high efficiency and lower-radiation induced degradation	toxic element As, expensive
Third generation		
organic PV cells	ease of processing, nontoxic, light, low cost, flexible modules of different shapes, colors, transparencies	limited durability, low efficiency
Dye-sensitized solar cells	simple assemble technology, potential low cost, choice of colors and opacities	limited large-scale applications as difficulty of synthesis

2.2.2 Ideal equivalent solar cell circuit

A PV module can be modelled as a “one diode model” as shown in Figure 2.2.4. This representation corresponds to the superposition of the diode-behaviour of a solar cell in the dark and the light-generated current (or photocurrent) I_L when exposed to solar radiation. The resulting load (or device) current is

$$I = I_L - I_D = R_L \times V. \tag{2.2.1}$$

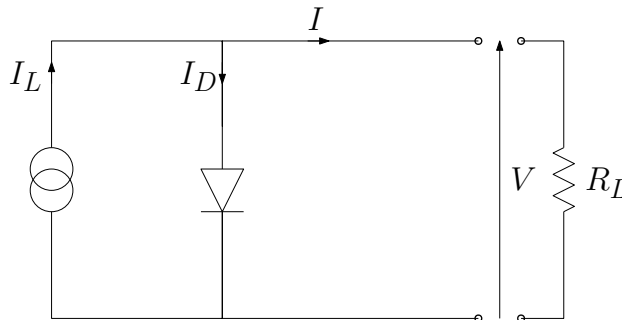


Figure 2.2.4: Equivalent ideal circuit of a solar cell

The photodiode current I_D is calculated following the Shockley diode equation (*Da Rosa*

2005, Duffie & Beckman 2013):

$$I_D = I_0 \left[\exp \left(\frac{qV}{nkT} \right) - 1 \right], \quad (2.2.2)$$

with I_0 the reverse saturation current, q the elemental charge, V the device voltage, n the ideality factor, k Boltzman constant and T the temperature. The ideality factor n of a diode indicates how close the diode follows the ideal diode equation ($n = 1$). Generally, $n = 1$ is assumed, corresponding to an ideal cell.

The device is therefore characterised by :

$$I = I_L - I_0 \left[\exp \left(\frac{qV}{nkT} \right) - 1 \right] \quad (2.2.3)$$

and the corresponding curve is known as the “I-V” curve (Figure 2.2.5a): there is an infinity of potential operational points (I, V).

The thermal voltage V_t defined by :

$$V_t \equiv \frac{nkT}{q} \quad (2.2.4)$$

allows to simplify (2.2.3) :

$$I = I_L - I_0 \left[\exp \left(\frac{V}{V_t} \right) - 1 \right] \quad (2.2.5)$$

2.2.3 Short circuit density and open circuit current

Two important parameters in PV modelling are the short-circuit current I_{SC} and the open-circuit voltage V_{OC} which are defined as the current (resp. voltage) at which the voltage (resp. current) are equal to zero, as illustrated in Figure 2.2.5a:

$$I_{SC} \equiv I(V = 0) = I_L \quad (2.2.6)$$

$$V_{OC} \equiv V(I = 0) \quad (2.2.7)$$

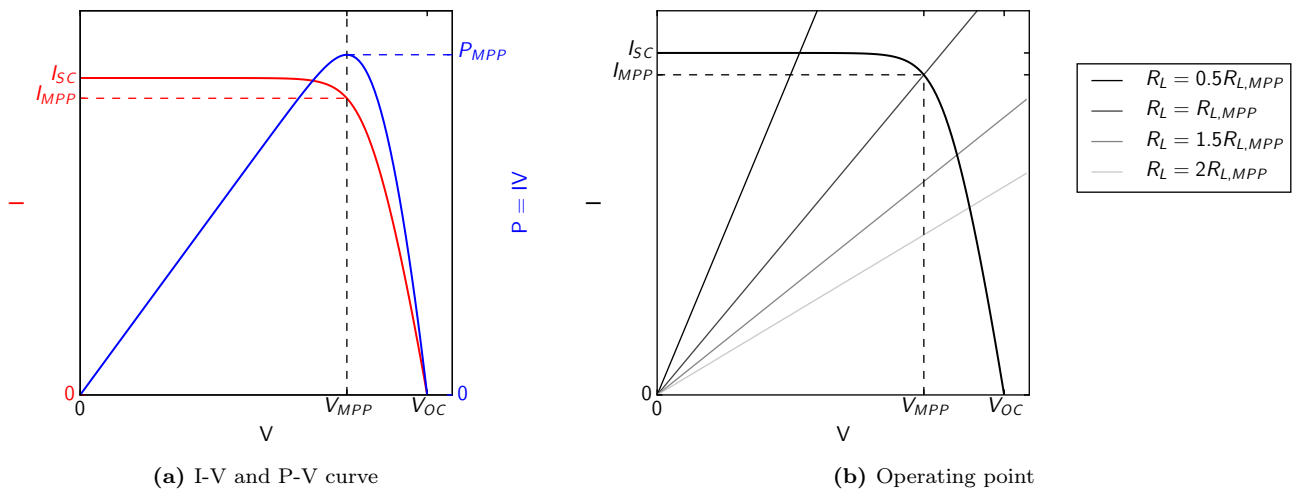


Figure 2.2.5: (a) I-V curve and (b) operating point defined by the resistive load and the I-V curve

2.2.4 Maximum power point and fill factor

The power supplied to the resistive load equals $P = I \times V$ knowing that the current and voltage are solved by the photodiode equation and by Ohm's law $V = R_L \times I$ as shown in Figure 2.2.5b. In practise, the operating configuration is set by choosing the load resistance R_L such that the operating point corresponds to the Maximum Power Point (MPP), which is the point where the power dissipated in the load is maximum, *i.e.* $R_{L,MPP} = \frac{V_{MPP}}{I_{MPP}}$. In the following and in the PV code, the PV module is assumed to be always operating in the optimal configuration. The product $I_{MPP} \times V_{MPP}$ corresponds to the maximum power that can be delivered to the load and is therefore always smaller than $I_{SC} \times V_{OC}$ which corresponds to the product of the greatest current and greatest voltage that can be extracted, but does not correspond to a possible operating point. The fill factor FF defined as :

$$FF \equiv \frac{I_{MPP} \times V_{MPP}}{V_{OC} \times I_{SC}} = \frac{P_{MPP}}{V_{OC} \times I_{SC}} \quad (2.2.8)$$

thus characterises the form of the I-V curve and is always smaller than 1.

2.2.5 Equivalent solar cell circuit with a series and shunt resistance

In a real solar cell, other effects must be taken into account which are generally modelled by a series and a parallel resistance :

- the parallel resistance (or shunt resistance) R_{sh} enables to simulate the leakages (edge of cell, diffusion paths, small metallic short circuits, etc). However, it has little importance under normal operating conditions and is therefore often assumed infinite;
- the series resistance R_s translates the resistance of metal contacts with the semiconductor, the resistance layers of the semiconductor itself or the resistance of metallic fingers which make up the front of the cell.

This leads to a more realistic equivalent circuit for a solar cell, given in Figure 2.2.6. The device is then characterised by :

$$I = I_L - I_0 \left[\exp \left(\frac{V + IR_s}{V_t} \right) - 1 \right] - \frac{V + IR_s}{R_{sh}}. \quad (2.2.9)$$

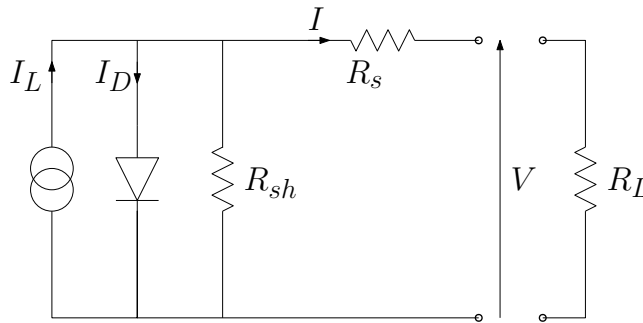


Figure 2.2.6: More realistic equivalent circuit of a solar cell.

Often, information such as the dark current I_0 are unknown meaning that this characterisation cannot be used. The following assumptions are therefore made: ([Lorenzo 2003](#)):

- the effect of parallel resistance can be neglected ($R_{sh} = \infty$);

- the photogenerated and short-circuit current are equal ($I_L = I_{SC}$);
- under all working conditions $\exp\left(\frac{(V+IR_s)}{V_t}\right) \gg 1$.

These assumptions simplify (2.2.9) into:

$$I = I_{SC} - I_0 \exp\left(\frac{V + IR_s}{V_t}\right). \quad (2.2.10)$$

Applying $I = 0$ in the expression above yields

$$V_{OC} = V_t \ln\left(\frac{I_{SC}}{I_0}\right), \quad (2.2.11)$$

whence

$$I_0 = I_{SC} \exp\left(-\frac{V_{OC}}{V_t}\right), \quad (2.2.12)$$

eventually leading to

$$I = I_{SC} \left[1 - \exp\left(\frac{V - V_{OC} + IR_s}{V_t}\right)\right]. \quad (2.2.13)$$

2.2.6 Current and density current

The density current is defined as the current per unit area. Therefore I (respectively I_{SC} , I_{MPP} , etc.) is related to J (respectively J_{SC} , J_{MPP} , etc.) by :

$$I_x = J_x \times A_c \quad (2.2.14)$$

with A_c the area of each cell.

2.2.7 Influence of the incoming radiation: photocurrent, spectral response and quantum efficiency

2.2.7.1 Photocurrent

The photocurrent I_L depends on the active surface (which can be assumed to be equal to the cell area A_c) and on the flux of photons $\Phi_{g,a}$ impacting the solar cell which are absorbed and whose energy is superior to the band (or energy) gap $E_{gap} = \frac{hc}{\lambda_g}$ of the semiconductor ([Da Rosa 2005](#)) :

$$I_L = q\Phi_{g,a}A_c, \quad (2.2.15)$$

or equivalently $J_L = q\Phi_g$ for the photocurrent density. Table 2.2.2 provides the energy band gap of the most common solar cells.

The absorbed photon flux $\Phi_{g,a}$ thus depends on three parameters :

1. the spectral irradiance, as the total incident photon flux Φ_g and irradiance at each wavelength are related by $G(\lambda) = \Phi_g(\lambda) \times \frac{hc}{\lambda}$;
2. the band gap and thus the nature of the semi-conductor;
3. the fraction of photons effectively absorbed by the solar cell.

Table 2.2.2: Energy band gap E_{gap} (Dupré et al. 2016) and λ_{gap} of different solar cells.

Cellule	E_{gap} eV	λ_{gap} μm
c-Si	1,125	1,10
Ge	0,661	1,88
GaAs	1,431	0,867
InP	1,351	0,918
CdTe	1,54	0,806
CdS	2,503	0,496
GaSb	0,727	1,71

2.2.7.2 Quantum efficiency

The quantum efficiency QE is defined as the ratio between the number of carriers collected by the solar cell and the number of photons incident for a given energy (or wavelength).

As a reminder, three cases are possible for an incoming photon:

1. $E_{\lambda} < E_{\text{gap}}$ or $\lambda > \lambda_{\text{gap}}$: the energy is insufficient to overcome the band gap and the photon is not absorbed ;
2. $E_{\lambda} = E_{\text{gap}}$ or $\lambda = \lambda_{\text{gap}}$: the energy is equal to the band gap and the photon has just enough energy to create a hole-electron pair and is absorbed ;
3. $E_{\lambda} > E_{\text{gap}}$ or $\lambda < \lambda_{\text{gap}}$: the photon energy is sufficient and the photon is absorbed.

In theory, the quantum efficiency can thus be computed following :

$$QE(\lambda) = \begin{cases} 1, & \text{if } \lambda < \lambda_{\text{gap}}. \\ 0, & \text{otherwise.} \end{cases} \tag{2.2.16}$$

However, in practise, not all photons with energy superior to the band gap are absorbed, as illustrated in the Figure 2.2.7.

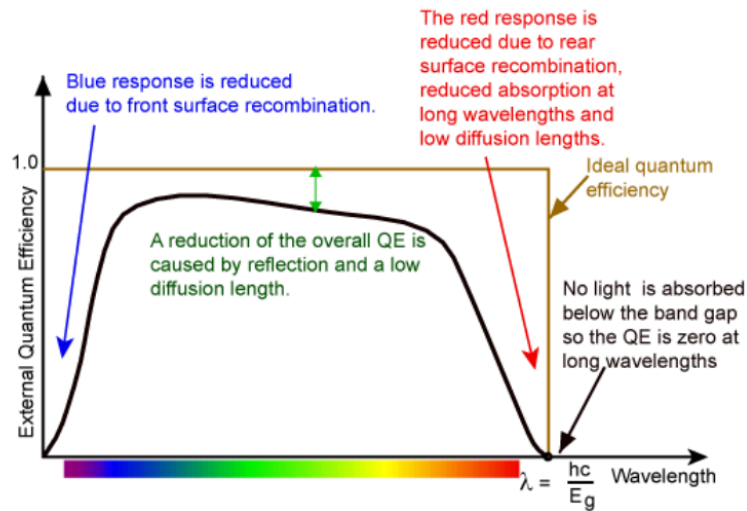


Figure 2.2.7: Typical and ideal external quantum efficiency, <http://www.pveducation.org/>

Figure 2.2.7 uses the term “external quantum efficiency” (EQE) which includes the optical losses at the cell level, whereas the “internal quantum efficiency” (IQE) only refers to the photons

which have not been reflected or transited outside the cell. In the following, the term “quantum efficiency” will be considered.

2.2.7.3 Spectral response

The spectral response is the ratio between the current generated by the cell and the incident power and is expressed in A W^{-1} . The flux of photons with a given energy E_λ is

$$\Phi_g(\lambda) = \frac{G(\lambda)}{E_\lambda} = \frac{1}{h\nu}G(\lambda) = \frac{\lambda}{hc}G(\lambda) \quad (2.2.17)$$

with G the spectral irradiance (given in $\text{W m}^{-2} \text{nm}^{-1}$).

The theoretical expression of the spectral response can then be deduced given the definition of the quantum efficiency following:

$$\text{SR}(\lambda) = \frac{q \cdot \Phi_g(\lambda) \cdot \text{QE}(\lambda)}{G(\lambda)} = q \cdot \frac{\lambda}{hc} \cdot \text{QE}(\lambda) \quad (2.2.18)$$

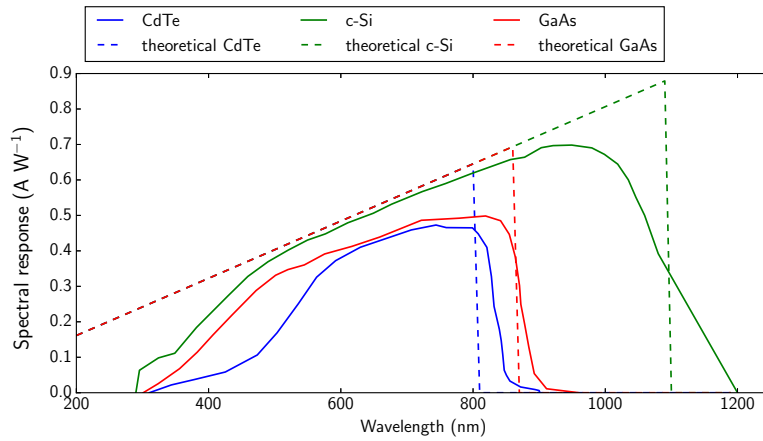


Figure 2.2.8: Real and ideal spectral response for different PV technologies. The real spectral responses are taken from <https://pvpmc.sandia.gov/modeling-steps/2-dc-module-iv/effective-irradiance/spectral-response/>.

Figure 2.2.8 compares examples of real and their equivalent ideal spectral response for different PV technologies.

2.2.8 Influence of the temperature

The energy band gap varies slightly with temperature: a higher temperature induces a smaller band-gap energy. Consequently, with increasing temperature, more of the solar spectrum has sufficient energy to excite electrons of the semiconductor and more current is generated (*Da Rosa 2005, Singh & Ravindra 2012*), implying a weak temperature dependence of I_{SC} . A temperature short-circuit current coefficient $C_{T,I_{\text{SC}}}$ is therefore introduced and is generally below $+0.05\% \text{ } ^\circ\text{C}^{-1}$.

Reverse saturation (or dark-light) current I_0 quantifies the leakage of minority carriers across the p–n junction in reverse bias. This leakage results in carrier recombination on either side of the junction. I_0 therefore directly affects V_{OC} (*Singh & Ravindra 2012*). However, minority carriers are thermally generated, such that I_0 increases exponentially with temperature and yields a negative open-circuit voltage temperature coefficient ($C_{T,V_{\text{OC}}} \approx -0.3\% \text{ } ^\circ\text{C}^{-1}$)

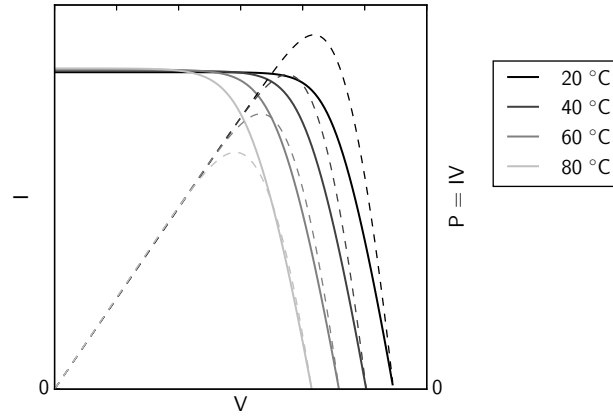


Figure 2.2.9: Influence of temperature on the I-V curve (solid) and P-V curve (dotted)

These temperature dependences mean that the I-V curve is directly influenced by the cell temperature (Figure 2.2.9) and others parameters such as the fill factor and the power are also affected. Manufacturer datasheets often indicate a power temperature coefficient of $C_{T,P_{MPP}} \approx -0.3\% \text{ } ^\circ\text{C}^{-1}$ and can sometimes reach $-0.5\% \text{ } ^\circ\text{C}^{-1}$. The negative influence of the temperature must therefore be taken into account when modelling PV production.

2.2.9 Reference conditions

Two reference conditions are commonly used to characterise PV modules.

Standard Test Conditions (STC) PV modules are generally rated under “Standard Test Conditions” (STC) which correspond to (Lorenzo 2003):

- Module inclination $\beta_{\text{STC}} = 37^\circ$;
- Module facing the sun, *i.e.* the solar and module azimuth angles are equal;
- Incident irradiance $G_{\text{POA,STC}} = 1000 \text{ W m}^{-2}$, incident solar spectrum for an air mass of 1.5 (AM 1.5);
- Cell temperature $T_{\text{c,STC}} = 25^\circ\text{C}$.

The most common reference spectrum used to represent STC is the American Society for Testing Materials 173-03 (ASTM 173-03) spectrum and notably relies on the United States Standard Atmosphere (USSA) 1976 (Myers *et al.* 2002, Myers & Gueymard 2004).

Normal Operating Cell Temperature A PV module is also characterised by measuring the Nominal Operating Cell Temperature (NOCT), defined as the cell temperature when the PV module is under nominal terrestrial environment (NTE) conditions (Lorenzo 2003):

- POA irradiance $G_{\text{NOCT}} = 800 \text{ W m}^{-2}$, incident solar spectrum for AM 1.5;
- Ambient temperature $T_{\text{a,NOCT}} = 20^\circ\text{C}$;
- Average wind speed 1 m s^{-1} ;
- Zero electrical load (*i.e.* open circuit, such that the cell efficiency equals $\eta_{\text{c,NOCT}} = 0$);
- The panel is normal to solar noon and mounted in a free-standing frame.

The NOCT is generally around 40°C .

These reference conditions are of utmost importance for PV modelling since most of the information given by the manufacturer on their datasheet correspond to these two operating conditions. Characteristics in the actual conditions thus have to be derived from these reference conditions.

2.2.10 From solar cells to modules and arrays

A module is made up of a set of solar cells. Usually, 36 (domestic use), 60 (typical residential grid connected system) or 72 (in the case of large commercial or utility scale solar systems) solar cells in series make up a module³. Modules wired in series are called a “string” and a set of strings wired in parallel are called an “array” as illustrated in Figure 2.2.10.

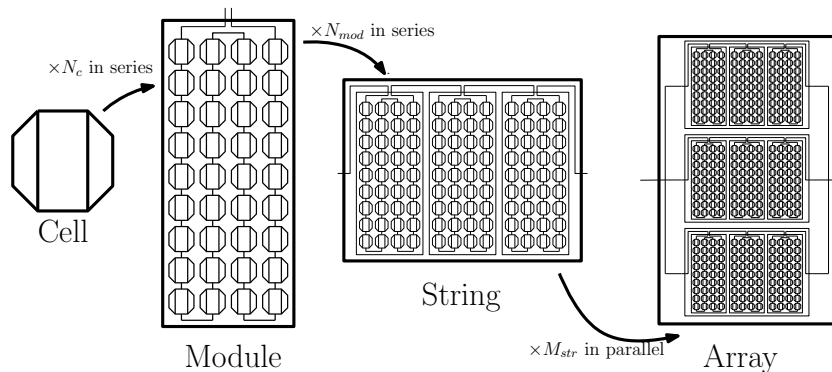


Figure 2.2.10: PV cell, module, string and array illustration

Series (resp. parallel) wiring allow to reach higher voltages (resp. currents) than those available from a single module (*Messenger & Ventre 2004*). For instance, from cell to module :

$$\begin{aligned} I_{\text{mod}} &= I_c \\ V_{\text{mod}} &= N_c \times V_c \end{aligned} \quad (2.2.19)$$

with the number of each subconstituent in series (resp. in parallel) denoted by N (resp. M), as shown in the Figure 2.2.10.

The Figure 2.2.11 provides an example on how the I-V curve varies depending on how the solar cells are connected.

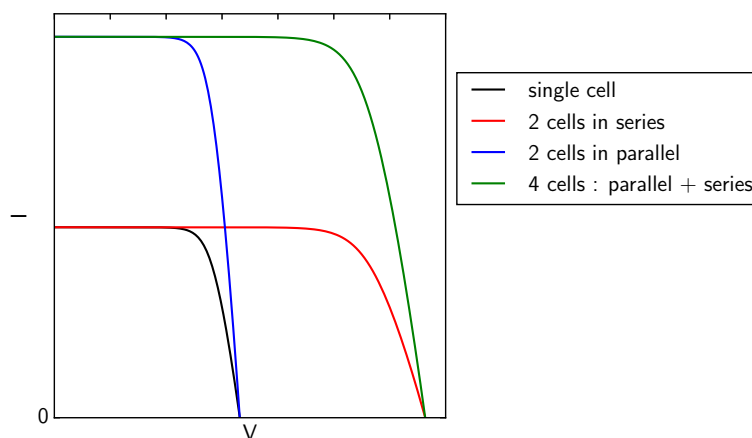


Figure 2.2.11: I-V curve for cells in series and in parallel

³<http://southerntiersolarworks.org/learn-more/solar101>

This means that the power of an array P_{arr} equals :

$$P_{\text{arr}} = M_{\text{str}} \times N_{\text{mod}} \times N_c \times P_{\text{cell}} \quad (2.2.20)$$

These differences must be accounted for when using information on the manufacturer's datasheet which are provided at the level of the module, or when wanting to compute the power of a photovoltaic farm, as the photovoltaics theory is based on the cell level.

2.3 Impact of the spectral and angular distributions of incident radiation on photovoltaic performance

The following highlights the impact of the characteristics of incident irradiance on the PV performance based on observations and numerical simulations. Note that the tools used in this part (the SIRTA observations, ecRad and MODTRAN radiative transfer models) are presented in Part 3.

2.3.1 With *in situ* observations

The measurements of module temperature, module power, Global Horizontal Irradiance (GHI) and Plane-Of-Array (POA) irradiance – the radiation normal to the surface of the PV module – on the SIRTA site are here analysed to emphasize on various parameters that must be taken into account in the PV model. The France Watts monocrystalline silicon module is taken as an example.

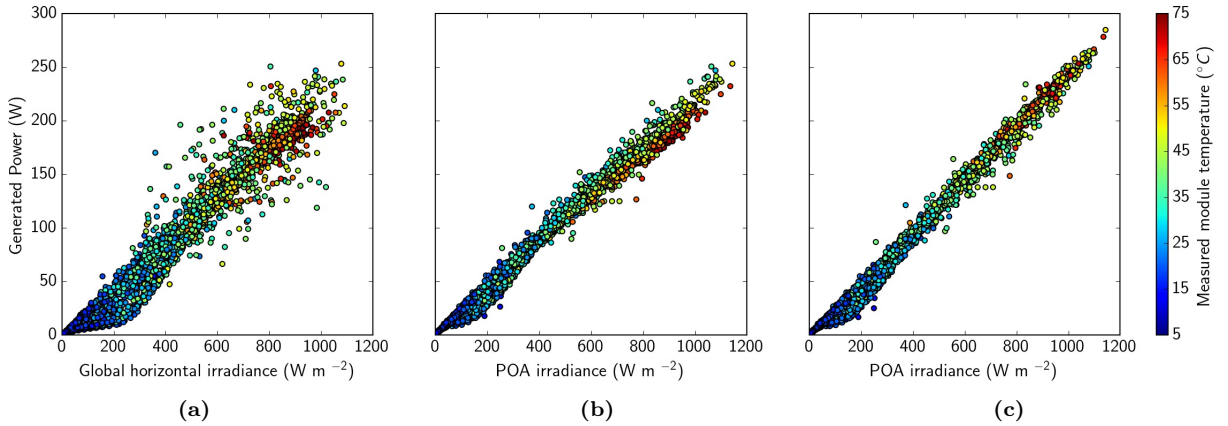


Figure 2.3.1: Observed module power as a function of (a) measured global horizontal or (b) POA irradiance. The power in (c) is corrected by $(1 - C_{T, P_{\text{MPP}}} \cdot (T_c - T_{c, \text{STC}}))$ to account for the expected influence of the temperature.

Figure 2.3.1a shows the power as a function of GHI and shows a wide dispersion of generated power for a given GHI. For instance, for $\text{GHI} \approx 800 \text{ W m}^{-2}$, the module power ranges from approximately 125 to 250 W and therefore presents a variation of 100%. This is not surprising because similar GHI does not imply similar POA irradiance due to the tilt of the module. Hence it is more relevant to plot the generated power as a function of the POA irradiance, as shown in Figure 2.3.1b. This emphasizes the importance of knowing the angular distribution of the incoming radiation in order to accurately compute the irradiance on a tilted surface, which constitutes a much more valuable information for PV modelling than the GHI. Practically, this means distinguishing the direct and diffuse contributions.

Yet, a dispersion of up to around 50 W is still noticeable for a given POA irradiance. Temperature can explain part of this scatter, because PV performance decreases with temperature (*Skoplaki et al. 2008*, *Almonacid et al. 2011*) However, the spread partly remains in Figure 2.3.1c once this temperature effect is corrected. This residual spread of approximately 30 W is attributed to optical losses but also various atmospheric conditions influencing the spectral distribution of the measured POA as shown in Part 2.3.2.

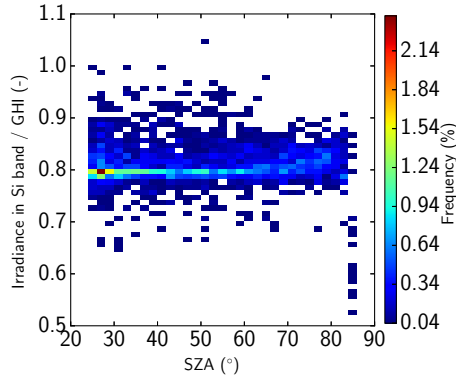


Figure 2.3.2: Ratio of the irradiance measured by the spectrometer (300–1050 nm) and the pyranometer (200 – 3600 nm) on the SIRTAsite over the month of June 2017.

Indeed, a change in spectral distribution can be noticed in Figure 2.3.2 comparing the measurements of the spectrometer (spectral range : 350–1050nm) – which in first approximation can be assimilated to the radiation which can be converted by a monocrystalline silicon cell as $\lambda_{\text{gap,c-Si}} = 1100 \text{ nm}$ – to the measurements of the pyranometer (spectral range: 200 – 3600nm) thus shedding light on the variation of radiation within the band that a solar cell is sensitive to. This observation also highlights the limits of methods considering the broadband irradiance (whether on a tilted or horizontal surface) without a correction factor accounting for atmospheric conditions as the useful fraction is not constant. Indeed, statistical or AI methods are generally based on forecasts of global radiation and temperature, as highlighted by the recent publications on solar power forecasting reviewed in *Antonanzas et al. (2016)*. Some physical models also compute the power by comparing the GHI to reference conditions and not accounting for the difference in portion of useful irradiance like *Jerez et al. (2015)*.

2.3.2 With radiative transfer simulations

Based on the above observations, the influence of atmospheric conditions on the irradiance is now further investigated thanks to ecRad simulations.

The atmosphere is set to US Standard Atmosphere 1976 (USSA 1976), and a cloud set between 546 and 1168m⁴. The cloud fraction is set to 1 and the cloud optical thickness is varied thanks to its water content. The position of the sun is constant (Solar Zenith Angle SZA = 48.2°).

Figure 2.3.3 shows the partition between direct and diffuse radiation with increasing optical thickness, thus showing how clouds filter radiation. Consequently, correctly computing direct and diffuse irradiance from the global irradiance is a non-injective function which requires having a good knowledge of the cloud properties, especially for an optical thickness below 20, where the proportion of diffuse irradiance increases sharply.

⁴Based on the 1D profile of the I3RC cumulus test case used by *Hogan et al. (2016)*

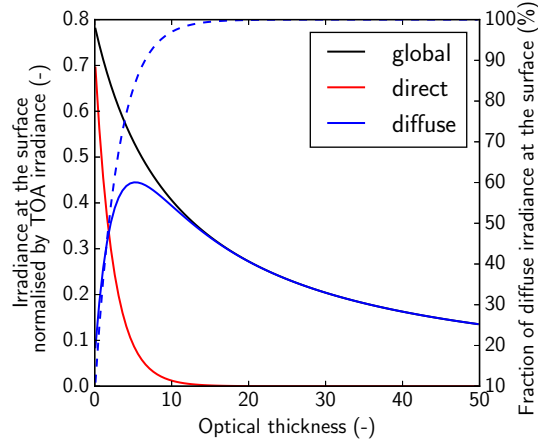


Figure 2.3.3: Atmospheric transmittance (global) and partition into direct and diffuse irradiance as a function of cloud optical thickness, simulated with ecRad.

Figure 2.3.4 shows that the fraction of shortwave GHI within the range absorbed by a silicon cell varies from 86% in clear-sky conditions to 97% for thick clouds. This fraction therefore depends on atmospheric conditions, which is in agreement with the observations in Figure 2.3.2.

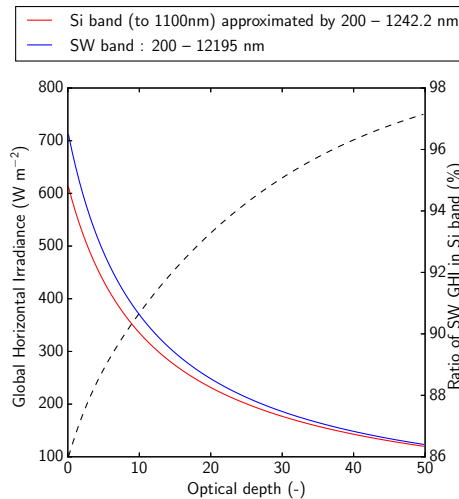


Figure 2.3.4: Global horizontal irradiance at the surface as a function of optical depth in the shortwave band and in the wavelength band absorbed by a silicon cell.

The influence of cloud optical thickness on spectral irradiance has been assessed thanks to two simulations for $\tau = 0$ (clear-sky) or 20 (cloudy) and for $\text{SZA} = 0^\circ$. The irradiance within each ecRad band normalised by the overall irradiance is given in Figure 2.3.5a and shows a difference in distribution over the bands: under cloudy skies, the irradiance is more heavily distributed in the shorter wavelengths. If the overall trend in both cases can be explained by Rayleigh scattering, which favours scattering in the blue domain, the difference in the normalised irradiance between clear and cloudy skies can be justified by the absorption of the water in the clouds: as reminded in Figure 2.1.3, water absorbs much more in the near-infrared (NIR) than in the visible domain.

The expected influence in terms of power production is illustrated in Figure 2.3.5b where the normalised irradiances have been further spectralised by using MODTRAN-simulated spectra (for the same SZA and under USSA) and compared to the ideal spectral response of a silicon

cell: clouds filter out photons which cannot generate current in a solar cell, which explains the global increase observed in the fraction of useful irradiance with optical depth (Figure 2.3.4). As the relative content in shorter wavelength is more important under cloudy sky, the efficiency of the solar cell – defined as the ratio between power and irradiance normal to the surface – in these conditions is expected to be higher, which is consistent with the observations of *Jardine et al.* (2001), *Nofuentes et al.* (2014) and *Kirn & Topic* (2017).

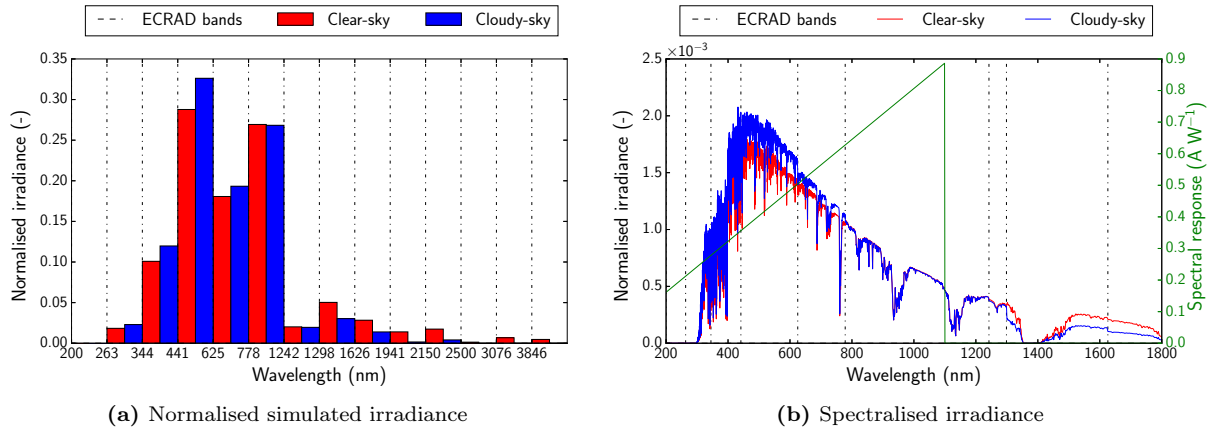


Figure 2.3.5: Normalised spectral irradiance for a clear and cloudy-sky

To conclude, this brief analysis of observations and ecRad simulations shed light on the importance of the angular and spectral properties of radiation.

PART 3

TOOLS AND DATA

Radiative transfer and atmospheric models handled in this project are first introduced. In a second phase, the measurements from the SIRTAs which are used throughout this project and notably for the model evaluation are presented. Last, in order to identify the possible inputs for the PV model, it is essential to be aware of what information is available. Therefore, the data commonly provided on PV modules is described.

3.1 Radiative transfer models

Radiative transfer models are numerical methods allowing to resolve the radiative transfer equation and provide the direct and diffuse radiative fluxes at the surface for given atmospheric conditions.

Common approximations include the “two-stream” approach where the radiation propagates in only two discrete directions (up and down), or the “plane-parallel” medium where the medium is assumed to be stratified in homogeneous horizontally infinite plane and parallel layers.

Ideally the radiative transfer equation should be solved at each wavelength as atmospheric properties – such as gas absorption – are wavelength dependent. However, this thorough approach is often too computationally expensive, especially for operational applications. Different methods have thus been developed in the aim of reducing the computation cost.

3.1.1 The MODerate resolution atmospheric TRANsmission (MODTRAN)

The MODerate resolution atmospheric TRANsmission (MODTRAN) is a radiative transfer scheme originally developed in the 1980s (*Berk et al. 1987*). MODTRAN is used in this project to provide high resolution spectra thanks to its 4800 bands in the 200 – 5000 nm spectral range. Also, the USSA 1976 is a standard atmosphere available in MODTRAN meaning that spectral irradiances with USSA 1976 can easily be computed.

3.1.2 ecRad

A new radiation scheme for the IFS, called ecRad, has recently been developed by the European Centre for Medium-range Weather Forecasts (ECMWF) and constitutes its operational code since cycle 43R3 (summer 2017)¹. This radiative model is based on the two-stream approximation and assumes a plane-parallel medium. Compared to their previous code, this new code includes a more efficient radiation scheme, refined climatologies, more cloud overlap assumptions and the possibility to represent 3D radiative effects or cloud horizontal heterogeneities

¹<https://software.ecmwf.int/wiki/display/FCST/Implementation+of+IFS+cycle+43r3>

([Hogan & Bozzo 2016](#)). Furthermore, ecRad uses fourteen spectral bands in the shortwave domain which are provided Table 3.1.1 and that correspond to RRTM ([Mlawer et al. 1997](#)).

Table 3.1.1: Wavelength and wavenumber of the 14 SW bands in ecRad

Wavenumber min cm^{-1}	Wavenumber max cm^{-1}	Wavelength min μm	Wavelength max μm
820	2600	3,84	12,2
2600	3250	3,07	3,84
3250	4000	2,50	3,07
4000	4650	2,15	2,50
4650	5150	1,94	2,15
5150	6450	1,55	1,94
6450	7700	1,29	1,55
7700	8050	1,24	1,29
8050	12850	0,778	1,24
12850	16000	0,625	0,778
16000	22650	0,442	0,625
22650	29000	0,345	0,442
29000	38000	0,263	0,345
38000	50000	0,200	0,263

In this project, ecRad radiation scheme will be run in standalone mode. The USSA 1976 is not predefined, such that its atmospheric profile has been recreated in ecRad as finely as possible from the characteristics used in MODTRAN. However, unless mentioned otherwise, the ecRad-modelled USSA 1976 does not contain aerosols as the means of specification are not comparable between both models.

3.2 Assessing the optical thickness of clouds

Cloud optical thickness is one of the main properties quantifying the influence of clouds on radiation. The optical thickness (or optical depth) expresses the attenuation of a beam by absorption or scattering during its path through a given medium (atmosphere, cloud, *etc.*) and is therefore directly related to the sum of the absorption and scattering coefficient, called extinction coefficient σ_e , by:

$$\tau = \int \sigma_e(z) dz. \quad (3.2.1)$$

When the physical properties of the cloud are known, its optical thickness can be deduced from the Liquid Water Content LWC, the effective droplet radius r_{eff} and water density ρ_w following

$$\tau = \int \frac{3 \text{LWC}(z)}{2 \rho_w r_{\text{eff}}(z)} dz, \quad (3.2.2)$$

where a monodisperse distribution of drop size is assumed. Equation (3.2.2) thus provides an estimation of the physical optical thickness². Appendix A provides further information on the derivation of (3.2.2) and details how the LWC is computed from the liquid water mixing ratio which is more frequently used in models than the LWC.

However, physical properties are not always known and another way to estimate the optical thickness is therefore required. A solution consists in considering the transmittance which is

²In ecRad, non-monodisperse distributions of drop size is considered (*e.g.* [Slingo \(1989\)](#))

directly related to the optical depth following

$$T_b = \exp(-\tau) \quad (3.2.3)$$

in the case of the beam irradiance and for the global irradiance (*Kokhanovsky & Rozanov 2003*)

$$T_g = \frac{1}{1 + \frac{3}{4}(1-g)\tau}, \quad (3.2.4)$$

with g the asymmetry parameter which is equal to 1 in a fully forward scattering medium and -1 in a fully backward scattering medium. For clouds, the value of $g = 0.86$ is commonly used (*e.g. Petty (2002), Kokhanovsky (2004)*), whereas 0.85 is used for instance by *Bohren (1987)*). The equation (3.2.4) is however valid for weakly absorbing homogeneous plane-parallel light scattering layers with no underlying surface (or a non-reflective surface) (*Kokhanovsky & Rozanov 2003*), which is never the case in reality but is assumed in this project as being met.

The inversion of (3.2.3) or (3.2.4) enables to retrieve the optical thickness from simulated or measured transmittances. Yet, these transmittances should ideally be applied at the top and bottom of the medium (for instance here clouds) but measurements are generally provided at ground level whereas top-of-atmosphere irradiance can be theoretically computed from the position of the Sun. Consequently, deriving the clouds optical thickness from measurements is not straightforward and a method is developed here below.

First, both the global and direct approaches are tested thanks to ecRad simulations. The atmosphere is set to US Standard Atmosphere 1976 (USSA 1976), and a cloud set between 546 and 1168m³ with a cloud fraction of 1. The liquid water content of the cloud (and thus τ) and SZA are varied to simulate various atmospheric conditions.

The relationships (3.2.3) and (3.2.4) are assessed by considering the transmittance modelled by the ground-level and TOA irradiances and the optical depth derived from the physical properties of the cloud with (3.2.2) which is considered here as the reference optical thickness. The results show that the fit of the global transmittance is more satisfying such that this approach is chosen in the following.

The results with the global approach are nevertheless unsatisfactory for several reasons. First, a dependance in SZA of the error is noticeable, with an increase in dispersion between different values of SZA with τ . For instance, the retrieved optical thickness nearly doubles in value between SZA = 0° and 60° for $\tau_{\text{phys}} = 20$.

Second, the retrieved optical thickness does not tend towards 0 as the physical optical thickness decreases, meaning that this approach always computes an optically thick cloud, even in the absence of clouds. This can be explained by the fact that the transmittance of the whole atmosphere is considered with the TOA and surface irradiances, including the contribution of aerosols and gas. An improved method therefore consists in assuming the overall transmittance as being the product between the transmittance of clouds T_{cloud} and that in the same atmospheric conditions but without the clouds T_{atm} :

$$T = T_{\text{cloud}} \times T_{\text{atm}} \quad (3.2.5)$$

³Based on the 1D profile of the I3RC cumulus test case used by *Hogan et al. (2016)*

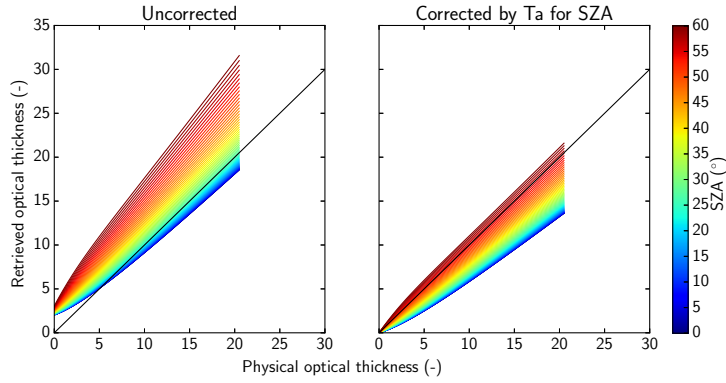


Figure 3.2.1: Retrieved optical thickness as a function of the optical thickness computed from the physical properties of the cloud for various SZA with ecRad simulations

This correction of T_{cloud} is expected to improve the optical thickness given the previous unsatisfying observations: T_{atm} for a given atmosphere varies with the length of the path, hence it is highly dependent on SZA thus decreasing the dependence in SZA of T_{cloud} , but can also contribute to a more precise evaluation of low cloud optical depths by increasing the transmittance of clouds compared to the previous approach.

The newly computed T_{cloud} can then be used to retrieve the cloud optical thickness thanks to (3.2.4) for the various atmospheric conditions already simulated in ecRad and are compared to the estimated physical optical depth. Figure 3.2.1 indicates that this method is more satisfying as the behaviour close to 0 is corrected and the dispersion is decreased. Nevertheless, the computed optical thickness is still dependent of the SZA, with an increasing underestimation as SZA decreases.

Besides, spectral filtering implies that the clouds do not have the same optical thickness for all wavelengths. One can therefore hope to improve the method by considering the transmittance over a specific domain in the SW. The same analysis as above is therefore conducted but by considering the transmittance individually over all fourteen ecRad bands. However, this method did not seem to improve drastically the results (Figure 3.2.2) and introduces a dependence of τ on the choice of wavelength range. This dependence can turn out to be problematic, for instance when comparing τ between different sources as spectral bands change between atmospheric models and in case of observations it relies on the measurements spectral irradiance which is not common.

To conclude, in the following, the optical thickness with ecRad simulations is computed thanks to the physical properties of the simulated clouds whereas in the absence of knowledge on the physical properties of clouds (measurements, atmospheric models), the optical thickness is retrieved from the global transmittance in the whole SW once corrected by the clear-sky atmospheric transmittance for the same SZA. It is nevertheless to be noted that if in the case of ecRad this atmospheric transmittance is easy to compute for the same atmosphere, in the case of observations, T_{atm} is simulated in ecRad under the assumption of a US standard atmosphere 1976. Finally, the dependence of the retrieved τ on SZA implies that it is more a helpful proxy to the optical thickness than an accurate estimation of this quantity.

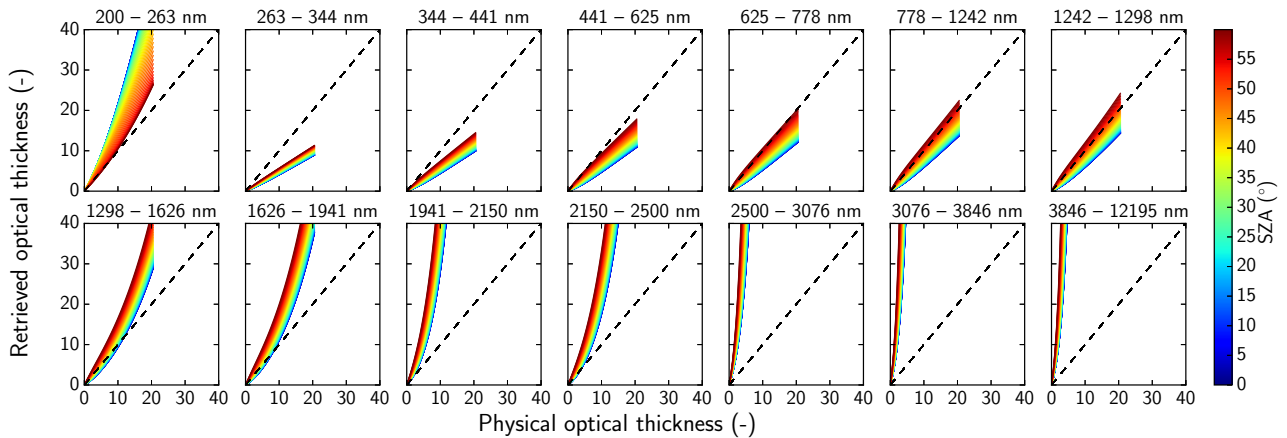


Figure 3.2.2: Retrieved optical thickness from the transmittance per ecRad band as a function of the optical thickness computed from the physical properties of the cloud for various SZA.

3.3 The Meso-NH atmospheric model

Meso-NH is a Mesoscale Non-Hydrostatic atmospheric model developed as a joint effort by the Centre National de Recherches Météorologiques (CNRM) and Laboratoire d’Aérodynamique (LA) (*Lafore et al. 1998*) and is freely accessible since April 2014. It has been designed to be a research tool for numerical models ranging from large scale (synoptic) to small scale (large-eddy) and thus aimed to be as flexible as possible.

Meso-NH model is coupled to the SURFEX surface model for the representation of surface-atmosphere interactions (*Bougeault et al. 2017*). A set of physical parametrizations as well as different modules enable flexible modelisation. Moreover, it enables easy grid-nesting as well as initialisation and forcing with observations (*e.g.* from other atmospheric models at Météo-France or ECMWF).

The longwave radiation scheme used by MesoNH is the Rapid Radiation Transfer Model (RRTM) developed by the ECMWF (*Mlawer et al. 1997*). Shortwave radiation is computed following *Fouquart & Bonnel (1980)* over the six bands given in Table 3.3.1.

Table 3.3.1: The six SW bands of the radiative transfer model currently used in Meso-NH

Band	Wavelength min μm	Wavelength max μm
1	0,185	0,25
2	0,25	0,44
3	0,44	0,69
4	0,69	1,19
5	1,19	2,38
6	2,38	4,00

ecRad has recently been implemented into Meso-NH, thus increasing the number of SW bands to 14, though this new development is still being tested.

The French operational atmospheric model AROME has widely inherited from the physical packages of Meso-NH (*Ducrocq et al. 2005*) and all developments on this research model can be plugged into AROME. Hence, this current project partly based on Meso-NH could be in the future used for prevision once added to the operational AROME model used for weather forecasting at Météo-France.

3.4 Available data

3.4.1 Measurements on the SIRTA site

The SIRTA (Site Instrumental de Recherche par Télédétection Atmosphérique) is an atmospheric observatory 20 km South of Paris. A PV platform has been installed on site, allowing to have a rich dataset including both atmospheric and PV modules measurements, *Yi et al.* (2015). In this study, SIRTA measurements for the whole months of June and December 2017 are available and contain most importantly the following variables:

- PV maximum power point (P_{MPP}), fill factor, open-circuit voltage and module temperature for five different panels (each corresponding to a different technology : m-Si, a-Si/ μ c-Si, HIT, CdTe, CIS) at 10-minute resolution;
- Wind speed, air temperature and relative humidity in the PV modules’neighbourhood;
- Global horizontal irradiance (GHI), direct normal irradiance (DNI), diffuse horizontal irradiance (DHI), plane-of-array (POA) irradiance averaged over 10 minutes;
- Spectral global horizontal irradiances with one-minute resolution, given in $W m^{-2} \mu m^{-1}$;
- Information on the atmospheric conditions, namely aerosol optical depths, precipitable water content, Angstrom coefficients and the Total Column Ozone.

All data except spectral irradiances are 10-minute averaged variables since sampling frequencies differ between instruments but also to account for the 700 m distance between some of the instruments which could induce noticeable differences at a smaller time resolution. Figure 3.4.1 summarizes the different instruments on site whereas further information is provided in Appendix C (*e.g.* spectral range, accuracy, location). It is to be noted that:

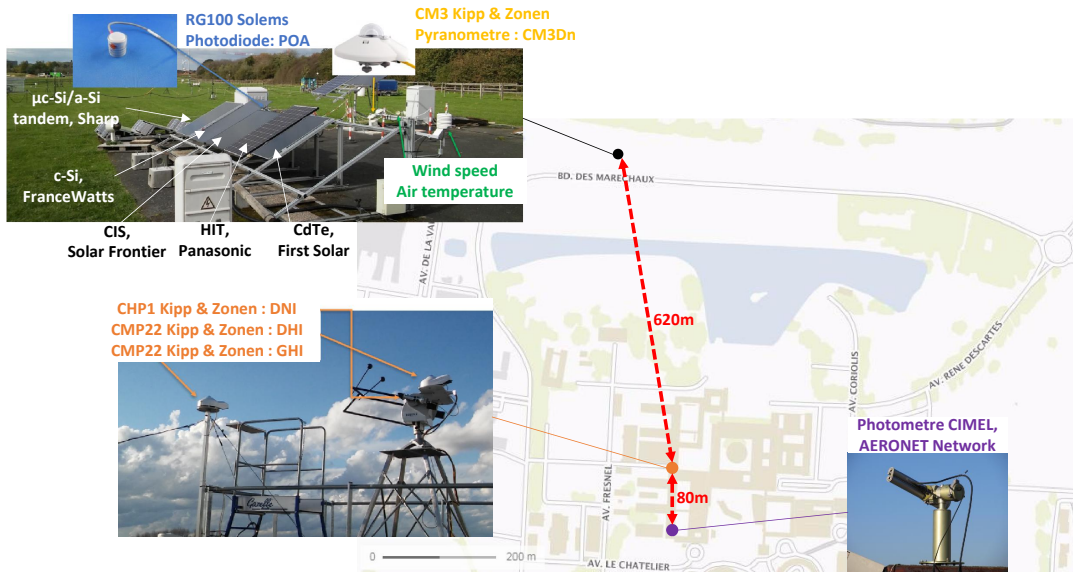


Figure 3.4.1: Instruments localisation, adapted from SIRTA.

- The “measured I_{SC} ” referred to in the following is deduced from the measurements of V_{OC} , FF and P as the measured I_{SC} in the dataset was empty;

- The pyranometer is chosen as reference for the POA irradiance rather than photodiode, as the photodiode is calibrated against a given global radiation spectrum and is not sensitive to wavelengths above 1100 nm: any change in the spectral distribution above 1100 nm compared to the calibration spectrum will not be accounted for;
- The GHI and DHI are measured over 200-3600 nm whereas the DNI instrument is sensitive over 200-4000 nm. Therefore, $G_b = \text{GHI} - \text{DHI}$ is used in the following rather than $G_b = \text{DNI} \cdot \cos(\text{SZA})$ in order to have consistent horizontal irradiance measurements. The difference between both approaches is generally of less than 15 W m^{-2} and presents a daily trend;
- The POA irradiance is measured over 300-3000 nm meaning that it cannot be directly compared to conversion of DHI, GHI or DNI due to mismatching wavelength domains.
- The spectral irradiance is provided only over 350-1050 nm

3.4.2 PV module manufacturer's datasheet

Manufacturer's datasheets are the only details that are assumed to be provided on the PV modules. Table 3.4.1 summarizes the most commonly parameters given by the manufacturers.

Table 3.4.1: Variables commonly provided by the manufacturer's datasheet

Variable	Notation	units
STC conditions		
Maximum (nominal) power	$P_{\text{MPP,mod,STC}}$	Wp
MPP current	$I_{\text{MPP,mod,STC}}$	A
MPP voltage	$V_{\text{MPP,mod,STC}}$	V
Short-circuit current	$I_{\text{SC,mod,STC}}$	A
Open-circuit voltage	$V_{\text{OC,mod,STC}}$	V
NOCT		
Temperature	NOCT	°C
Temperature dependance		
Temperature power coefficient	$C_{T,P_{\text{MPP}}}$	% °C ⁻¹
Temperature coefficient of I_{SC}	$C_{T,I_{\text{SC}}}$	% °C ⁻¹
Temperature coefficient of V_{OC}	$C_{T,V_{\text{OC}}}$	% °C ⁻¹
Other		
Module area	A	m ²
Number of cells	N_c	-
Cell type		
Power tolerance	$\epsilon_{P_{\text{MPP}}}$	%

However PV theory used in the PV code is based on solar cells. This means that the information provided must be converted to the equivalent cell values, according to the explanations provided in Part 2.2.10. This is done following (2.2.19) :

$$\begin{aligned}
 P_{\text{MPP},c} &= \frac{P_{\text{MPP,mod}}}{N_c} \\
 I_{x,c} &= I_{x,\text{mod}} \\
 V_{c,c} &= \frac{V_{x,\text{mod}}}{N_c}
 \end{aligned} \tag{3.4.1}$$

with x representing the maximum power point, the short-circuit current or the open-circuit voltage. The PV code also manipulates variables normalised per unit area to be in coherence

with radiation inputs. One therefore has, with $A_c \approx \frac{A}{N_c}$ (*i.e.* neglecting the cell interspacing):

$$\begin{aligned} P_{\text{MPP},c} &= \frac{P_{\text{MPP},\text{mod}}}{A_c} \\ I_{x,c} &= \frac{I_{x,\text{mod}}}{A_c} \\ V_{x,c} &= \frac{V_{x,\text{mod}}}{N_c} \end{aligned} \tag{3.4.2}$$

The voltage and intensity cannot be both per unit area for homogeneity reasons as $P = V \times I$, and given that the short-circuit current is directly linked to irradiance, the voltage is not normalised.

PHOTOVOLTAIC PRODUCTION MODELLING

In this chapter, the overall structure of the developed PV model is introduced and the motivations exposed. Then each subcomponent is explained and the different options available mentioned. The reader is referred to the scientific documentation in Appendix D for further details. Eventually, the PV model has been structured into a user-friendly way, and the format of the final tool is presented.

4.1 Main components of PV modeling

The operating power of a PV cell can be computed from the fill factor, the short-circuit current and the open-circuit voltage following

$$P = FF \times I_{SC} \times V_{OC} \quad (4.1.1)$$

The PV model is based on (4.1.1) meaning that computing the power is equivalent to computing FF, I_{SC} and V_{OC} .

The short-circuit current I_{SC} is assumed equal to the photogenerated current (see Part 2.2.5). Given the definition of the spectral response as well as the the short-circuit current temperature coefficient, I_{SC} is computed for various irradiances and cell temperatures thanks to:

$$I_{SC} = \left[\int SR_{modeled}(\lambda)G(\lambda)d\lambda \right] \cdot (1 + C_{T,I_{SC}} \cdot (T_c - T_{c,STC})) \quad (4.1.2)$$

A spectralised irradiance at the cell-level is therefore required, as well as an accurate estimation of the spectral response and the cell temperature. The other parameters are provided by the manufacturer. This I_{SC} model thus enables to account for the spectral and the temperature effects mentioned in Part 2.3.

The open-circuit V_{OC} is modelled based on

$$V_{OC} = V_t \ln \left(\frac{I_{SC}}{I_0} \right) \quad (4.1.3)$$

which is deduced by applying (2.2.5) for V_{OC} (2.2.7). The logarithmic relationship between V_{OC} and the short-circuit irradiance thus links V_{OC} to the irradiance. Yet, the open-circuit

voltage is mainly dependent on the cell temperature due to the thermal voltage V_t term. Two approaches are proposed to compute V_{OC} for any given conditions:

- A first simple approach consists in translating the value of V_{OC} from STC to the operating conditions by varying the incoming irradiance then the temperature thanks to $C_{T,V_{OC}}$ (hereafter the “simple” V_{OC} option)
- A second approach consists in physically modelling the temperature dependence thanks to the precise formulation of I_0 which is highly sensitive to temperature (*Singh & Ravindra 2012*) (hereafter the “ I_0 ” V_{OC} option).

The fill factor FF is computed following *Green (1982)* and depends on I_{SC} , V_{OC} , V_t (directly linked to T_c) and R_s . The fill factor thus requires another subcomponent to correctly compute the series resistance. *Green (1982)* provides two different options referred to in the following as the “simple” and “complex” FF options.

Additional variables have therefore been identified (cell temperature, spectral response, cell impacting spectral irradiance, series resistance) and must be also modelled. The PV model can therefore be simply represented by the interaction between different subcomponents as shown in Figure 4.1.1.

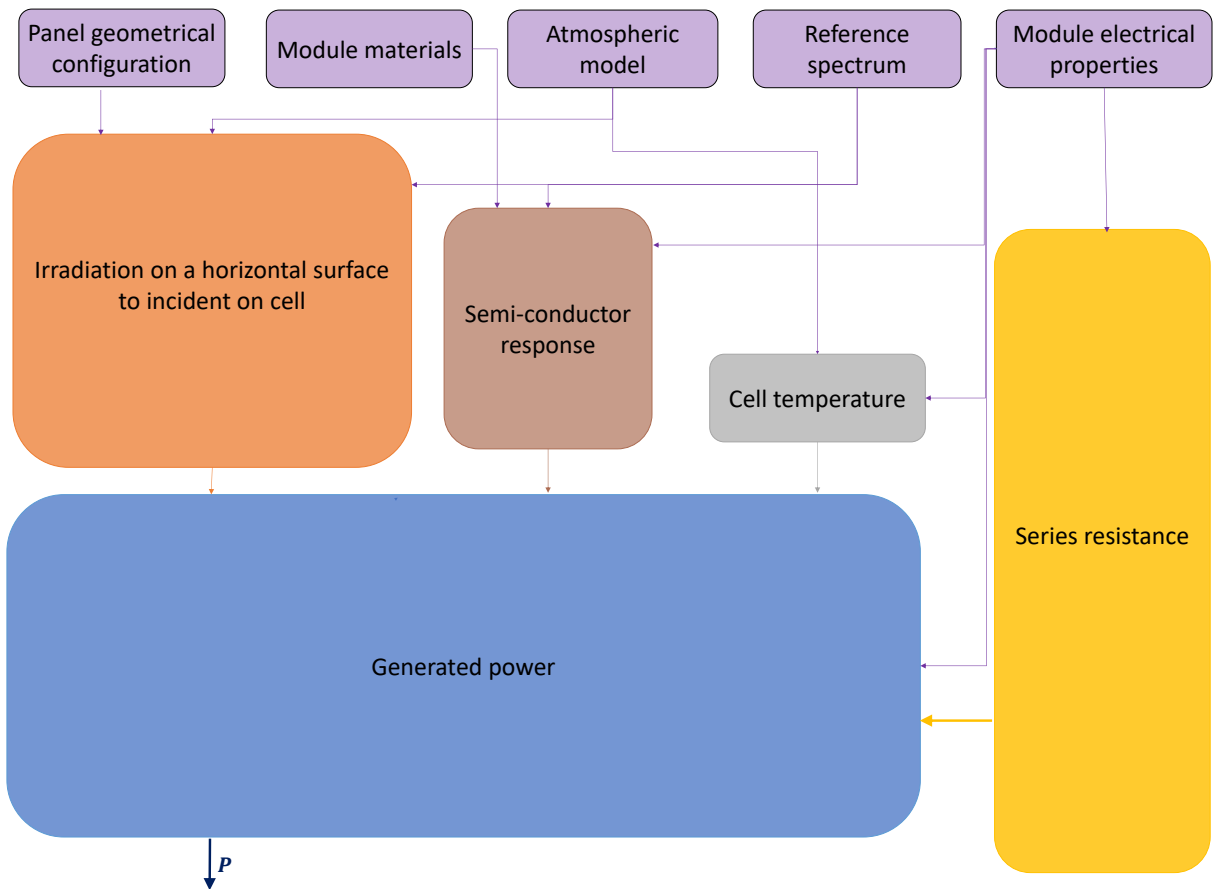


Figure 4.1.1: Simplified diagram of the PV code

4.2 Description of the subcomponents and the different options available

The additional variables are voluntarily modeled as physically as possible. The following describes briefly the main steps but the reader is referred to Appendix D for further details.

4.2.1 Cell-impacting irradiance

Modelling the spectral irradiance impacting the solar cells implies :

- Adding spectral resolution to the band simulated or measured direct and diffuse horizontal irradiances (to be able to apply a spectral response),
- Computing the spectral POA irradiance from those on a horizontal surface which is a process called transposition,
- Applying optical losses, to account for reflection at the surface of the panel and absorption of all layers preceding the solar cell.

4.2.1.1 Spectralisation

The spectralisation step is important due to the sensitivity of the solar cell to the wavelength. The irradiances, whether output by atmospheric models or measured, generally correspond to broadband values (*i.e.* integrated over the SW) or in the best case to narrow bands (like the six bands which can be retrieved from Meso-NH). However, in both cases, the spectral resolution is not fine enough to directly apply the spectral characteristics of the solar cell as the sharp cut of the spectral response at λ_{gap} does not necessarily match the boundary of a numerical band. The spectralisation step therefore aims at specifying the distribution of irradiance within the bands provided.

Accounting for the spectral resolution The ASTM G173-03 spectrum is the reference for the STC. Yet, it considers a specific state of the atmosphere whereas the surface irradiance spectrum is strongly variable with the air mass (or solar zenith angle SZA).

Furthermore, the ASTM G173-03 spectrum considers the irradiance on an inclined surface $\beta_{\text{STC}} = 37^\circ$ meaning that the transposition step has already been applied, and the spectrum for a different inclination would be different due to a change in contribution of the different subcomponents. A more optimal approach thus consists in spectralising the direct and diffuse irradiance separately on a horizontal surface, then applying the chosen transposition model to obtain the spectralised POA irradiance. Spectralising the direct and diffuse irradiances thus requires other reference spectra.

Figure 4.2.1 shows the different MODTRAN-simulated spectra for various SZAs under clear-sky (USSA conditions). Figure 4.2.1b corresponds to the spectra normalised by the total irradiance on the domain that silicon cells are sensitive to and highlights that the irradiance is not identically distributed over the wavelengths with varying SZA. This observation must therefore be accounted for in PV modelisation.

In order to account for the influence of SZA on the irradiance, spectral resolution is added to the direct and diffuse radiation by considering MODTRAN spectra simulated under USSA with the solar zenith angle ranging from 5° to 85° with an angle resolution of 5° . MODTRAN radiative transfer code provides both direct and diffuse irradiance at a high spectral resolution.

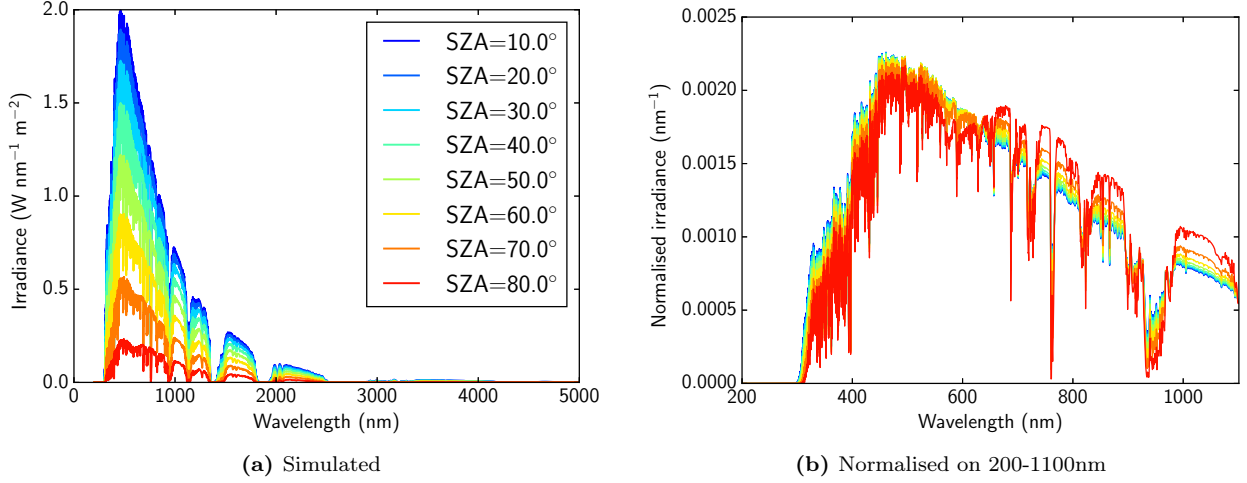


Figure 4.2.1: MODTRAN-simulated spectra considering the USSA conditions with SZA varying between 10 and 80° and the same spectra normalised by their integral between 200nm and 1100nm.

The spectrum considered for the spectralisation is the SZA-interpolated spectrum from the eighteen simulated spectra. This hypothesis of linear behaviour for a SZA variation of less than 5° is conformed by Figure 4.2.2 which illustrates for different wavelengths the evolution of global spectral irradiance with SZA.

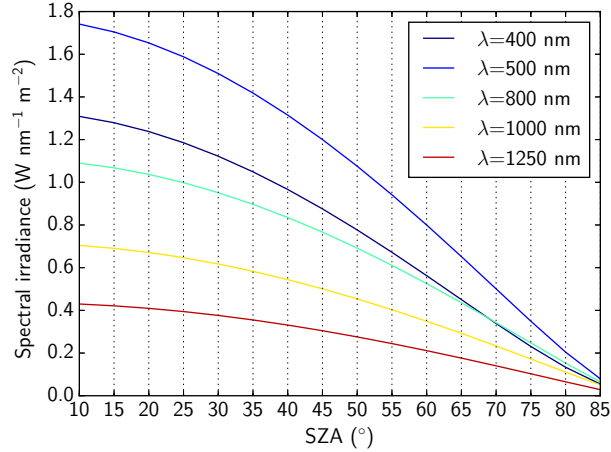


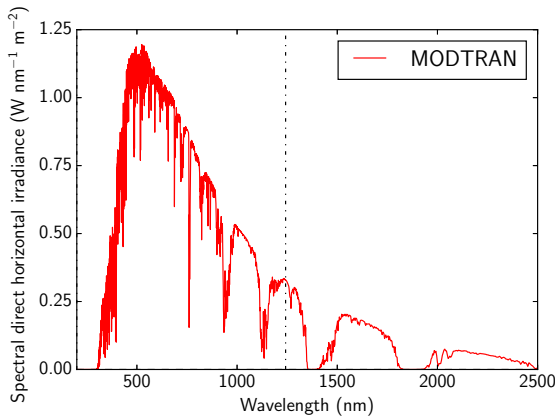
Figure 4.2.2: Global spectral irradiance for different wavelengths and solar zenith angles.

Applied method Given that the spectral signature is different for direct and diffuse radiation, both components are spectralised independently by considering the reference direct (resp.diffuse) component of the reference spectrum.

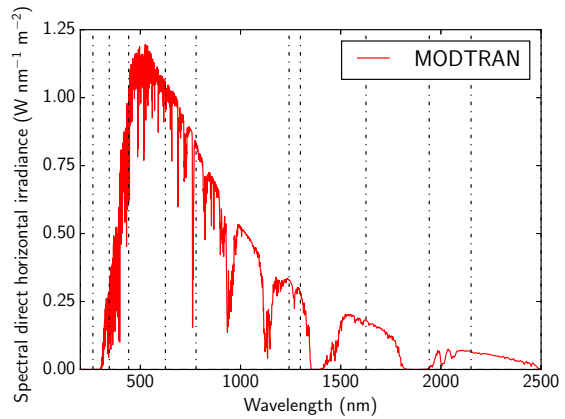
First, the reference spectrum G_{ref} is computed given the SZA by interpolating the MODTRAN spectra considering only the direct (or diffuse) component (Figure 4.2.3a). The irradiance to be spectralised corresponds to the integration over a wavelength domain $I_k = [\lambda_k; \lambda_{k+1}]$ (Figure 4.2.3b). This integrated value is spectralised by considering for $\lambda \in I_k = [\lambda_k; \lambda_{k+1}]$:

$$G(\lambda) = G(I_k) \cdot \frac{G_{ref}(\lambda)}{\int_{\lambda_k}^{\lambda_{k+1}} G_{ref}(\lambda) d\lambda} \quad (4.2.1)$$

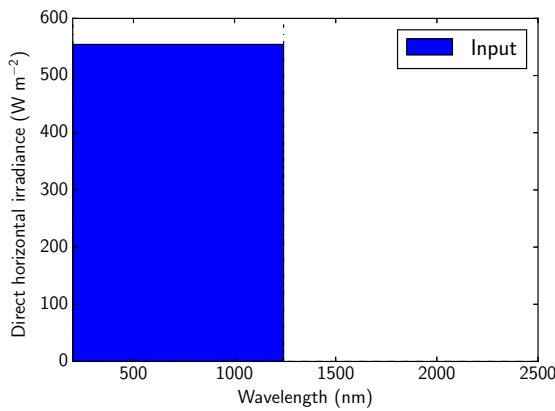
which leads to a spectrum of the same resolution and shape as the reference spectrum but with



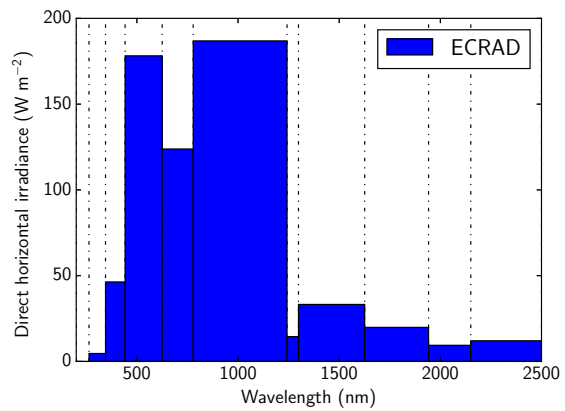
(a) Reference spectrum given the SZA



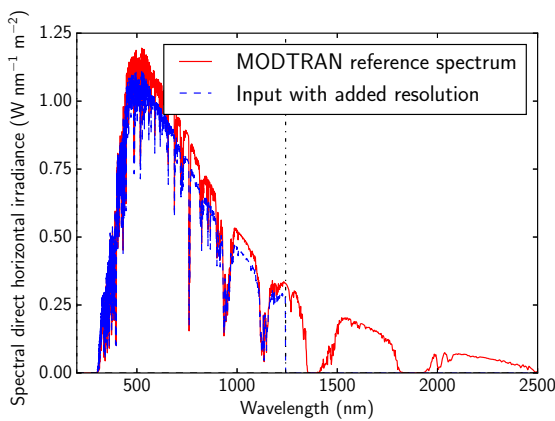
(a) Reference spectrum given the SZA



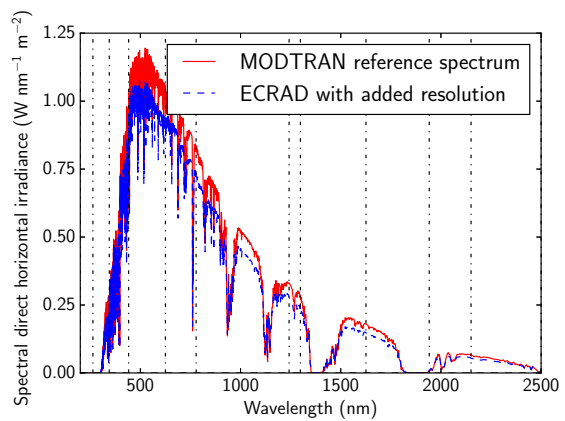
(b) Given irradiance



(b) Given irradiance



(c) Spectralisation



(c) Spectralisation

Figure 4.2.3: Spectralisation method for a global irradiance. The example for an irradiance measured over 200-1100nm is given.

Figure 4.2.4: Spectralisation method for given spectral irradiance. The dotted lines correspond to the different bands measured

the same integrated irradiance as the input (Figure 4.2.3c).

In the case of spectral irradiances given for different bands, the method is the same by treating each band independently, as shown in Figure 4.2.4. This spectralisation thus does not aim at correcting the reference spectrum to the integrated value of the input irradiance, but rather to add information to the input on the relative spectral distribution within each band.

4.2.1.2 Transposition

The POA irradiance results from the contribution of the beam, the ground-reflected and the diffuse component (*Reindl et al. 1990a*) as illustrated by Figure 4.2.5. Irradiance inputs are generally provided for a horizontal surface, such that transposition models are required.

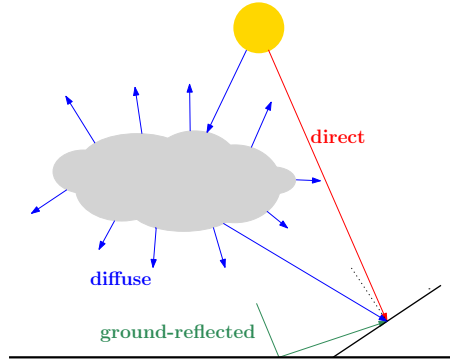


Figure 4.2.5: Contribution of direct, diffuse and ground-reflected irradiance to POA irradiance

The contribution of the direct component is straightforward whereas isotropic hypothesis is commonly assumed for reflected component (*Duffie & Beckman 2013*). The diffuse component is more intricate to model as it depends on the position of the Sun, and consequently on space and time. It is generally modeled by considering the three subcomponents (*Reindl et al. 1990a*, *Loutzenhiser et al. 2007*) illustrated in Figure 4.2.6:

- a circumsolar diffuse subcomponent, which is due to the predominant forward scattering of solar radiation in the atmosphere by the aerosols;
- a horizon brightening subcomponent, which translates a higher diffuse radiation near the horizon due to an increase in radiation scattering and multiple internal reflection for long path lengths through the atmosphere;
- an isotropic diffuse subcomponent, which corresponds to the remaining irradiance and is assumed to be uniformly distributed over the sky dome.

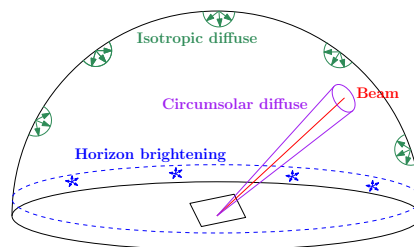


Figure 4.2.6: Different subcomponents of the sky-scattered irradiance and beam irradiance

The diffuse radiation on a tilted surface can be estimated by many transposition models, six of which are considered in the following. In all six of these models, the beam and ground-reflected components are treated as presented here-above (unless specified otherwise) but do

not all consider the three diffuse subcomponents. These models are presented in order of complexity:

- Isotropic (2D) model is the simplest model, it assumes that all the diffuse radiation is uniformly distributed over the sky dome and all sky elements are only defined by the zenith angle. In this 2D approach, the azimuth angle is therefore not taken into account (*Badescu 2002, Duffie & Beckman 2013*).
- Isotropic 3D model (*Badescu 2002*) also assumes isotropic radiation but both azimuth and zenith angle of the radiance are considered contrary to the 2D model. With this model, the ground-reflected irradiance is also assumed 3D isotropic;
- Klucher model aims at correcting the errors in overcast skies under the isotropic model by adding a clearness index *Klucher (1979)*;
- Hay-Davies model also accounts for the circumsolar subcomponent (*Davies & Hay 1980*);
- Reindl model takes into account all isotropic diffuse, circumsolar radiation and horizontal brightening, (*Reindl et al. 1990a*);
- Perez model considers empirically derived coefficients, as tabulated in *Perez et al. (1987, 1990)*, aiming at better modelling all three subcomponents. Only the coefficients provided in *Perez et al. (1990)* will be considered in the following.

4.2.1.3 Optical losses

Once the POA irradiance computed, optical losses must be applied as they result in an increased loss in power at high angles-of-incidence. These optical losses should account for two phenomena:

1. the losses due to reflection at each interface;
2. the losses due to the absorption of each layer.

After investigation, four optical models are considered,

- two theoretically derived from optical laws:
 - “Air-glass and absorption reflection” (as in *De Soto et al. (2006)*)
 - “Air-glass reflection” (as advised by *Sjerps-Koomen et al. (1996)*)
- two models based on empirical values for $a_r = 0.157$ (Air/Glass/Si) and $a_r = 0.17$ (typical value for m-Si modules with clean surfaces) in *Martin & Ruiz (2001)*

Martin & Ruiz (2001) distinguishes the different components (beam, scattered, ground-reflected) whereas the two other models provide a method to compute the transmitted irradiance as a function of the angle of incidence. These two methods are applied with the angle-of-incidence of the beam irradiance, and the effective beam irradiance incidence angle of diffuse and ground-reflected irradiance as defined by *Brandemuehl & Beckman (1980)*. In all cases, the optical losses are assumed to be independent of wavelength as justified in (*Sjerps-Koomen et al. 1996*).

4.2.2 Spectral response

As a reminder, the quantum efficiency with an ideal approach is defined by (2.2.16), whereas the spectral response is derived from (2.2.18)

4.2.2.1 Modelled quantum efficiency and spectral response

As explained in Part 2.2.7 and illustrated in Figure 4.2.7, the quantum efficiency is far from being ideal.

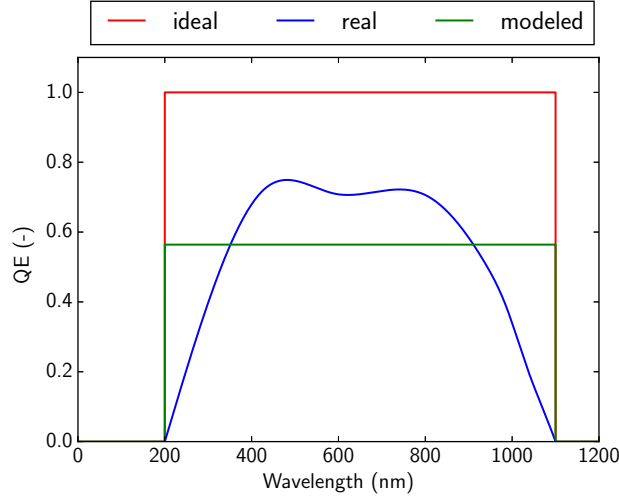


Figure 4.2.7: Ideal, real and modelled quantum efficiency of a solar cell.

Without any further information on the shape of the QE curve, the quantum efficiency can be modelled with a constant value:

$$QE_{\text{modeled}}(\lambda) = \alpha \times \mathbf{1}_{\lambda < \lambda_{\text{gap}}}, \quad (4.2.2)$$

meaning

$$SR_{\text{modeled}}(\lambda) = \alpha \times SR_{\text{ideal}}(\lambda). \quad (4.2.3)$$

This constant α is chosen such that the density current is correctly computed with the cell-impacting irradiance $G_{c,\text{ASTM}}$ resulting from an incoming ASTM reference spectra in the plane-of-array. In other terms, it must satisfy:

$$\int SR_{\text{real}} G_{c,\text{ASTM}} d\lambda = \int SR_{\text{modeled}} G_{c,\text{ASTM}} d\lambda \quad (4.2.4)$$

$$\Leftrightarrow \alpha \int SR_{\text{ideal}} G_{c,\text{ASTM}} d\lambda = J_{\text{SC,STC}}. \quad (4.2.5)$$

The constant can therefore be deduced thanks to the STC conditions following :

$$\alpha = \frac{J_{\text{SC,STC}}}{\int SR_{\text{ideal}} G_{c,\text{ASTM}} d\lambda} \quad (4.2.6)$$

which can be computed thanks to $J_{\text{SC,STC}}$ provided by the manufacturer, the modelled SR_{ideal} based on the type of PV cell and $G_{c,\text{ASTM}}$ (see Part 4.2.2.2). This constant remains however dependent on the module considered, as the ideal spectral response only relies on λ_{gap} which is technology-specific, and $J_{\text{SC,STC}}$ is specified by the manufacturer for a given module.

4.2.2.2 Reference spectrum incident to the cell

The calculation of the corrected quantum efficiency (or spectral response) requires the cell-impacting irradiance under STC $G_{c,ASTM}$, the cell-impacting irradiance being the POA irradiance after applying the optical losses. Yet, the provided ASTM G173-03 spectrum corresponds to the POA irradiance. As the optical losses depend on the nature of the radiation (direct, diffuse or ground-reflected) an optical loss cannot be directly determined for the POA irradiance. Consequently, the MODTRAN equivalent spectrum for STC is used to compute the overall optical losses in STC following the optical loss option chosen, which is then applied to the ASTM G173-03 spectrum.

4.2.3 Cell temperature

Three options to compute the cell temperature are available:

- a “simple model”, which only considers the cell temperature dependence on ambient temperature and POA irradiance :

$$T_c = T_a + \frac{G_{POA}}{G_{NOCT}} \cdot (NOCT - T_{a,NOCT}) \quad (4.2.7)$$

- *King et al. (2004)* model, which first computes the module temperature from the ambient temperature, POA irradiance and wind speed thanks to empirically fitted coefficients tabulated in *King et al. (2004)* then applying an empirically defined temperature difference to deduce the cell temperature. This model includes six “submodels” due to six possible set of fitted coefficients;
- *Skoplaki et al. (2008)* model, which is based on the energy balance of the PV module and a hypothesis on the thermal loss coefficient U_L . This model has further been derived into four “submodels” as explained in Appendix D.3.3.

It is to be noted that a model including the effect of wind is preferable since *Huld & Amillo (2015)* observed a change in performance by over 5% in hot windy areas due to the cooling effect of wind.

4.2.4 Series resistance

The series resistance R_s is required to compute the fill factor, as mentioned in the previous part. As a first approximation, the series resistance is assumed constant (*Lorenzo 2003*), meaning that R_s can be retrieved from a known value of FF by inverting the *Green (1982)* model used.

This method can be applied as the fill factor is known in STC thanks to the $I_{SC,STC}$, $V_{OC,STC}$ and $P_{MPP,STC}$ provided by the manufacturer datasheet, given the definition of the fill factor (2.2.8):

$$FF_{STC} = \frac{P_{MPP,STC}}{I_{SC,STC} \times V_{OC,STC}} \quad (4.2.8)$$

4.3 Overview

To summarize, Figure 4.3.1 provides an overview on how the photovoltaic model works via its subcomponents.

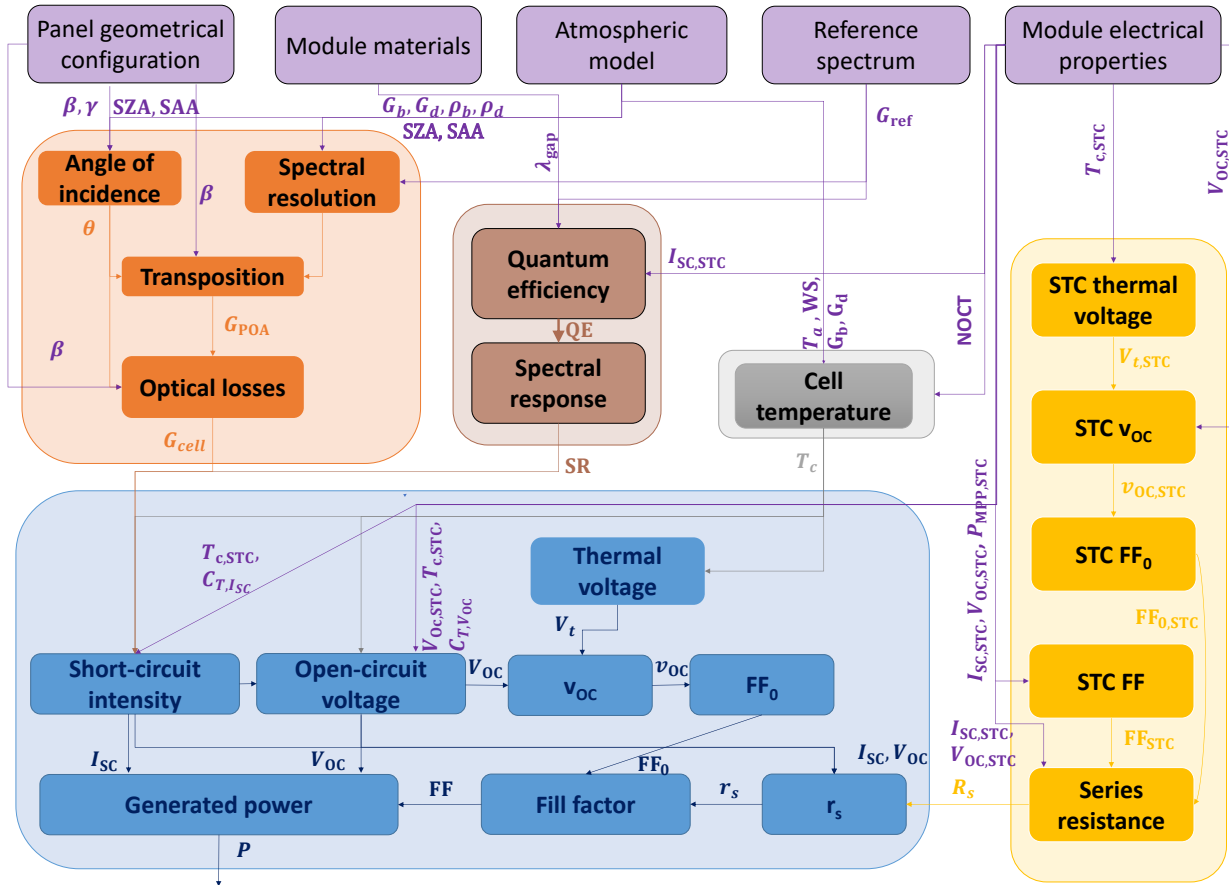


Figure 4.3.1: Detailed diagram of the PV code

Also, the PV model has been put into a user-friendly format so that it can be used as a black box. This user-friendly version is constituted of (Figure 4.3.2):

- Three “packages” constituting the toolbox with all the required functions;
- A main function which calls the functions in the correct order and passes on the computed variables (MAIN_FUNCTION.py). The outline of the main function is therefore summarised in Figure 4.3.1 here above;
- Three namelists: one to define the characteristics of the module (MY_MODULE.py), one to choose the options to be used (NAMELIST.py), and one to provide a description of the atmospheric conditions (MY_ATM.py);
- A main script importing the namelists, launching the main function, and saving the computed power (MAIN.py).

Figure 4.3.2 also recalls the variables required as an input for the PV model

The options available that are to be specified in NAMELIST.py are summarised in Table 4.3.1. The POA “DEFAULT” option is a hybrid option which has been added following the calibration presented in Part 5.

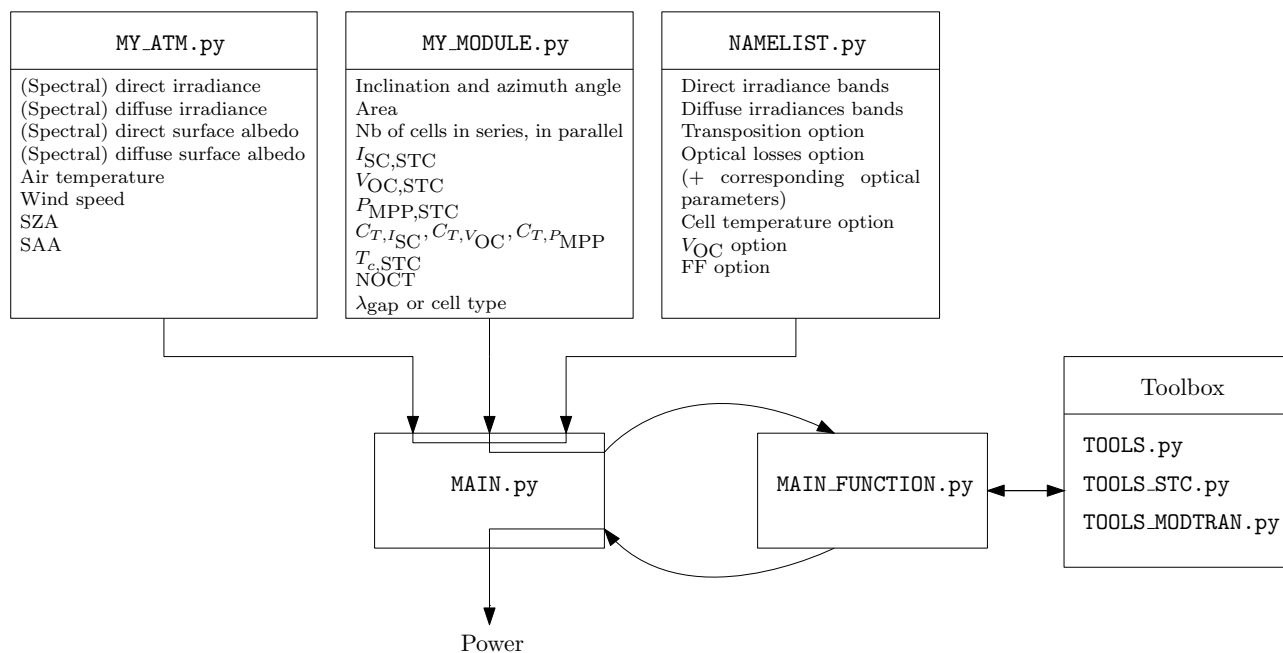


Figure 4.3.2: Structure of the user-friendly version of the PV model

Table 4.3.1: Available options in the developed PV model

Process	Options	Required specifications
POA	DEFAULT ISOTROPIC (<i>e.g.</i> Badescu (2002) , Duffie & Beckman (2013)) KLUCHER (Klucher 1979) HAY-DAVIES (Davies & Hay 1980) REINDL (Reindl et al. 1990a) PEREZ (Perez et al. 1990) ISOTROPIC3D (Badescu 2002)	
Optical losses	Reflection_Absorption (De Soto et al. 2006) Reflection (Sjerps-Koomen et al. 1996) Martin (Martin & Ruiz 2001)	n0, n1, K, L n0, n1 ar, c1, c2
Module temperature	King (King et al. 2004) Skoplaki (Skoplaki et al. 2008) simple (<i>e.g.</i> (Skoplaki et al. 2008))	mount_type_King (between 0 and 5)
V_{OC}	I0 (adapted from Singh & Ravindra (2012)) STC	
FF	simple (Green 1982) complex (Green 1982)	

VALIDATION OF THE PHOTOVOLTAIC MODEL

This part achieves the double objective of calibrating and validating the PV model. It is first evaluated as thoroughly as possible by decomposing the model into the smallest subcomponents possible and comparing all the measured variables by the SIRTAs in June 2017 to those simulated with the PV model. At each step proposing several options, the performances are compared and the best option is set as default, yielding a calibrated PV model. This latter is then validated thanks to an independent set of measurements obtained at SIRTAs in December 2017.

5.1 Calibration and evaluation of the PV model

5.1.1 Methodology

In order to calibrate and assess the accuracy of the PV model, the simulated variables must be compared to the measured ones. The measurements of June 2017 at the SIRTAs are used for this calibration. The model is decomposed into the smallest subcomponents that can be tested given the available measurements reminded in Figure 5.1.1 and enables, when different options are available, the choice of the one to be applied by default. This validation by parts allows the PV model to be the most accurate physically speaking. It therefore differs from statistical approaches where the whole model is considered as a black box and the target is to minimize the error of the final output, regardless of the physical relationships between variables. A statistical approach is therefore dependent on the localisation, the module but also the source of the inputs as their bias is implicitly corrected. On the contrary, the approach in this project enables a PV model which is aimed at being independent of the module and origin of the inputs as physical models are applied.

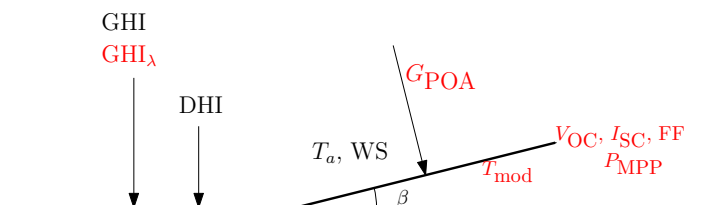


Figure 5.1.1: Measurements available from the SIRTAs in June 2017 for the PV model evaluation and calibration. Variables in red correspond to those which can be compared to modelled variables whereas those in black are only used as inputs. GHI_λ corresponds to the spectral irradiances measured by the spectrometre.

A change in behaviour of the PV module as irradiance decreases occurs ([Mavromatakis et al. 2017](#)), such that observations with $G_{POA,measured} \leq 200 \text{ W m}^{-2}$ are discarded. The dataset con-

tains 4177 observations of which only 1764 verify the criteria on $G_{\text{POA,measured}}$.

To validate each subcomponent of the PV model, several errors are computed. The error variable x' for any variable x is defined by the difference between the simulated and real variable:

$$x' = x_{\text{sim}} - x_{\text{real}} \quad (5.1.1)$$

and the mean operator is denoted by $\langle \cdot \rangle$. The errors considered are:

- the Mean Bias Error (MBE):

$$\text{MBE} = \langle x' \rangle \quad (5.1.2)$$

- the Mean Relative Error (MRE):

$$\text{MRE} = \left\langle \frac{x'}{x_{\text{real}}} \right\rangle \quad (5.1.3)$$

which is highly sensitive to small errors for small values, whereas accurate solar power production is mainly required when the power is high;

- the Root Mean Square Error (RMSE):

$$\text{RMSE} = \sqrt{\langle x'^2 \rangle} \quad (5.1.4)$$

which does not allow for compensation of positive and negative biases and gives more weight to the largest errors;

- the STandard Deviation (STD) of the error evaluates the dispersion of the error variable x' about its mean value:

$$\text{STD} = \sqrt{\langle (x' - \text{MBE})^2 \rangle} = \sqrt{\text{RMSE}^2 - \text{MBE}^2} \quad (5.1.5)$$

A STD close to zero means that the error is more or less constant such that it can easily be corrected.

In reality, one does not have access to the real variables but to observations, thus including measurement uncertainties. Without any further information on these uncertainties, one can assume white noise, meaning:

$$\langle x_{\text{obs}} - x_{\text{real}} \rangle = 0 \quad (5.1.6)$$

Certain errors such as the MBE and the RMSE will therefore not be influenced by the errors in measurements whereas others will be.

5.1.2 Cell-incident irradiance calibration

5.1.2.1 Spectralisation

The measured dataset includes 1min-spectral irradiances measured with 1nm resolution for the three clear-sky days. The error induced by spectralisation can be assessed by comparing the measured spectral irradiance and the sum of the spectralised direct and diffuse irradiances from the measured GHI and DHI (Figure 5.1.2). In order to partly correct the errors due to the difference in wavelength range, the simulated spectra is normalised over the spectral range of

the spectrometer to the integrated spectral irradiance measured. However, a bias due to the use of clear-sky days only is expected.

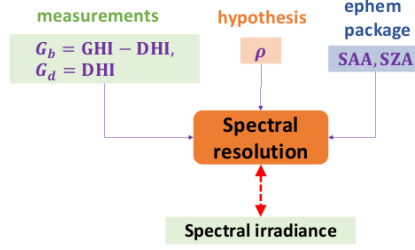


Figure 5.1.2: Methodology used to assess the accuracy of spectralisation method.

Figure 5.1.3 presents the results in the case of a particular timestamp. Though the measured and simulated distributions are not equal, the spectralisation step is shown to provide a realistic shape to the provided irradiance.

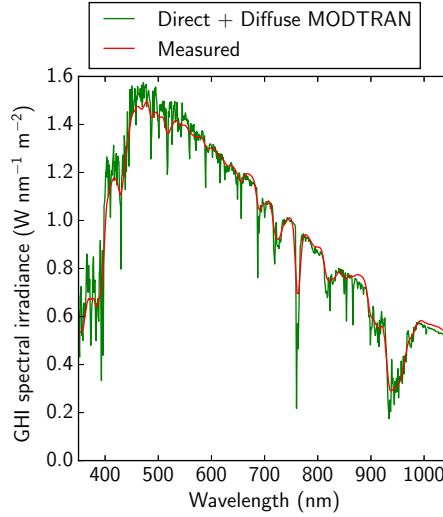


Figure 5.1.3: Comparison of the 10 minute-averaged measured spectral irradiance by the SIRTa on June 10 2017 at noon and the spectral irradiance deduced from the measured GHI and DHI by MODTRAN-spectralisation of direct and diffuse components brought to the same spectral resolution as the measurements.

The errors are estimated on the wavelength range of the spectrometer, *i.e.* 300–1050 nm. Table 5.1.1 provides the MRE and RMSE for the three days of data.

Table 5.1.1: MRE and RMSE due to spectralisation

MRE [-]	RMSE [W nm ⁻¹ m ⁻²]
0.0297	0.0020

5.1.2.2 POA irradiance

The default transposition method is chosen by comparing the measured POA irradiance to the one modelled thanks to the measured irradiances on a horizontal surface and the Sun position provided by ephem Python package (Figure 5.1.4).

As a reminder, the diffuse and ground horizontal irradiances are measured over 200–3600 nm contrarily to 300–3000 nm for the POA irradiances. This can easily be overcome by integration

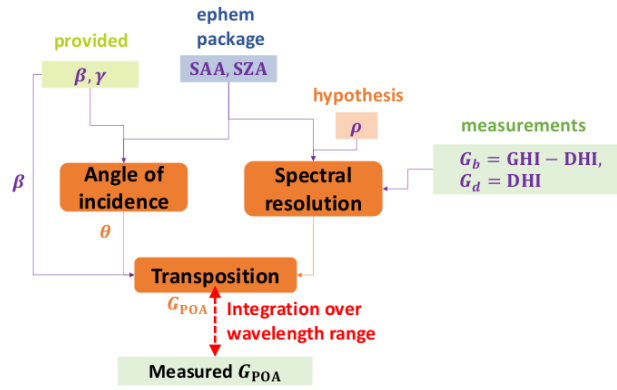


Figure 5.1.4: Methodology used to assess the accuracy of the transposition models.

over the appropriate domain which is enabled thanks to the previous spectralisation. For the different transposition methods, the maximum error that could have been induced if the spectral mismatch had not been corrected has been computed to be of 5%. Table 5.1.2 presents the errors in forecasted POA irradiance for all six methods. The isotropic 3D method performs the best for all criteria.

Table 5.1.2: Error in G_{POA} for the different transposition methods, for $G_{\text{POA, meas}} > 200 \text{ W m}^{-2}$

	Isotropic	Isotropic 3D	Klucher	Hay-Davies	Reindl	Perez
Mean relative error (%)	2,25	0,08	5,67	2,77	3,08	4,50
Mean error (W m^{-2})	9,33	-1,54	29,5	15,6	17,0	26,8
Mean absolute error (W m^{-2})	41,8	40,7	52,1	45,0	45,4	50,6
RMSE (W m^{-2})	70,9	70,8	77,7	73,9	74,0	77,9

However, considering global errors over the whole month of June introduces a bias as different SZAs do not have the same weight in the dataset whereas transposition methods can present varying accuracy with SZA. The performance of each model has thus been assessed for 5-degree width SZA bins, meaning that the errors are not influenced by the occurrence of each SZA. Only the bias is assessed as the relative error is highly sensitive to small errors at low irradiances and the final interest is on the total PV production.

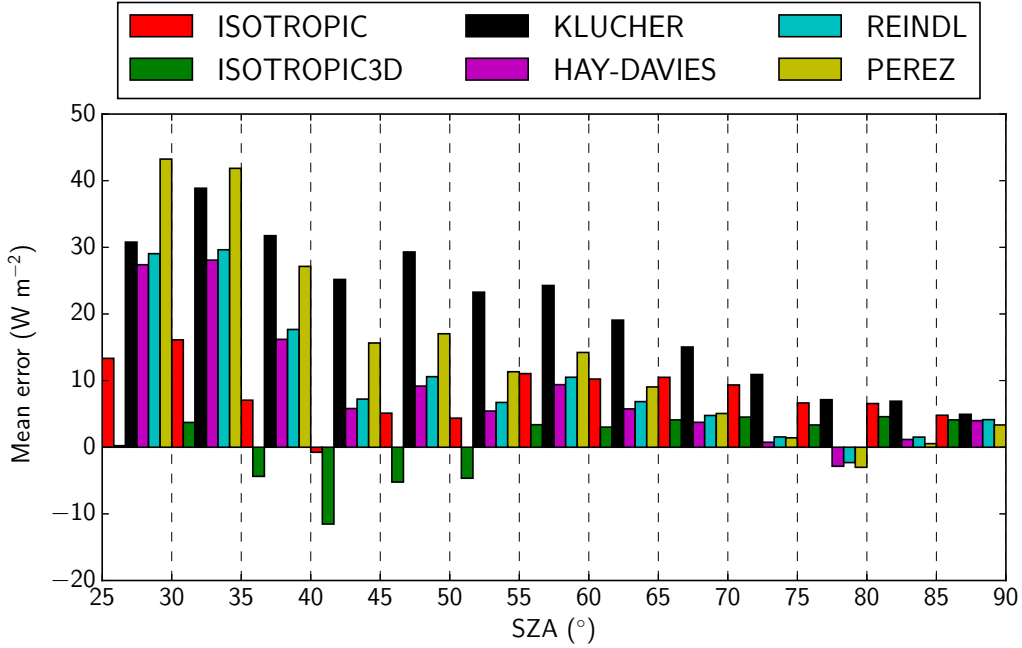
Figure 5.1.5 shows the errors in POA irradiance modelling for the different transposition models as a function of the SZA. It is to be noted that a selection criterium based on median or mean values does not lead to the same conclusion. Given that the mean is greatly influenced by outliers and considering the values taken by the first and ninth decile (provided in Figure 5.1.5), the median seems the most appropriate criteria. Consequently, the default methods applied in the PV model are:

1. 3D isotropic model for $\text{SZA} < 70^\circ$;
2. Perez model for $\text{SZA} \geq 70^\circ$.

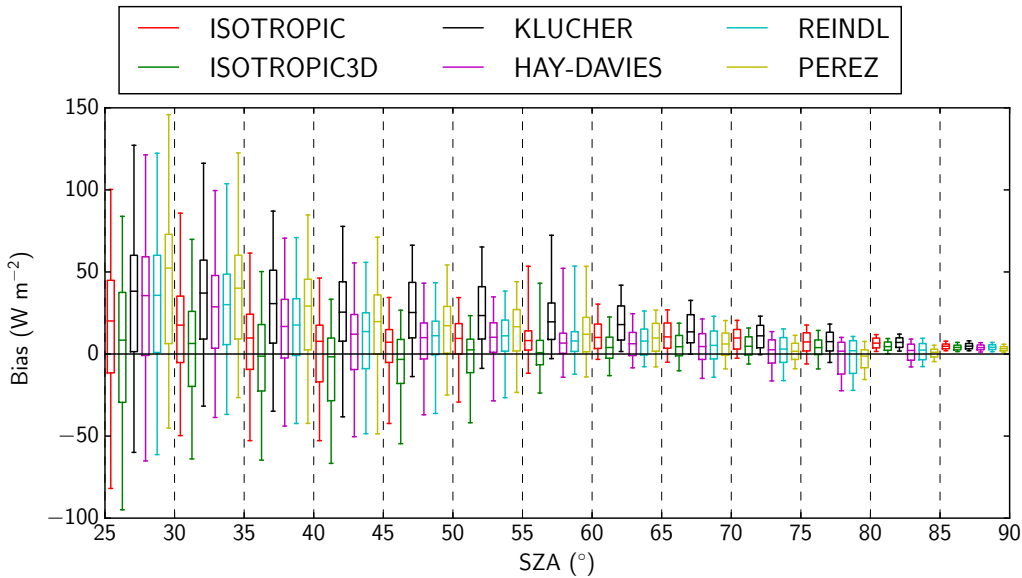
The Hay-Davies and Reindl models also perform well at high SZA, however, the errors are less dispersed with the Perez model, hence the choice mentioned above.

5.1.2.3 Optical losses

The optical losses models are first compared for the direct, diffuse and ground-reflected radiation separately, then globally in standard test conditions.



(a) Mean error



(b) Boxplot : D1,Q1,median,Q3,D9

Figure 5.1.5: Errors in POA irradiance modelling for different SZA.

The glazing extinction coefficient, the glazing thickness and the refractive index are set by default to $K = 4 \text{ m}^{-1}$, $L = 2 \text{ mm}$ and $n_1 = 1.526$ as in *De Soto et al. (2006)*. Figure 5.1.6 compares the optical losses for each subcomponent (beam, diffuse, ground-reflected). Following *Martin & Ruiz (2001)*, the transmission achieved at normal irradiance is 1 (meaning no reflection) whereas Fresnel law indicates $T = 1 - \frac{(1 - \frac{n_0}{n_1})^2}{(1 + \frac{n_0}{n_1})^2}$ which is approximately 0.956 with $n_1 = 1.526$ (and $n_0 = 1$ for air); which means that a loss of more than 4% is neglected with *Martin & Ruiz (2001)*.

The irradiance transmitted to the solar cell for a module in STC with varying solar zenith angle has been computed. As the overall optical losses depend on the fraction of direct/diffuse/ground-reflection irradiance, the global POA ASTM G173-03 spectrum cannot be applied. Consequently, the equivalent spectrum computed with MODTRAN is applied, after normalising

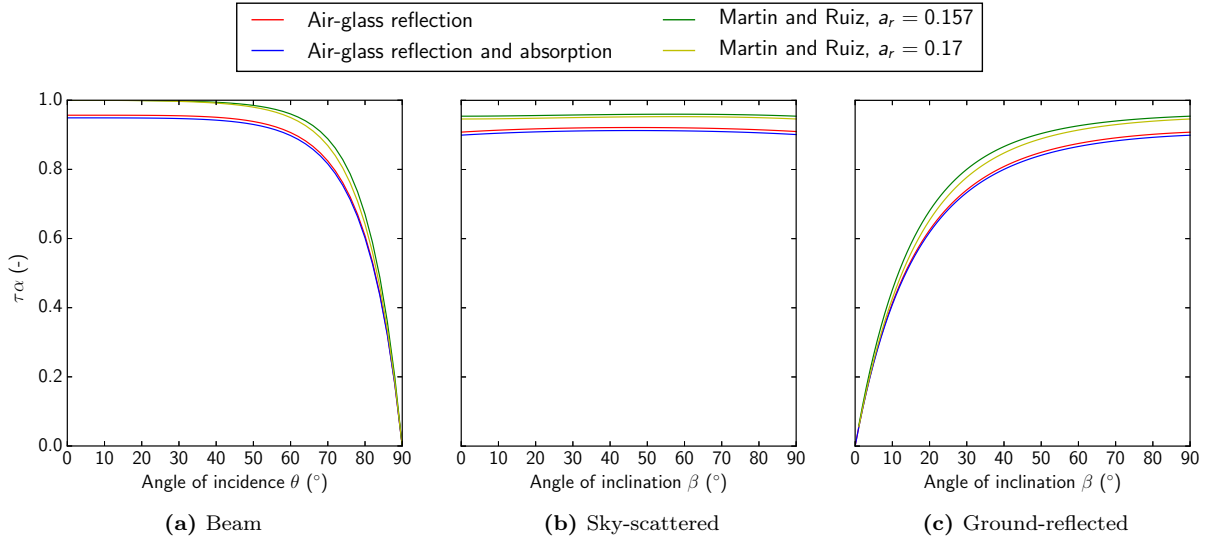


Figure 5.1.6: Absorption-transmission coefficient for the beam, sky-scattered and ground-reflected components considering the four optical losses methods

G_{POA} to 1000 W m^{-2} ¹. Figure 5.1.6 shows that the differences between the theoretical and empirical models are non-negligible.

Figure 5.1.7a indicates that when the identical optical losses method is applied to the current and standard test conditions, the normalised transmission coefficients are nearly identical at low SZAs and differences are little at higher angles. However, in the developed PV model, the cell-impacting irradiance is not directly normalised by STC and Figure 5.1.7b highlights the difference in models when not normalised by STC.

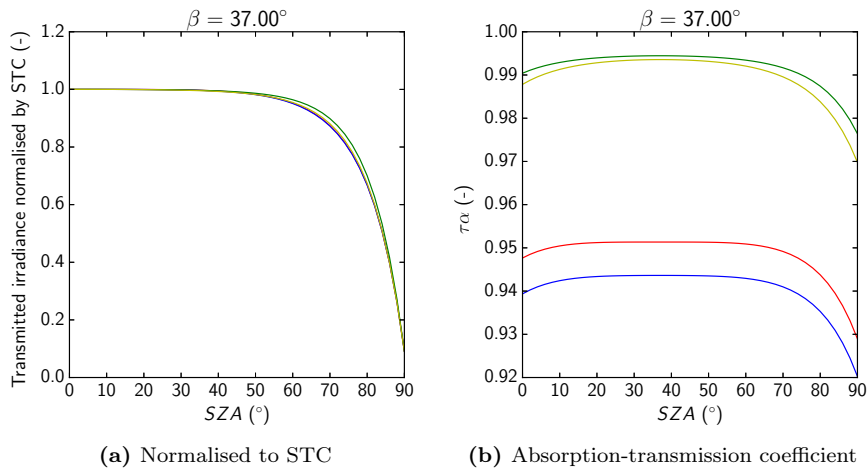


Figure 5.1.7: Modelled transmitted irradiance to the solar cell normalised to STC conditions for different methods considering the MODTRAN-equivalent ASTM G173-03 spectrum. Refer to the colour legend of the previous figure.

Given the fact that *Martin & Ruiz (2001)* is based on empirical values for silicon PV models, that it does not follow the physically expected results at normal irradiance as mentioned above and considering the wish to have a physical PV model, the choice for a physical optical loss model was made.

The difference between the “air-glass” models with and without absorption corresponds to

¹The integrated MODTRAN POA otherwise equals 1038 W m^{-2}

the absorption term $A_\alpha(\theta_r, \lambda) = \exp\left(-\frac{K(\lambda)L}{\cos(\theta_r)}\right)$ (D.2.37) which for the K and L chosen represent a reduction in transmission of 0.8 to 1% as the incident angle increases from 0 to 90°. The physical method based on air-glass reflection will be applied by default. This choice will also be checked with the evaluation of I_{SC} in Part 5.1.4.1.

5.1.3 Cell temperature modelling calibration

Three models to compute the cell temperature are studied and detailed in Appendix D:

- a “simple model”;
- King model (including six sets of empirical coefficients);
- Skoplaki models.

The models are tested on four PV modules. The France Watts module is used as a reference for illustrations as it is the most common module (c-Si), despite the fact that the NOCT is not given by the manufacturer and is assumed to be 45 °C which corresponds to the most common value for PV modules.

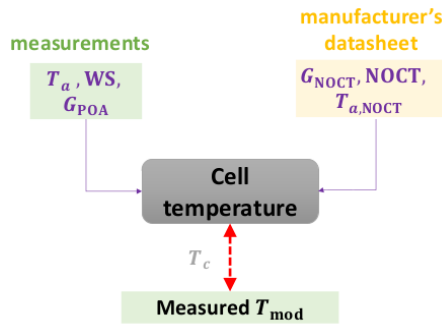


Figure 5.1.8: Methodology used to assess the accuracy of T_c models.

5.1.3.1 Choice of the King model parameters

King et al. (2004) computes the module temperature before deducing the cell temperature. Since temperature is measured at the back of the modules, the choice of the King empirical coefficients to apply is based on the comparison between the modelled module temperature and the measured temperature.

Figure 5.1.9 presents the modelled temperature compared to the measured values for the FranceWatts monocrystalline module for the different parameters, and is representative of all four modules. The sixth set of empirical coefficients is shown to be the only one allowing a good representation of high module temperatures as the other parametrisations lead to an important positive or negative bias as the temperature increases.

Table 5.1.3 shows that for all four modules, the best fitting parameters in terms of both bias and standard deviation are the sixth set of empirical coefficients which correspond to those for a tracker. Though this does not have any physical sense for this installation, it is the modelled applied in the following, unless mentioned otherwise. Furthermore, the standard deviation of the errors in temperature is not small enough to be able to correct these errors.

Figure 5.1.10 shows the error in modelled module temperature as a function of air temperature, wind speed and plane-of-array irradiance with the optimal King parameters. The module

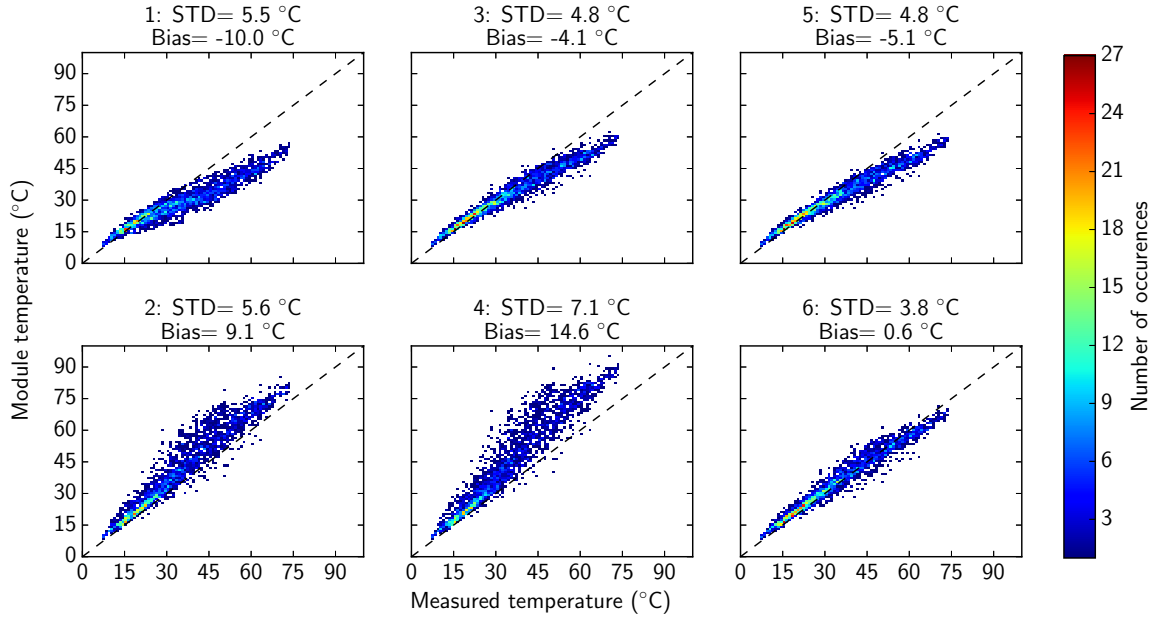


Figure 5.1.9: Modelled versus measured module temperature (FranceWatts monocrystalline module) depending on the empirical coefficients provided by *King et al. (2004)*. The numbering corresponds to the rows in Table D.3.1.

Table 5.1.3: Bias and standard deviation in module temperature for the six sets of King parameters and all four modules. The mount type numbering (1 to 6) refers to the rows in Table D.3.1

	Bias (°C)						Standard deviation (°C)					
	1	2	3	4	5	6	1	2	3	4	5	6
First Solar	-10,63	8,50	-4,77	13,93	-5,75	0,01	5,26	5,43	4,05	7,16	4,07	3,38
FranceWatts	-9,99	9,12	-4,14	14,55	-5,12	0,64	5,53	5,57	4,83	7,10	4,82	3,79
Panasonic	-24,73	-9,38	-19,88	-5,08	-20,67	-16,13	7,57	8,65	7,04	9,84	7,03	7,31
Sharp	-9,20	9,90	-3,35	15,32	-4,32	1,43	4,65	6,07	4,37	7,76	4,26	3,70

temperature seems to be underpredicted for higher POA irradiances, wind speed between 0.5 et 1 ms^{-1} and with increasing air temperatures. This is a global trend noticed for all four modules.

The previous analysis considers the measured wind speed as input for the King model. However, the wind-speed considered by *King et al. (2004)* is at 10m above ground WS_{10m} whereas the measurements WS are provided at 2m. Wind speeds at two different heights can be related by considering a wind power law profile:

$$WS_h = \left(\frac{h}{h_{ref}} \right)^\alpha WS_{h_{ref}} \quad (5.1.7)$$

Counihan (1975) indicates that the most likely value for typical rural terrain of α is $\frac{1}{7} \approx 0.143$. *Huld & Amillo (2015)* apply an exponent of 0.2 without justifying this choice. An investigation on the correct α to apply, adapted to the SIRTAsite, is presented in Appendix E. and indicates that each module leads to a different value whereas the α coefficient only depends on the terrain. Consequently, no correction of the wind speed with height is introduced in the PV model.

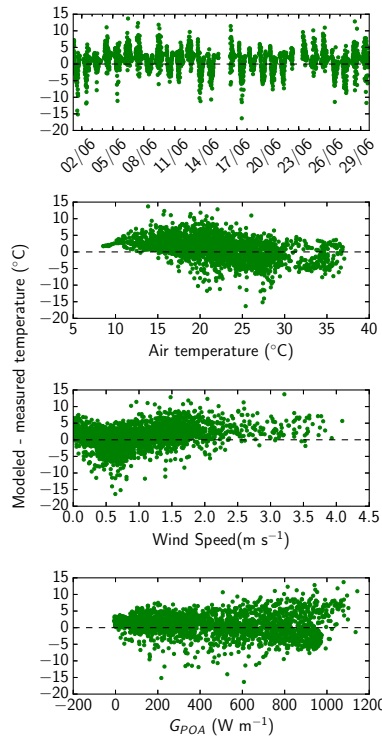


Figure 5.1.10: Error in module temperature as a function of the date, air temperature, wind speed and plane-of-array irradiance with the optimal King parameters (FranceWatts monocrystalline module)

5.1.3.2 Choice between the different Skoplaki models

Four different approaches are considered for the Skoplaki model in the PV model, named Skoplaki 1, Skoplaki 2, Skoplaki 2 constant and Skoplaki 2 irradiance in the following.

Table 5.1.4 shows the resulting bias and standard deviation for all four panels and is illustrated in Figure 5.1.11. The Skoplaki 1 and 2 have similar performances. Table 5.1.4 also indicates that the “Skoplaki 2 constant” model performs better for the FranceWatts module (m-Si module) but not for the other panels. The model accounting for the influence of irradiance on the cell efficiency is not satisfying, which may be due to the considered value of the intensity coefficient of cell efficiency γ . Given the fact that both “Skoplaki 2 constant” and “Skoplaki 2 irradiance” consider empirical values which are not necessarily representative of the modelled module and the observed biases and standard deviations, these alternative approaches will not be considered by default. The analysis of the RMSE and STD of all four panels shows a slightly better performance of the Skoplaki 2 model, which will therefore be chosen by default.

Table 5.1.4: Bias and standard deviation in cell temperature for the four Skoplaki models and all four modules.

Skoplaki model	Bias (°C)				Standard deviation (°C)			
	1	2	2 constant	2 irradiance	1	2	2 constant	2 irradiance
First Solar	-4,55	-4,60	-4,97	-6,42	3,66	3,63	3,84	4,05
FranceWatts	-4,92	-4,97	-4,34	-7,38	4,48	4,11	3,90	4,96
Panasonic	-21,55	-21,67	-20,25	-23,84	7,04	7,16	7,28	7,26
Sharp	-3,25	-3,30	-3,55	-4,67	3,72	3,23	3,22	3,58

The analysis of a correction of the NOCT to improve the Skoplaki model has been carried out but turned out non-satisfying, as explained in Appendix E.

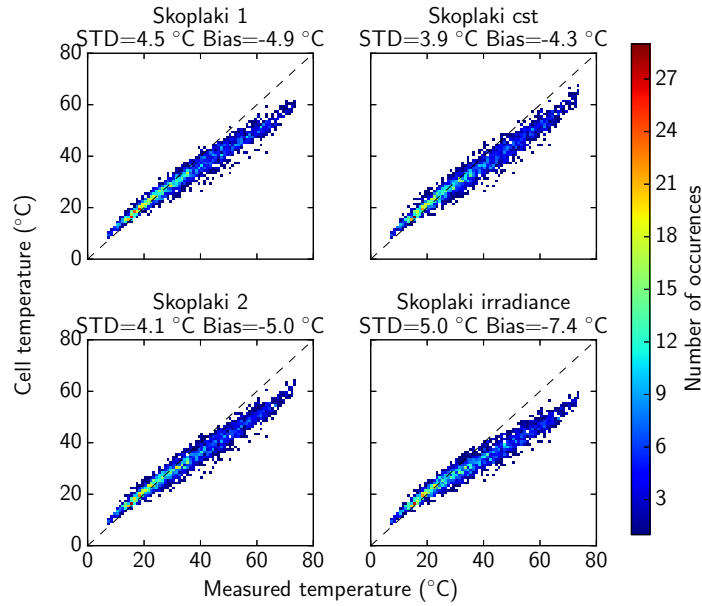


Figure 5.1.11: Modeled versus measured module temperature (FranceWatts monocrystalline module) depending on the Skoplaki model.

5.1.3.3 Default temperature model choice

The Panasonic (HIT) cell temperature is very badly modelled as indicated by the different biases and standard deviations computed above. This may be due to its high efficiency at high temperatures (“the HIT solar cell can maintain higher efficiency than a conventional crystalline silicon solar cell” according to the manufacturer).

Figure 5.1.12 compares all models considered (simple, King and Skoplaki) in the case of France Watts module and is representative of the other modules (except the Panasonic module). It is to be noted here that unlike previous figures, the cell temperatures and not the module temperatures are represented for the King model in Figure 5.1.12.

A positive bias of several degrees is expected due to the temperature difference between the module and the cell. King model is the only model with a positive bias, and considering the small difference between the modelled module temperature and measured temperature (bias $\leq 1.2^\circ\text{C}$) noted previously, the King model is chosen as the default model to be used.

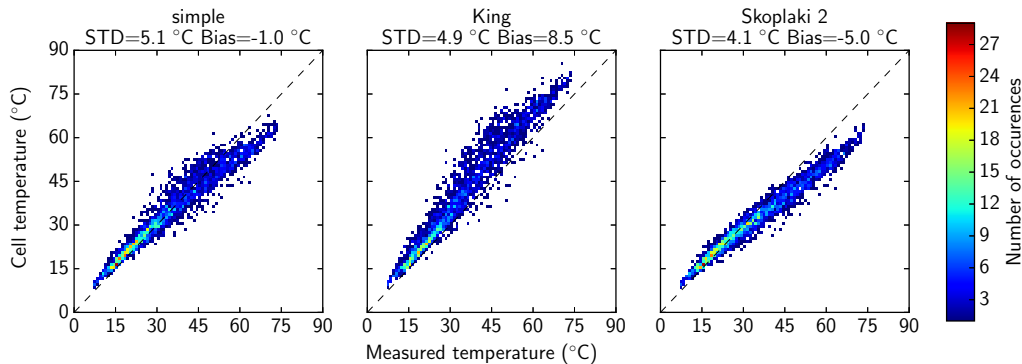


Figure 5.1.12: Modelled cell temperature versus the measured temperature for the different models considered for the France Watts module.

Improvements that could be studied for a better cell modelisation include :

- A better understanding of the measured wind speed and a refined estimation of the wind

speed at 10 m, the free stream and local wind speed;

- Access to measured cell temperature. The validation in this case is complicated by the fact the cell temperature is unknown and many models do not compute the module temperature as an intermediate step, meaning that the modelled and measured variables compared do not represent the same physical variable;
- A more precise study of the intensity cell efficiency coefficient instead of a default value, which is possible by analysing the information on the manufacturer datasheet.

5.1.4 From irradiance and temperature to power calibration

The computation of the electrical properties of the solar cell equivalent circuit are validated independently thanks to measured data alone. It is to be noted here that the measured module temperature is used, instead of the cell temperature which cannot be measured.

5.1.4.1 Short-circuit current

The generated photocurrent, which is assumed to be equal to the short-circuit current, can be calculated thanks to the measured device temperature and the incoming irradiance. This step requires the use of the spectral response model which cannot be validated as such but the accuracy of the chosen approach can be assessed with the short-circuit current. The position of the Sun is computed with the ephemeris Python package. This methodology is illustrated in Figure 5.1.13.

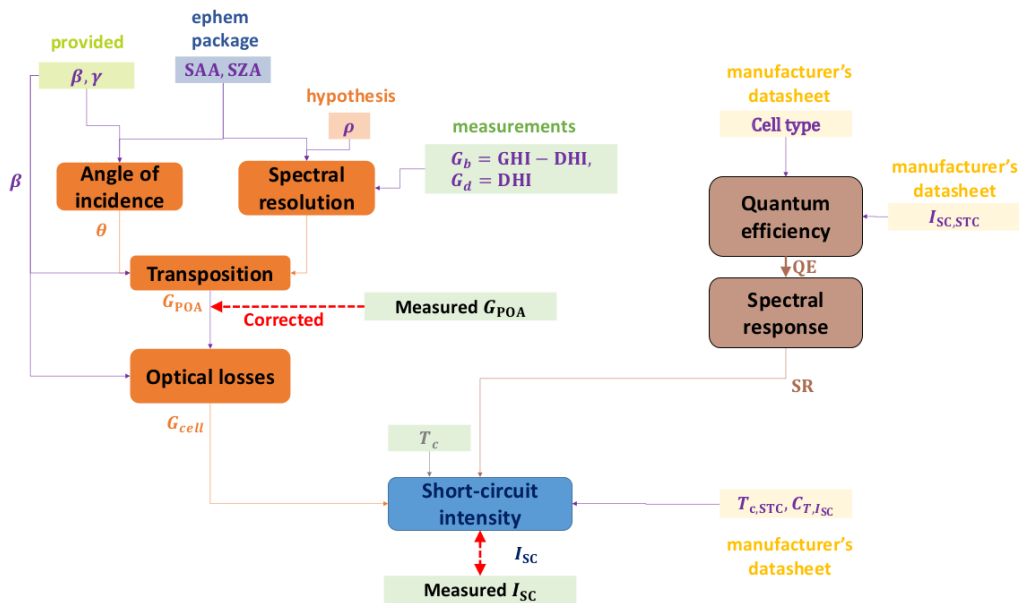


Figure 5.1.13: Methodology used for validating the I_{sc} modelling

Figure 5.1.14 illustrates the modelled and measured I_{sc} in the case of the FranceWatts module and the errors over the whole dataset are provided in Table 5.1.5. Comparing the modelled and measured I_{sc} enables to check the option set by default for the optical losses as I_{sc} is directly affected by the irradiance reaching the solar cell. If the reflection and reflection-absorption approaches lead to quasi-identical errors in I_{sc} , the model following *Martin & Ruiz (2001)* distinguishes itself just before sunrise and sunset, with higher I_{sc} *i.e.* lower optical losses which is coherent with the difference in transmittance between the models for SZA between 50

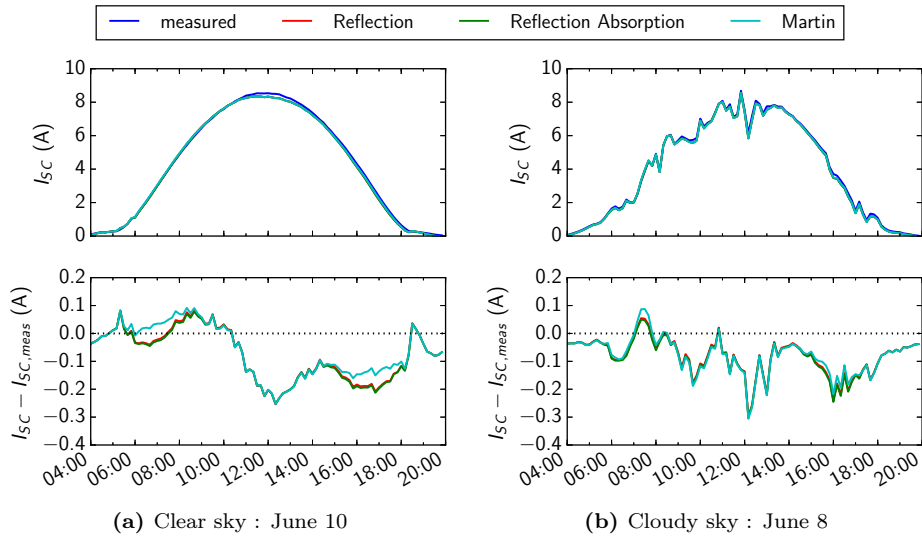


Figure 5.1.14: Simulated and measured I_{SC} of the module on a clear-sky and cloudy day

and 80° shown in Figure 5.1.7a. In terms of accuracy, this lowered optical loss can be beneficial or not depending on whether the irradiance is already under- or overestimated as seen in Figure 5.1.14a. The “reflection” default option is therefore not challenged.

Table 5.1.5: Error in I_{SC} of the module for the different optical losses methods.

	Reflection	Reflection-Absorption	Martin
Mean error (A)	-0,132	-0,136	-0,127
Mean relative error (%)	-2,89%	-2,98%	-2,65 %
RMSE (A)	0,259	0,260	0,259
STD (A)	0,222	0,222	0,226

The source of error in I_{SC} has been further investigated. The short-circuit current is mainly dependent on the spectral response and the incident irradiance. The POA irradiance is corrected to equal the measurements and the optical losses do not explain the difference between the simulated and measured I_{SC} . The errors must therefore originate from the spectral response.

The spectral response has been modelled under the ideal hypothesis. An approach based on trapezoidal-shaped quantum efficiencies has been carried out, in order to model better the real shape of quantum efficiency curves (Figure 2.2.7). Trapezoidal quantum efficiencies are generated for different slopes and a same amplitude of 1. These are then corrected by a constant similarly as in (4.2.4) such that $I_{SC,STC}$ is correctly computed, as shown in Figure 5.1.15a. The resulting short-circuit current are illustrated for a clear-sky and cloudy day in Figure 5.1.15. This investigation highlights the importance of the solar cell sensitivity to the photon wavelength, thus also pointing out the importance of a good knowledge of the spectral irradiances.

In the PV model, the hypothesis of ideal quantum efficiency is kept in order to limit the number of parameters to set. Furthermore, the slightly better accuracy of the *Martin & Ruiz (2001)* model does not justify the choice of this empirically based model compared to more physical models which can be more easily adjusted to a given module if enough information is provided.

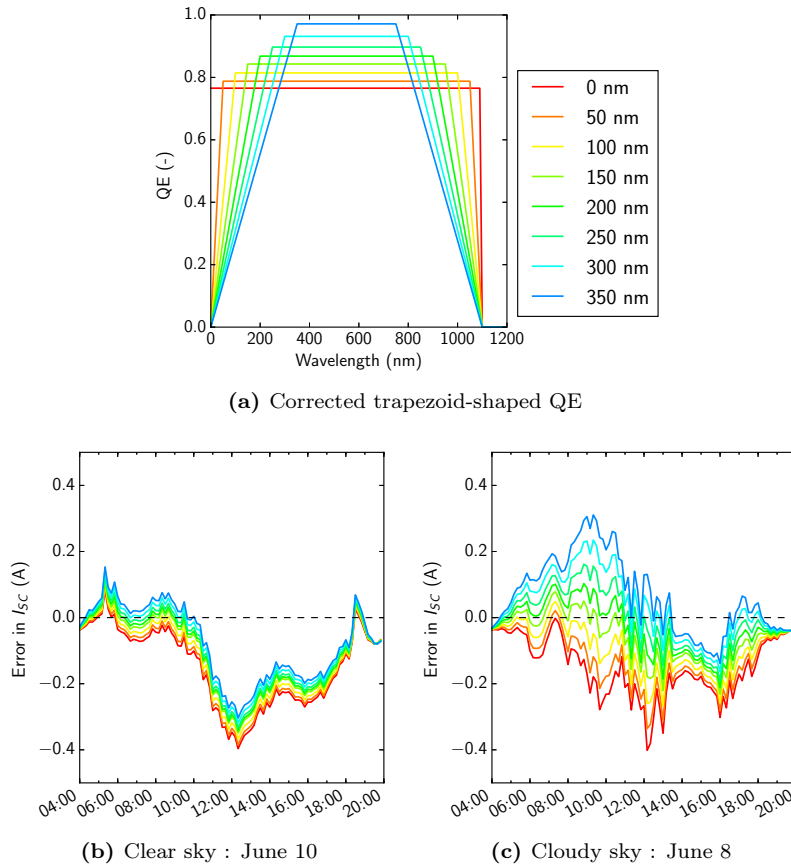


Figure 5.1.15: Difference between the simulated and measured I_{SC} on a clear-sky and cloudy day with trapezoidal quantum efficiencies. The legend given in Figure 5.1.15a corresponds to $\frac{1}{2}(b - a)$ with b and a the bottom and top base and is common for all subfigures, whereas the black line corresponds to the measured I_{SC} .

5.1.4.2 Open-circuit voltage

The open-circuit voltage is validated by considering measured data only following Figure 5.1.16. Two options are available and are compared during the validation.

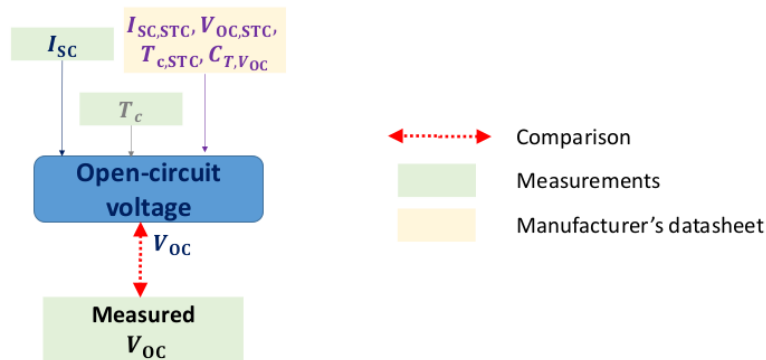


Figure 5.1.16: Methodology used for validating the V_{OC} modelling.

Table 5.1.6 indicates the errors in modelled V_{OC} for the simple method or the one based on the formulation of I_0 . If the MRE is closer to zero for the simple model, the I_0 method is more advantageous in terms of RMSE and STD.

Furthermore, Figure 5.1.17 shows the measured and the two modeled V_{OC} over a clear and cloudy day and shows that the I_0 is the most accurate between 8:00 and 16:00 which corresponds to the time of day where accurate PV power modelling is of interest, whereas both models tend

Table 5.1.6: Error in V_{OC} of the module for the two formulations.

	simple	with I_0
Mean error (V)	-0,117	0,157
MRE (%)	-0,364%	0,449%
RMSE (V)	0,388	0,229
STD (V)	0,370	0,167

to overestimate at sunrise and sunset. As the simple model otherwise underestimates, errors counterbalance over the period of simulation hence a smaller MRE.

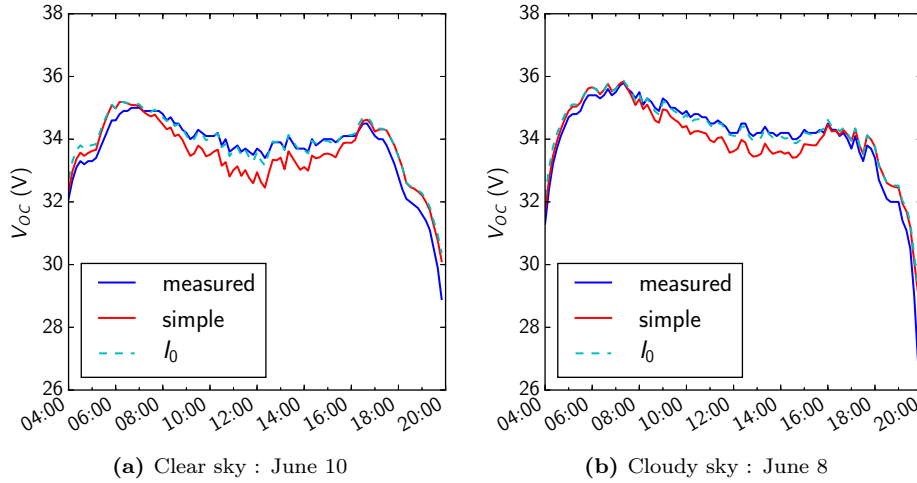


Figure 5.1.17: Simulated and measured V_{OC} of the module on a clear-sky and cloudy day

Therefore, the choice of default method should be based on the RMSE in this case; hence the choice of the I_0 method by default.

5.1.4.3 Fill factor

The fill factor is evaluated and calibrated by considering the measured values and the manufacturer’s datasheets only following the method described in Figure 5.1.18. When neglecting the shunt resistance, two approaches are possible, depending on the formulation of the fill factor. Figure 5.1.19 illustrates the simulated fill factors for a clear-sky and cloudy day whereas Table 5.1.7 provides the errors for each option.

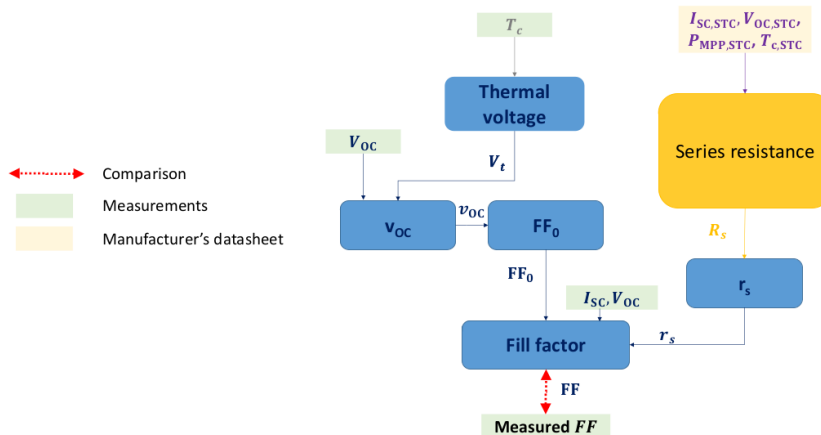


Figure 5.1.18: Methodology used for validating the FF modelling.

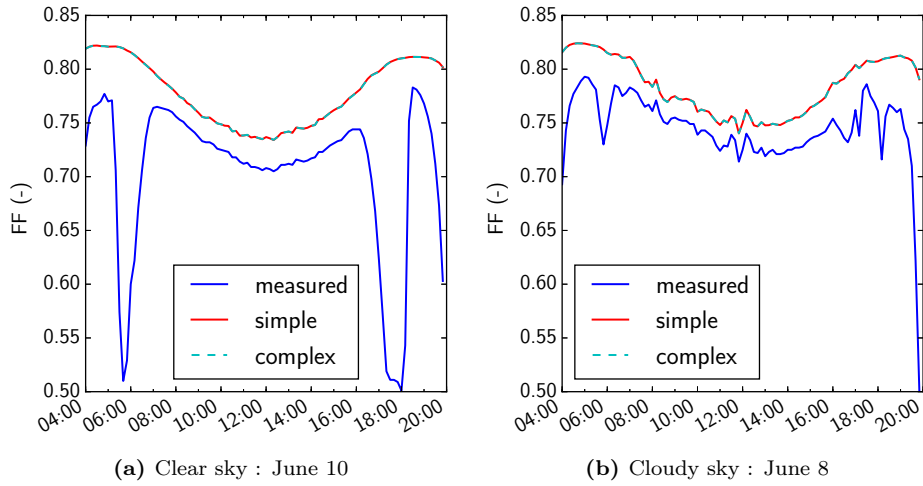


Figure 5.1.19: Simulated and measured FF of the module on a clear-sky and cloudy day

Table 5.1.7: Error in FF of the module for the two fill factor expressions.

	simple	complex
Mean error (-)	0,0343	0,0342
MRE (%)	4,86%	4,85%
RMSE (-)	0,0492	0,0491
STD (-)	0,0353	0,0353

The “complex” method is found to be slightly more accurate than the simple formulation of the fill factor (Table 5.1.7), which is in agreement with [Green \(1982\)](#), and is therefore chosen as default. The difference in errors between both approaches is negligible compared to the overall error. However, this overall error in FF is non-satisfying.

Two main hypothesis must be checked, namely:

1. the temperature dependence of the series resistance can be neglected;
2. the shunt resistance can be assumed infinite.

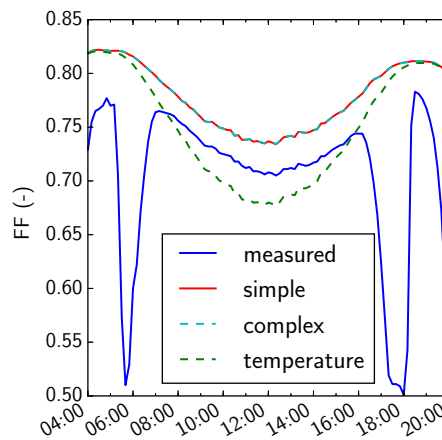


Figure 5.1.20: Simulated and measured FF on a clear-sky day (10 June 2017), including a method accounting for the temperature dependence of the series resistance.

[Sabry & Ghitas \(2007\)](#) studied the influence of temperature on the series resistance and the

model suggested for the one diode model is applied ² but did not allow to correct the error as shown in Figure 5.1.20: the new curve has a trend which corresponds less to the measured fill factor than those computed above. The temperature dependence of R_s therefore cannot explain the error in fill factor.

The issue may arise from the shunt resistance, however, the shunt resistance and the series resistance cannot be both computed thanks to the manufactured data but would require experimental measurements.

5.1.4.4 Operating power

The power is now assessed without the intermediate measurements of I_{SC} , V_{OC} and FF but by cascading down the simulated values as illustrated by Figure 5.1.21. In this approach and as reminded in Figure 5.1.13 the modelled POA is scaled to the measurements.

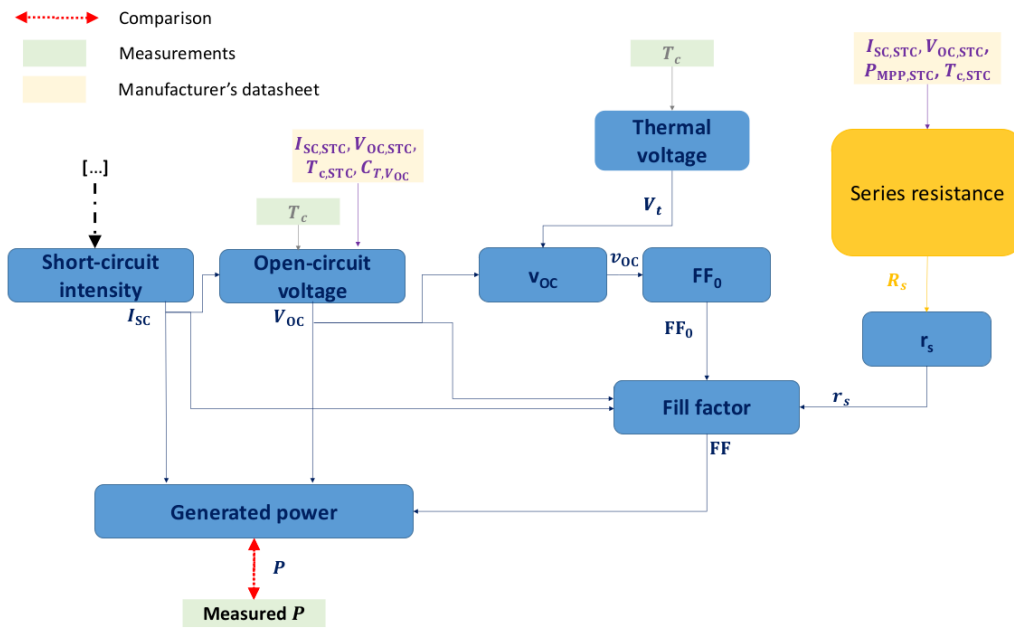


Figure 5.1.21: Methodology used to assess the accuracy of the power, with the I_{SC} modelled following Figure 5.1.13

Figure 5.1.22 presents the same clear and cloudy days as previously but in terms of simulated and measured power. The Table 5.1.8 summarizes the errors in module power over the month of June for POA irradiance above 200 W m^{-2} . The mean relative error is low (2.3%) and the mean absolute error is of 4.8 W (for a nominal power of 250 W) meaning that the power modelisation from POA irradiance and temperature is robust (Table 5.1.8).

Table 5.1.8: Error in P of the module by using the simulated I_{SC} , V_{OC} , FF. The nominal power of the panel is 250 W.

	Simulated
Mean error (W)	2,30
Mean relative error (%)	2,29
RMSE (W)	6,50
STD (W)	6,07

² $R_s(T_c) = \frac{0.025 \cdot T_c + 17.9}{100000}$, Sabry & Ghitas (2007)

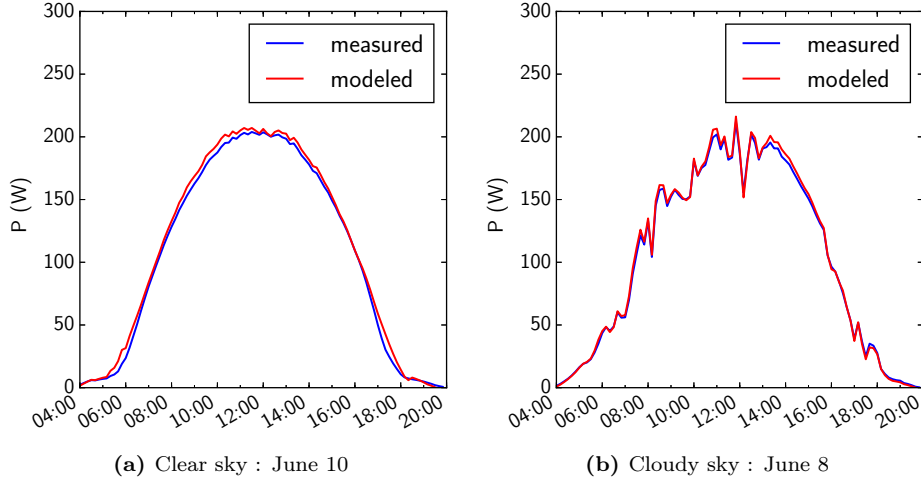


Figure 5.1.22: Simulated and measured P of the module on a clear-sky and cloudy day. The measured module temperature is considered and POA irradiance corrected by the measurements.

5.1.5 Evaluation of the overall code

5.1.5.1 With the measured temperature

In order to assess the errors due to modelling the irradiance from measurement on a horizontal surface, the simulated power is compared to the measurements when all steps are modelled except the cell temperature. The POA irradiance is therefore no longer corrected by the measured value, contrary to the previous sections.

Table 5.1.9: Error in I_{SC} , V_{OC} , FF and P of the module by using all simulated variables except the cell temperature. The nominal power of the panel is 250W.

	I_{SC}	V_{OC}	FF	P
MBE	-0,033 A	0,133 V	0,0350	4,8 W
MRE	-0,67 %	0,38 %	4,97 %	4,64%
RMSE	0,672 A	0,298 V	0,0501	18,5 W
STD	0,672 A	0,266 V	0,0358	17,9 W

Table 5.1.9 indicates the errors in terms of module power. The mean relative error is of 4.6% (compared to 2.6% when the POA irradiance is set to the measured value), meaning that the errors introduced by the transposition models are non negligible. As expected, the induced errors on the irradiance impacting the cell mainly influence the short-circuit current, with an MRE shifting from -2.9% to -0.7% (pointing out that the POA irradiance is globally overestimated as I_{SC} increases).

Figure 5.1.23 illustrates the performance of the model with the measured temperature for a clear-sky and cloudy day.

5.1.5.2 Influence of the temperature model

The PV model is now assessed considering all simulated values, including the cell temperature.

Table 5.1.10 indicates that the mean relative error is of 0.18% which is less than when the measured temperature was considered. Figure 5.1.24 illustrates this performance for a clear and a cloudy day. The open-circuit is mainly sensitive to the temperature, which is coherent with the errors computed : the open-circuit voltage is now underestimated on average by

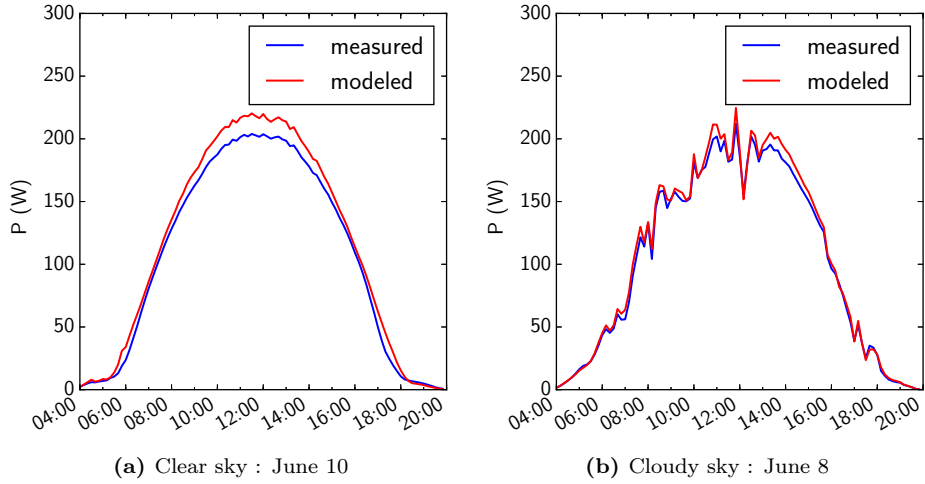


Figure 5.1.23: Simulated and measured P of the module on a clear-sky and cloudy day considering the measured module temperature. All variables are simulated and cascaded down except the cell temperature.

2.7% compared to previous mean relative errors closer to 0%, meaning that the simulated cell temperature is too high. In other terms, the temperature model adds errors into the model, but allows to counterbalance the errors due to the transposition model, thus improving the final result.

Table 5.1.10: Error in P of the module by using all simulated variables. The nominal power of the panel is 250W.

	I_{SC}	V_{OC}	FF	P
MBE	-0,022 A	-0,94 V	0,0306	-1,9 W
MRE	-0,48 %	-2,72 %	4,36 %	0,18 %
RMSE	0,677 A	1,15 V	0,0469	15,8 W
STD	0,676 A	0,66 V	0,0356	15,7 W

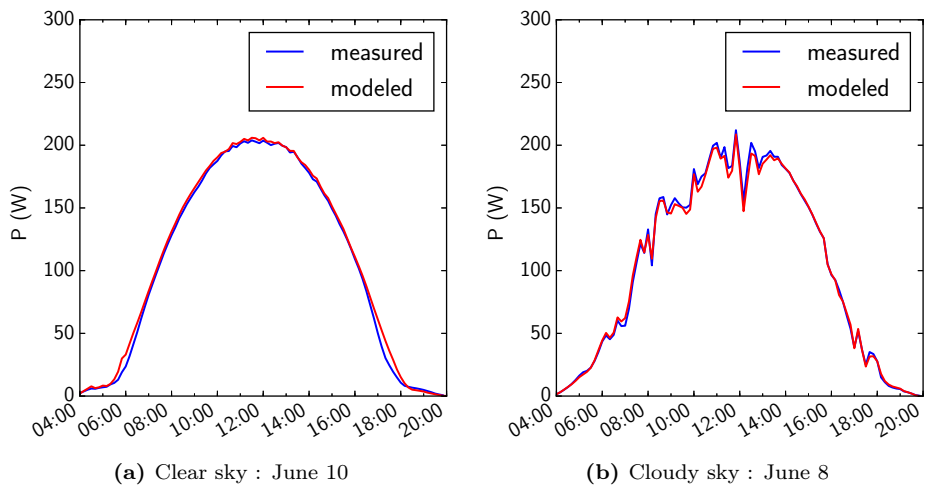


Figure 5.1.24: Simulated and measured P of the module on a clear-sky and cloudy day. All variables are simulated.

In the case of a better FF model, it would be beneficial to have a more accurate cell temperature. As the model has been evaluated and calibrated thanks to the measured module temperature, the PV model may be more accurate if the modelled module temperature is in-

put. The simple model is not altered as it does not distinguish cell and module temperature, but only the module temperature can be computed in the King model. Figure 5.1.25 illustrates the errors in module temperature and shows that the King module model allows to best simulate the measured module temperatures.

As a conclusion, with a better physical model, it may be more interesting to use the King module model as a temperature model.

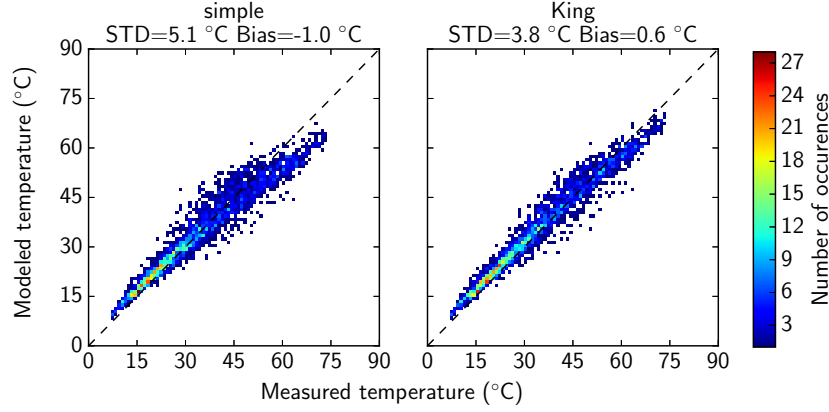


Figure 5.1.25: Modeled versus measured module temperature (FranceWatts monocrystalline module): comparison between the simple model and the King model (module temperature).

5.1.6 Summary of the default options

During the evaluation of the different subcomponents thanks to the measurements at the SIRTA in June 2017, the PV model has also been calibrated: the options to be applied by default have been selected and are summarised in Table 5.1.11.

Table 5.1.11: Options applied by default in the PV model

Process	Default option	Default required specifications
POA	ISOTROPIC 3D for SZA < 70° PEREZ otherwise	
Optical Losses	Reflection	n0=1.0, n1= 1.526
Module temperature	King	mount_type_King=5
Voc	I0	
FF	complex	

5.2 Validation over a winter month : example of December 2017

The default methods of the PV model have been chosen in Part 5 thanks to measurements on the SIRTA site in June 2017. It is therefore interesting to evaluate the developed model on an independent set of data. This part considers the performance of the model in December 2017.

Figure 5.2.1a shows the simulated power as a function of the measured power for $G_{\text{POA,meas}} > 200 \text{ W m}^{-2}$. This criteria allows to be consistent with the threshold chosen for the evaluation in Part 5. The MRE is evaluated as being 3.70 % and the MBE -0.77 W which means the model is less accurate in December than during June (whose errors are provided in Table 5.1.10).

This change in accuracy can notably arise from lower SZAs on average and lower temperatures in December than in June. The options by default are therefore not necessarily optimal

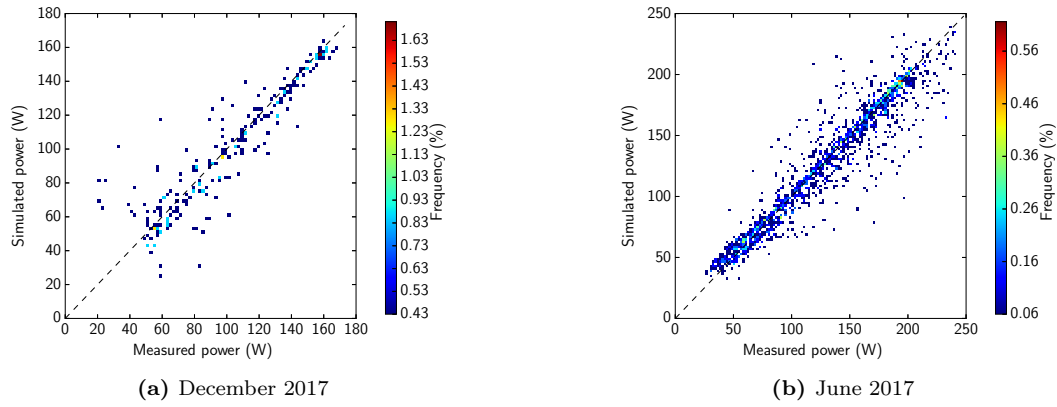


Figure 5.2.1: Density function of the modelled power as a function of the measured power

for December.

However, the criteria on the POA irradiance implies that only 218 data points out of 4321 in December are exploited, such that the analysis over several winter months would allow a better overview of the accuracy in winter.

PART 6

FURTHER INVESTIGATION OF THE SPECTRAL AND ANGULAR EFFECTS ON PV PERFORMANCE

The PV model has been validated and can now be applied to further understand the effects of the spectral and angular properties of radiation on the PV performance. First, the impact of clouds hinted at in Part 2.3 is further analysed by coupling ecRad with the PV model. Then, the difference in performance between a simple PV model neglecting spectral effects and the one developed in this project is assessed. Last, one of the specificities of this model resides in the use of spectral irradiances, whereas other models are based on broadband irradiances. The impact on the number of bands is therefore investigated.

6.1 Impact of clouds on PV performance

6.1.1 Influence of clouds on the radiation incident on a tilted surface

Clouds impact available radiation at the surface mainly through three physical phenomena :

1. Reflection, which is the primary effect and limits radiation transmission.
2. Absorption, which is wavelength selective (Figure 2.1.3).
3. Scattering, thus changing the orientation of radiation.

By increasing the reflection and absorption, clouds contribute to a drop in irradiance reaching the ground and consequently in PV power. However, the change in angular and spectral properties also result in a change of PV efficiency.

6.1.2 ecRad simulations coupled with the PV model

The influence of clouds on PV performance has been studied by coupling ecRad simulations with the PV model following the method illustrated in Figure 6.1.1: the atmosphere is set to the US Standard Atmosphere 1976 and variable atmospheric conditions are reached by adding a cloud with a thickness of 500 m whose optical thickness is controlled by its liquid water mixing ratio. The resulting radiation is then fed into the PV model. In this study, a monocrystalline panel (identical to the one on the SIRTAsite) is considered but inclined of 37° – the recommended inclination for maximum exposure. The cell temperature is set constant to the NOCT, such that only the irradiance can influence the performance of the PV panel.

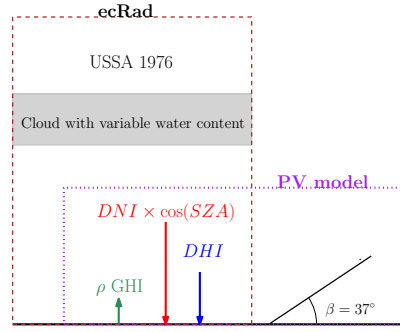


Figure 6.1.1: Simulation protocole

The efficiency of the PV module can be defined as the ratio of generated power to the plane-of-array irradiance. The change in efficiency with varying cloud optical thickness and SZA is given in Figure 6.1.2a. An overall increase can be observed with gains of up to 5.2% in efficiency, meaning that clouds lead to more efficient atmospheric conditions for PV performance, which is coherent with the observations made by *Jardine et al. (2001)* and *Nofuentes et al. (2014)*. This global increase in efficiency can be explained by the absorption of photons by clouds (liquid water, ice) for wavelengths above the gap wavelength – *i.e.* photons that cannot be absorbed by solar cells – as illustrated in Figure 2.1.3, thus increasing the irradiance within the wavelength domain the silicon cell is sensitive to, as shown in Figure 6.1.3a for $SZA = 0^\circ$.

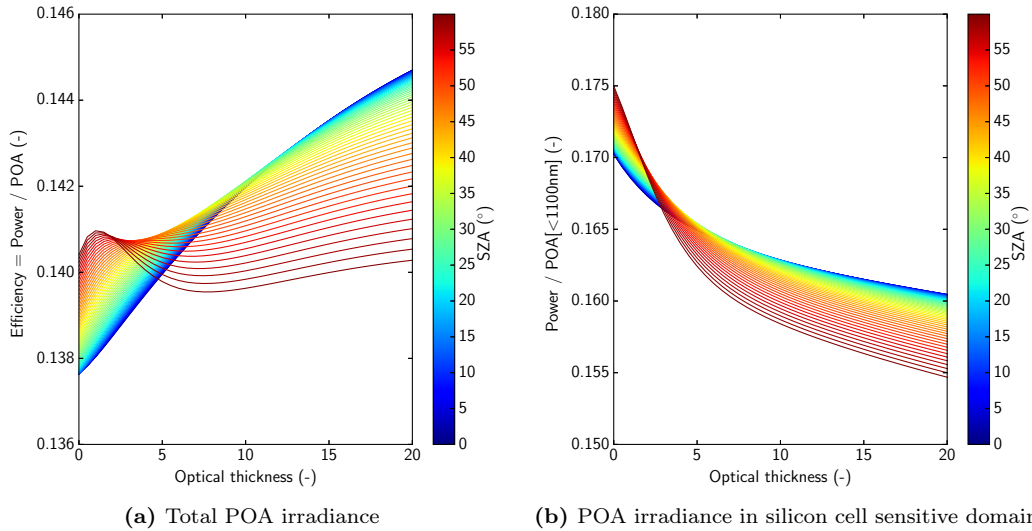


Figure 6.1.2: Efficiency of monocrystalline solar cell as a function of the cloud optical thickness and SZA.

When correcting the efficiency to only account for the POA irradiance in the wavelength domain which can be converted by the PV cell, the variation in efficiency is much simpler. As presented in Figure 6.1.2b, this alternative efficiency decreases with optical thickness for all SZA (Figure 6.1.2b), which is due to the shift of irradiance towards the less efficient blue domain with increasing optical thickness. The conversion from 6.1.2a to 6.1.2b is done by considering the fraction of effective POA irradiance, which depends on the cloud optical thickness (Figure 6.1.3a), but also on SZA (Figure 6.1.3b), which both explain the complex variation observed in Figure 6.1.2a.

The variation remaining with the alternative efficiency also underlines the change in the solar spectrum with SZA and τ and stresses the fact that there is not a simple relationship between incoming radiation and generated power.

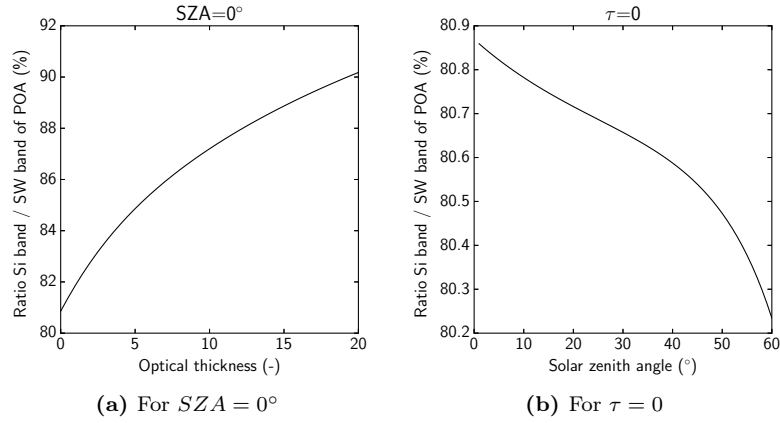


Figure 6.1.3: Variation in effective POA irradiance with optical thickness and solar zenith angle.

The following aims at understanding why there is an inversion in the order of efficiency with SZA between clear-sky and cloudy-sky conditions in Figure 6.1.2b.

In clear-sky conditions, the direct radiation is the main contributor to the POA irradiance, and its contribution increases with the SZA for the chosen inclination as confirmed by Figure 6.1.4. Yet, direct radiation is more efficient than the diffuse radiation which has a heavy distribution around the blue domain. Therefore, the spectrum for high SZA is richer in red than a lower SZA as illustrated in Figure 6.1.5 which generates more current thus resulting in a higher PV module efficiency.

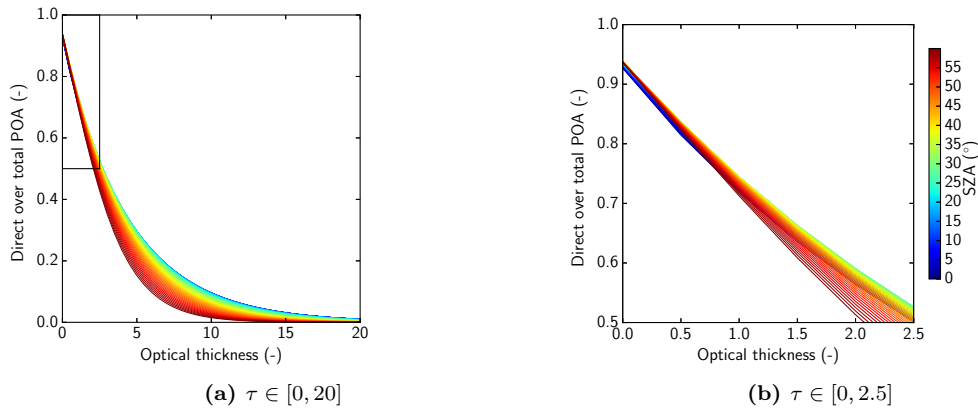


Figure 6.1.4: Contribution of the beam radiation in the overall POA irradiance.

In overcast conditions, the radiation on an inclined surface is mainly diffuse. Moreover, the diffuse component becomes “bluer” as the distance travelled in the atmosphere increases – *i.e.* with increasing SZA – thus explaining why the efficiency as a function of SZA is the opposite compared to clear sky conditions.

Therefore, the impact of clouds on radiation can be explained by two levels of spectral filtering. First, clouds tend to increase the efficiency of a PV module when considering the SW integrated irradiance as they filter out photons which do not have enough energy to be absorbed by PV cells. Second, due to the shift from NIR towards the blue domain, the effect is

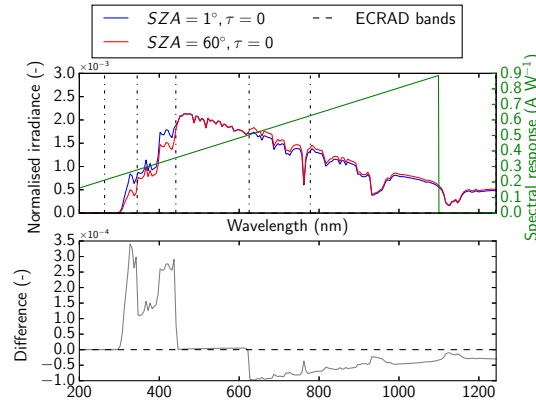


Figure 6.1.5: Normalised irradiance over 200–2500nm for $SZA = 1$ or 60° and $\tau = 0$

opposite when only the irradiance in the effective range for silicon cells is taken into account. Furthermore, the SZA also has an important impact on the efficiency of the solar cell.

6.1.3 Observed phenomena

Observations in June 2017 at the SIRTAs can also be analysed and confronted with the results obtained with the ecRad simulations.

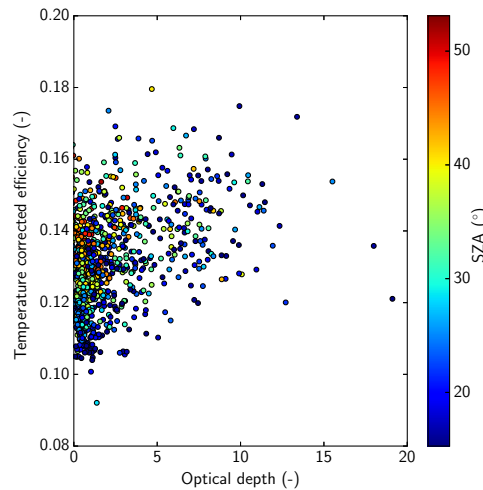


Figure 6.1.6: Measured efficiency as a function of the optical depth deduced from the measurements of June 2017. The efficiency is corrected to represent the equivalent efficiency at NOCT.

Figure 6.1.6 shows the efficiency of the monocrystalline silicon module installed at the SIRTAs in June as a function of the estimated optical depth when $G_{POA,meas} > 200 \text{ W m}^{-2}$. The efficiency is derived from the measured power and POA irradiance but is then corrected by the measured module temperature such that all efficiencies represent a module operating at the NOCT. This correction allows to cancel the effect of temperature on efficiency and obtain corrected measurements that can be compared to those in Figure 6.1.2a. However, the efficiency deduced from the measurements does not present the same trend as with ecRad as no global trend in SZA or τ can be distinguished. This can be expected as the ecRad simulations consider an identical atmosphere (USSA 1976) whereas the measurements correspond to different atmospheric conditions where varying physical quantities such as humidity and aerosol affect the incoming spectral and angular properties of the irradiance and thus the PV module efficiency.

Furthermore, the efficiencies obtained with ecRad are of the order of 14% which is coherent with the corrected measured values.

6.2 Influence of the spectral resolution of the irradiance input

The irradiance from measurements or atmospheric models is often provided integrated over the whole SW domain. Yet, the previous analysis on the influence of clouds on PV performance stresses the role of the spectral properties of the incoming irradiance. This paragraph aims at answering the question of whether this lesser level of knowledge of spectral properties has a crucial impact on the modeled power.

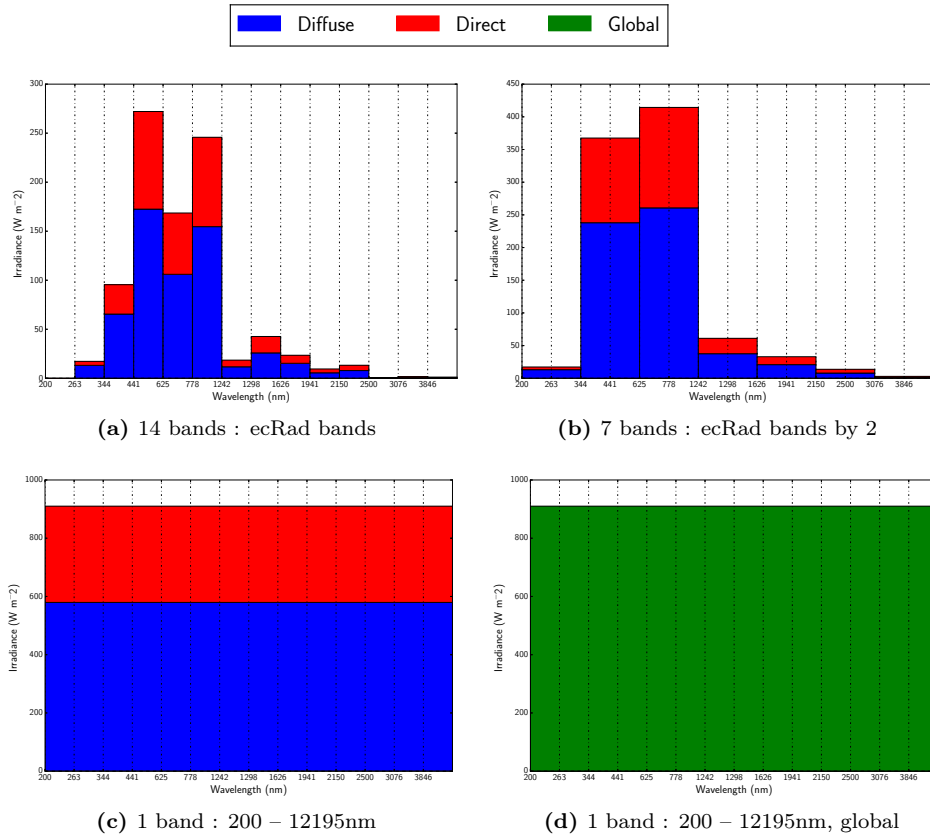


Figure 6.2.1: Illustration of the incoming irradiance integrated over each band for different levels of knowledge. The dotted vertical lines represent the delimitation of the fourteen ecRad bands. This illustration corresponds to the case $\tau = 0$ and $\text{SZA} = 30^\circ$.

In order to answer this question, different atmospheric conditions are simulated with the coupled ecRad/PV models following the same methodology as presented in Figure 6.1.1. The 14-band direct and diffuse irradiance outputs of ecRad are postprocessed to constitute three declined levels of knowledge, as illustrated in Figure 6.2.1: the direct and diffuse irradiance over the 14 SW bands of ecRad (Figure 6.2.1a) are first integrated over every 2 consecutive bands resulting in a 7-band input (Figure 6.2.1b) and then over all the bands leading to a 1-band input (Figure 6.2.1c) for the PV model. Then, in order to further worsen the knowledge on the incoming irradiance and to also briefly investigate the importance of the angular properties, a fourth input consists in considering the global irradiance in the SW (Figure 6.2.1d) by summing the direct and diffuse components of the 1-band irradiance. The redecomposition between direct and diffuse irradiance is then computed following *Erbs et al. (1982)*. Spectralisation is

then applied to these three different spectral resolution inputs.

The power modeled with the coupled ecRad–PV model considering the ecRad 14-band output is used as a reference. The relative error for all $\{SZA, \tau\}$ combinations (identical to those in Part 6.1 hereinabove) and all three degraded inputs can then be computed, as represented in Figure 6.2.2.

First, when the decomposition between direct and diffuse components is modelled, the relative errors present no general trend over SZA and τ and range from 7.3% to -9.9%. This biggest range of relative errors among all three levels of knowledge as well as the non-monotonous variability with atmospheric conditions point out that the GHI is not a sufficient parameter for PV modelling.

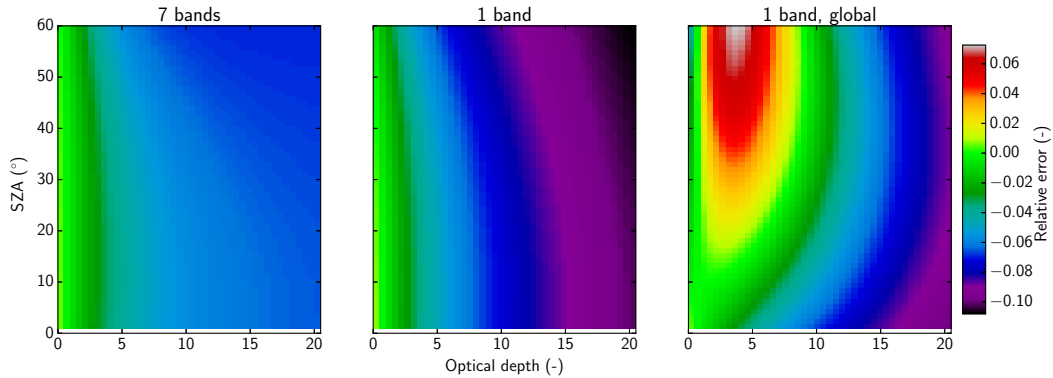


Figure 6.2.2: Relative error in modelled power with varying SZA and τ for the 7-band, 1-band and 1-band global inputs

When considering the two other levels of knowledge, Figure 6.2.2 shows a clear deterioration in accuracy when the number of bands is reduced and when the cloud optical depth increases. This behaviour with τ is expected since clouds induce spectral filtering whose effect grows with optical depth with a shift of the normalised spectrum towards the blue domain. Yet, the reference MODTRAN spectra used for spectralisation (see Part D.2.1) have been computed under clear-sky conditions and only aim at shaping the irradiance over the given bands.

Consequently, when only one band is provided, the resulting spectral irradiance corresponds to clear-sky conditions, such that the spectrum shift and the growing fraction of POA irradiance which can be absorbed by the PV cell are not accounted for, thus leading to underestimated power, which is coherent with the negative relative errors simulated with the 1-band input (Figure 6.2.2). As the POA irradiance in the SW is accurate, one can expect the trend of the relative error to follow that of the difference of efficiency between clear-sky (for the 1-band model) and the modeled τ (for ecRad) given in Figure 6.1.2a, which would lead to a non-monotonous variability, contrarily to what is observed. This is due to the difference in the modeled clear-sky conditions between MODTRAN and ecRad as the USSA is a complex atmosphere that has not been as accurately modeled in ecRad (*e.g.* the aerosols have been neglected in ecRad). Figure 6.2.3 shows the spectral distribution of MODTRAN and ecRad-simulated direct and diffuse irradiance under USSA for $\tau = 0$ and $SZA = 30^\circ$. In the case of MODTRAN, the spectrum has been integrated over all fourteen SW ecRad bands. The spectrum is richer in blue with ecRad than MODTRAN under clear-sky conditions (probably because aerosols absorption is neglected in ecRad) meaning that the simulated conditions are

not exactly identical in MODTRAN and ecRad and also explains positive relative errors for $\tau = 0$ with the 1-band model. As τ increases, the change in spectral distribution with ecRad coupled with the use of reference spectra from MODTRAN complexifies the understanding of the simplified trend in Figure 6.2.2 compared to Figure 6.1.2a.

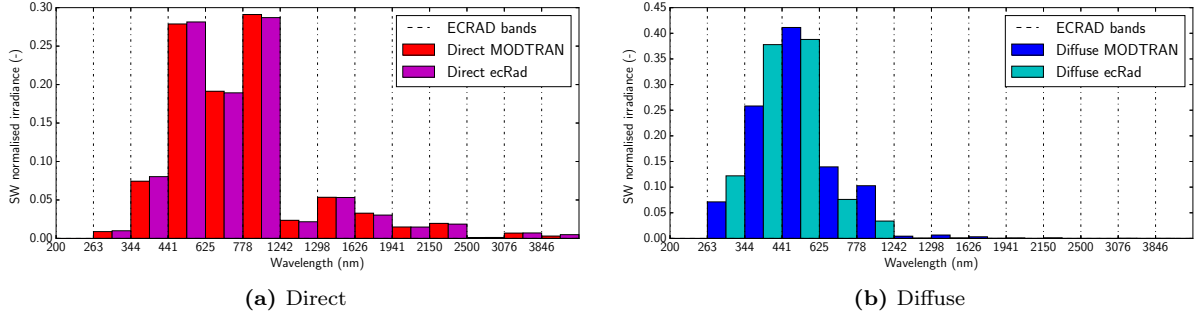


Figure 6.2.3: Direct and diffuse irradiance normalised over the SW domain from MODTRAN and ecRad for the clear-sky USSA and SZA = 30 °C

In the case of the 7-band irradiance, the total POA in the band absorbed by the solar cell is expected to be well modelled such that one can refer to the efficiency as a function of the effective POA irradiance (Figure 6.1.2b). However, thanks to the seven bands, the modeled irradiance no longer represents clear-sky conditions such that the efficiency point with the 7-band model on the efficiency curve is not clearly defined. For $\tau = 0$, the relative error is positive due to the difference in spectrum shape between MODTRAN and ecRad in clear-sky conditions explained here above in the case of the 1-band model. As τ increases, the relative error decreases and becomes negative: the power is underestimated. This must originate from the fact that when integrating over two bands, two consecutive bands which may be respectively increasing and decreasing in value, can therefore, once summed, reduce or even cancel any change in the spectrum shape. In other terms, with a reduced number of bands, variations within each band between two different states can compensate each other and possibly result in an identical band irradiance.

The 7-band model is therefore more precise (up to -7.1% error) than the 1-band model (up to -10.8% error) which is coherent with the fact that there is a loss of information. Furthermore, the accuracy presents a slight decrease with SZA though the errors are limited thanks to the use of SZA-interpolated MODTRAN spectra as reference. This slight increase in error with SZA is justifiable because an increased SZA corresponds to a longer path through the atmosphere and is therefore subject to more absorption and dispersion than a lower SZA. Therefore, higher SZAs amplify the spectral filtering and are expected to be less easy to accurately model than lower SZA which are closer to the reference clear-sky spectra.

Therefore, this small analysis proves that the level of knowledge of the spectral distribution has a clear influence on the modeled power with up to 10% difference in modeled power observed for inputs with less bands.

6.3 Comparison with a simple PV model

The impact of clouds on PV performance (Part 6.1) as well as the study of the number of bands (Part 6.2) have highlighted the importance of knowing the spectral properties of the incoming

irradiance.

Given this fact, it is worthy to compare the performance of the developed PV model to a simple PV model often applied – where the efficiency of the PV module is only corrected by temperature and therefore does not account for changes in spectral distribution compared to STC – like in *Jerez et al. (2015)* :

$$P = P_R \times P_{\text{STC}} \times \frac{G}{G_{\text{STC}}} \quad (6.3.1)$$

with G (resp. G_{STC}) the incoming irradiance (resp. under STC) and P_R the performance ratio defined by:

$$P_R = 1 + \gamma(T_c - T_{c,\text{STC}}) \quad (6.3.2)$$

where $\gamma = C_{T,P_{\text{MPP}}}$ is the power thermal coefficient, the performance ratio thus representing the loss (or gain) in efficiency induced by the cell temperature compared to STC.

This common model is applied to the atmospheric conditions measured by the SIRTAs in June and December 2017 and compared to the developed PV model.

In order to only account for the difference in formulation of the power as a function of POA irradiance and temperature of both models, the POA irradiance integrated over the SW domain and the cell temperature as computed by the developed PV model are applied in 6.3.1 such that the two variables are identical in both cases.

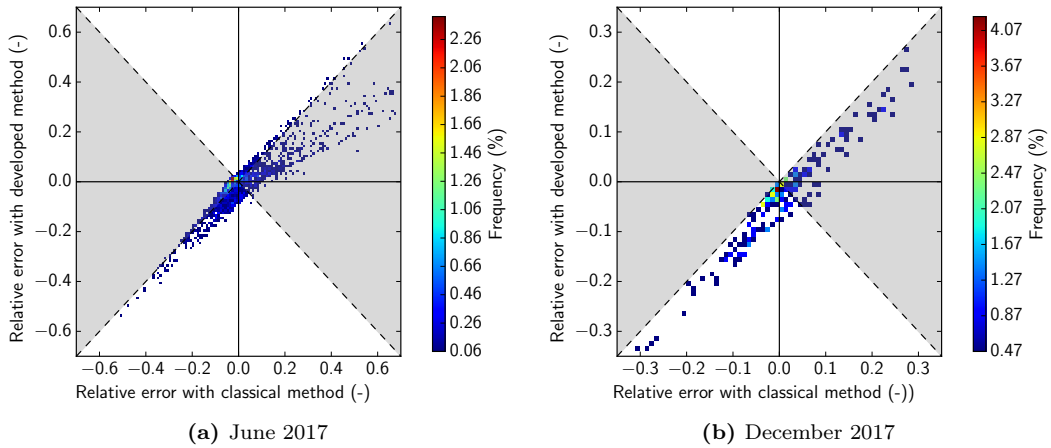


Figure 6.3.1: Relative error in modelled power with the newly developed versus a classical model. The grey zone represents the region where the developed models performs better.

The relative error compared to the measured power is calculated for both models and represented in Figure 6.3.1 for June and December 2017. In June, the PV model developed in this project performs overall better than the simple model (MRE in module power of 0.18 % versus 3.39 % and RMSE¹ of 15.8 W versus 16.4 W for $G_{\text{POA}} < 200 \text{ W m}^{-2}$). Both models tend to behave similarly in June except for the region of positive MRE below the first bisector where the relative errors with the classical model are approximately doubled. A further study is required to understand the origin of this difference.

In December (Figure 6.3.2b), the developed model leads to lower relative errors than the simple method (all values are below the first bisector), and overall the developed model is more

¹As a reminder, the nominal power of the module is 250W.

accurate with a MRE of 3.7 % against 8.4 % for the classical model and a RMSE of 14.9 W versus 15.7 W for $G_{\text{POA}} < 200 \text{ W m}^{-2}$. However, the limited number of data points verifying $G_{\text{POA}} < 200 \text{ W m}^{-2}$ must be kept in mind before generalising this observation.

Though a thorough analysis is necessary to accurately understand the origin of differences observed between both models, several conditions where the developed code is expected to perform better can be pointed out

First, the simple model does not account for optical losses which are important when the sun is low in the sky (high SZA) which induces overestimated power after sunrise and before sunset. This confirmed in the observations as illustrated in Figure 6.3.2a for 10 June 2017.

Second, a model which does not account for the spectral distribution of irradiance is not expected to be accurate when atmospheric conditions are drastically different than STC (as seen in Part 6.1 and Part 6.2). The irradiance between 5 and 8 December is particularly low for the month (mean POA irradiance of 73.74 W m^{-2} over the three days against a monthly average of 97.62 W m^{-2} during daytime) and is probably due to denser clouds as the ratio of the irradiance measured by the spectrometre to that of the pyranometre is high (on average 0.87). Figure 6.3.2b illustrates the simulated and measured power between 5 and 8 December where the atmospheric conditions are particularly different to the clear-sky conditions in STC. As expected, the model neglecting spectral changes does not reproduce accurately the power under such conditions on the contrary to the developed model.

Furthermore, monocrystalline silicon solar cells are known to be less sensitive to spectral changes than other solar cells with a larger band gap (*Nofuentes et al. 2014*, *Dirnberger et al. 2015*) such as CdTe and a-Si cells. This new model is therefore expected to be even more relevant for these technologies. Nevertheless, this comparison with the silicon cell known to be only slightly sensitive to spectral changes already legitimizes the newly developed PV model.

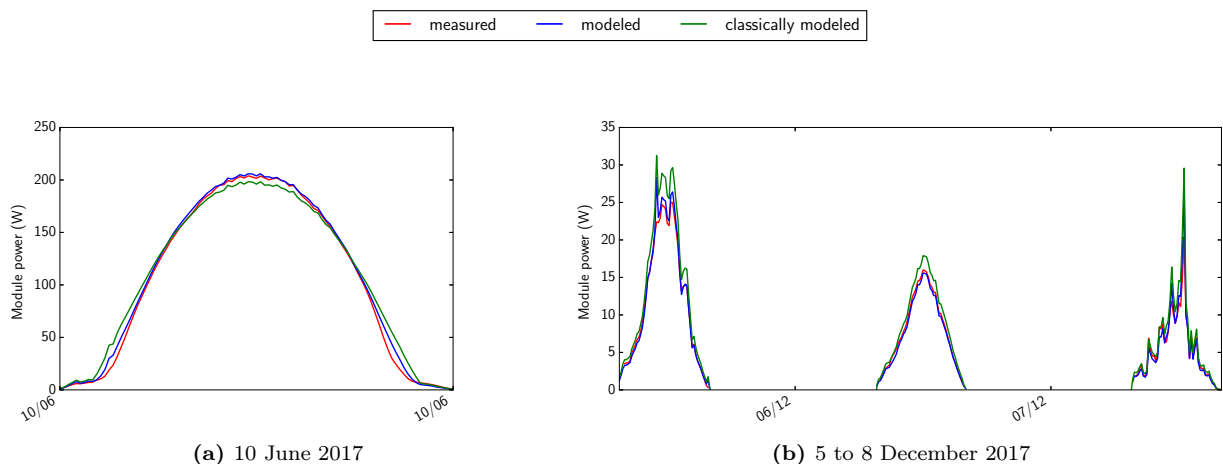


Figure 6.3.2: Measured and modelled module power with newly developed or classically used PV model

THE COUPLED MESO-NH – PV MODEL

Meso-NH simulations have been performed to simulate the atmospheric conditions over the SIRTA site during the month of June 2017. The coupled MesoNH – PV model for the monocrystalline silicon module on the SIRTA site is then assessed, following which the errors in the atmospheric modelling are analysed. Eventually, various suggestions which could improve the accuracy of the coupled model are discussed.

7.1 Method

In order to couple Meso-NH and the PV model, Meso-NH simulations must be performed, the variables of interest retrieved from the simulated atmosphere and finally introduced into the PV model.

7.1.1 The grid – PREP_PGD step in MESO_NH

The grid used in Meso-NH is centred on the SIRTA experimental site following the coordinates provided in Table 7.1.1. The resolution is set to $\Delta x = \Delta y = 1.3$ km and the number of nodes is fixed to 80 in both x and y directions ($n_x = n_y = 80$), thus creating a grid extending 104 km in both directions. The vertical discretization follows *Gal-Chen & Somerville (1975)* which is the method applied by default in Meso-NH and the number of vertical layers is set to $n_z = 64$.

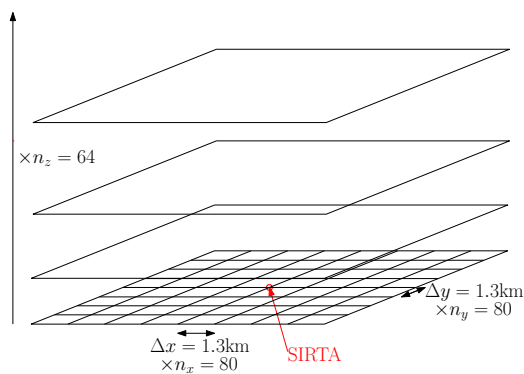


Table 7.1.1: SIRTA site location

Latitude	Longitude
48.718°	2.207°

Figure 7.1.1: Grid setup for Meso-NH simulations

The simulations consist in real case studies, with orography taken from Shuttle Radar Topography Mission (SRTM, resolution of 30 Arc-Seconds, equivalent to 250 meters) and land cover from ECOCLIMAP v2.0 (1 km resolution).

7.1.2 Initial and boundary conditions – PRE_REAL_CASE step in MESO_NH

The entire month of June is simulated in Meso-NH by independently launching each day from 00:00 to 24:00. The choice of starting each simulation at 00:00 enables the part of the day which is interesting for PV forecasting, *i.e.* during daytime, not to be affected by the initial setup of the simulation.

The initial conditions are provided by the AROME analysis at 00:00 of the desired day, and the simulation is forced at the lateral boundaries every 3 hours thanks to the AROME analyses. AROME analyses consist in the correction of AROME forecasts by observations such that they are assumed to be an accurate representation of the real atmospheric conditions at a given time. AROME analyses are provided on AROME’s 1.3km grid, thus justifying this choice of resolution for the Meso-NH grid. The choice of forcing the Meso-NH simulations with AROME analyses is justified by the will to first assess Meso-NH (and the coupled Meso-NH–PV model hereafter) on its capacity to correctly model the present situation rather than its “forecasting” abilities.

7.1.3 Meso-NH simulation – MESO_NH step in MESO_NH

Meso-NH simulations are launched with a time step of 30 seconds though the variables of interest are output every minute thanks to the use of the ground station and profiler tools of Meso-NH. These latter are applied to the location of the SIRTA site, thus limiting the amount of data to be saved. The ground station is set to save, among other variables:

- the air temperature at 2 m,
- the zonal and meridian wind speed at 10m,
- the spectral direct and diffuse irradiance at ground-level,
- the ground direct and diffuse spectral albedo,
- the solar zenith and azimuth angle,

whereas the profiler gives access to variables such as the vertical profile of:

- the cloud fraction,
- the liquid water content.

Apart from the air temperature and wind speed for the station and the liquid water content for the profiler, these variables are not programmed to be saved by default in Meso-NH but was enabled by changing the script accordingly.

In practise, the wind speed and air temperature should be provided to the PV model at the level of the PV panels. As the air temperature provided by the station is provided at 2 m which seems a reasonable approximation, the wind speed must be converted from 10 m to 2 m. This is achieved by applying the commonly used logarithmic wind speed profile ([Manwell et al. 2010](#), p.46):

$$u(z) = \frac{u_*}{\kappa} \ln \left(\frac{z-d}{z_0} \right) \quad (7.1.1)$$

with u the wind speed, u_* the friction velocity, $\kappa \approx 0.41$ the Von Karman constant, d the zero plane displacement and z_0 the surface rugosity.

The surface rugosity for the SIRTA site is retrieved from Meso-NH on 15 June 2018 at 00:00 thus corresponding to the middle of the simulated period and equals to $z_{0,SIRTA} = 0.694$ m. In the following, the rugosity is assumed constant, which seems acceptable given the simulation is limited to the month of June.

The zero plane displacement corresponds the 2/3 or 3/4 of the mean obstacle height in the neighbourhood. Without any further information, a displacement of $d = 0$ m is assumed. Finally, one can deduce the wind speed at 2m thanks to:

$$u(z = 2m) = u(z = 10m) \times \frac{\ln\left(\frac{z=2m}{z_{0,SIRTA}}\right)}{\ln\left(\frac{z=10m}{z_{0,SIRTA}}\right)} \quad (7.1.2)$$

7.1.4 Coupling method

A script to read the air temperature at 2m, the wind speed at 10m, the spectral irradiance at ground-level, the ground direct and diffuse spectral albedo, the solar zenith and azimuth angle from the ground-station output file and to compute the wind speed at 2m following (7.1.2) is added into the atmospheric input package (MY_ATM) for the PV model. This script also averages the variables over 10-minute windows so that the inputs' (and power outputs') time resolution correspond to those of the measurements. The six spectral bands of Meso-NH are specified in the namelist (NAMELIST) whereas all options are set to default. Finally the module package contains the specificities of the FranceWatts monocrystalline silicon panel (MY_MODULE). Eventually, the PV code can be launched by executing the MAIN script, outputting the power at every timestep provided in the atmospheric input.

7.2 Accuracy of the coupled model

The coupled model results in a MRE of 13.8% and a RMSE of 36.6 W. Figure 7.2.1 shows the simulated module power as a function of the simulated one and indicates with the high density of points around the first bisector that the coupled model often provides satisfactory results. However, the important number of points above this bisector also highlights that the coupled model often leads to power overestimation, which must originate from inaccuracies in the atmospheric simulations as the PV model resulted in a MRE of 0.2% when provided with the observed conditions over the same period of simulation (Part 5).

Figure 7.2.2 shows the simulated and measured power over the period of 10 to 20 June 2017, where the performance of the coupled model over clear-sky days is satisfactory but the strong variability of power certainly due to moving clouds during cloudy-sky days is not reproduced. Over this period, Meso-NH therefore does not seem to reproduce the clouds correctly.

However, on other days, like over the period of 2–4 June illustrated in Figure 7.2.3, the coupled model does reproduce a variable power over the day, though this variability can be of the wrong strength (June 2nd), wrongly timed (June 3rd), or lack in variability (June 4th). The latter could possibly be explained by the resolution of the grid (1.3km) which prevents from correctly simulating small moving clouds as these are subgrid, and are therefore modelled by a cloud of lower optical thickness but stagnating over the cell for a longer period.

The performance of the coupled model is therefore expected to be highly dependent on the capacity of accurately reproducing the cloudy-sky conditions with Meso-NH. Two variables are therefore of high interest: the cloud optical thickness and the total cloud fraction. The cloud

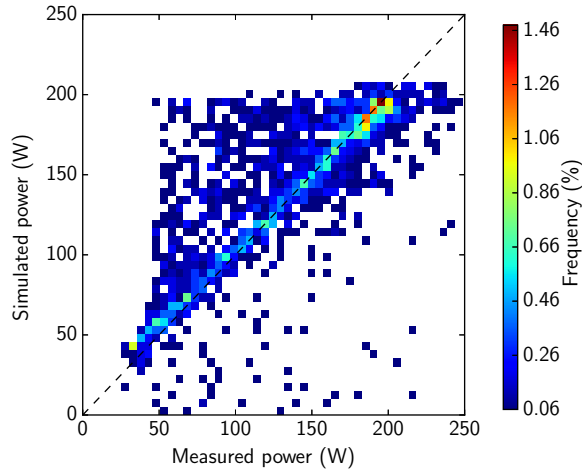


Figure 7.2.1: Modeled (Meso-NH + PV) versus measured power in June at the SIRTa

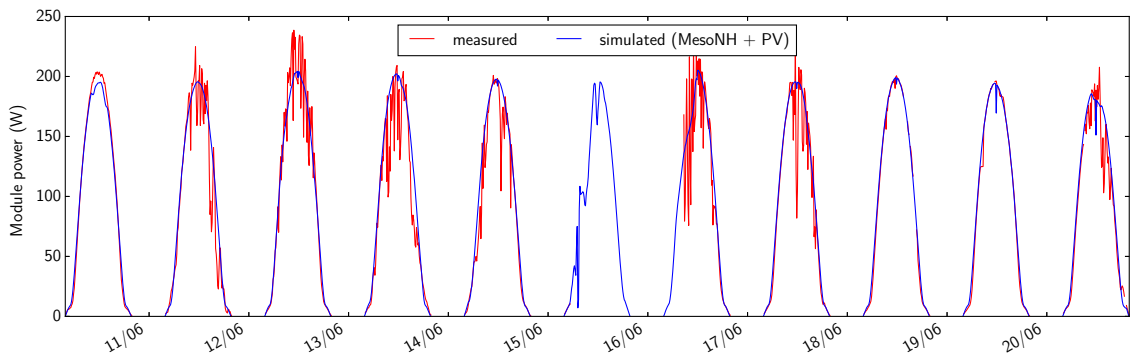


Figure 7.2.2: Measured and modeled by the coupled MesoNH-PV model from 10 to 20 June at the SIRTa

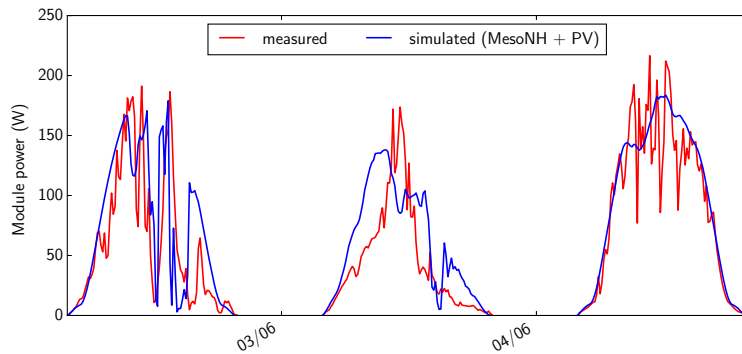


Figure 7.2.3: Measured and modeled power with the coupled MesoNH-PV model for June 2 and 3 at the SIRTa

optical thickness is computed as presented in Part 3.2. As previously explained, this optical thickness should be seen as an estimate rather than the exact representation of the physical properties of the cloud. The total cloud fraction must be computed from the vertical profile of cloud fraction available thanks to the profiler. Such computation is required by radiative transfer model such as ecRad, where three different hypothesis concerning cloud overlap can be applied, namely exponential-random, maximum-random and exponential-exponential (*Hogan & Bozzo 2016*). The same subroutine as developed in ecRad is therefore used to compute the total cloud fraction, using the maximum-random model which is the hypothesis applied in Meso-NH.

The relative error in simulated power as a function of the computed total cloud fraction is given in Figure 7.2.4a which indicates a frequent relative error around 0 when no clouds are modelled (cloud fraction of 0) thus corresponding to a correct simulation of clear-sky conditions by Meso-NH. On the other hand, there is a wide range of relative errors for small cloud fractions which correspond to wrongly-simulated clear-sky conditions. As the modelled total cloud fraction increases, the relative error can become highly positive or negative, hinting at the fact that the cloud fractions simulated by Meso-NH are probably either overestimated (negative relative errors) or underestimated (positive values).

However, the irradiance reaching the ground when the sky is overcast also depends on the cloud optical thickness. Figure 7.2.4b shows a high density of optical thicknesses under the value of 2 with a high dispersion in power relative errors. These relative errors are especially positive thus hinting at an overestimation in irradiance at ground-level which may mean that the optical thicknesses modelled by Meso-NH is often underestimated and stuck under the value of 2.

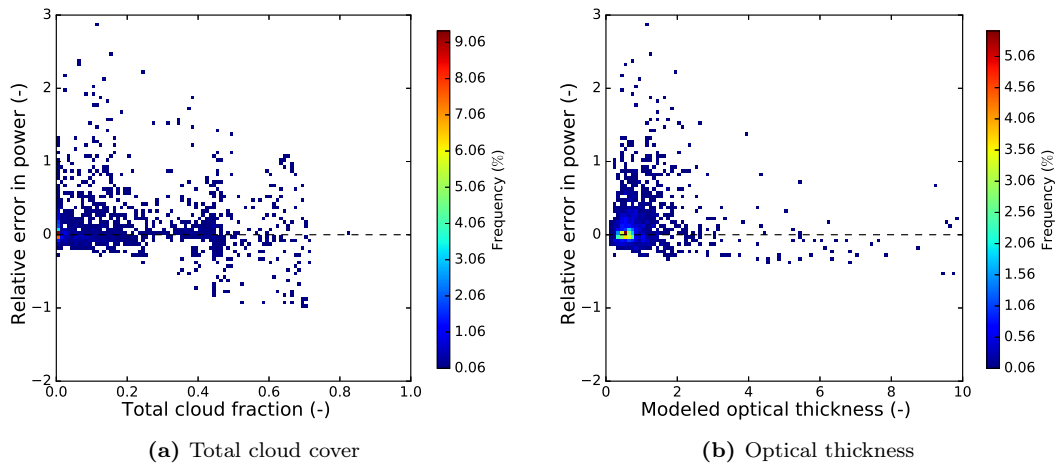


Figure 7.2.4: Relative error in power as a function of the modelled total cloud cover and optical thickness from Meso-NH simulations.

7.3 Sources of error in Meso-NH simulations

In order to better understand the performance of the coupled Meso-NH – PV model, the atmospheric variables simulated by Meso-NH are compared to the observations. This comparison is intentionally only qualitative as it aims at understanding the source of errors in the modelisation and the ways to improve the simulated atmospheric conditions.

Clear-sky conditions are distinguished from cloudy skies, not only because Meso-NH is expected to perform better in clear-sky conditions, but also because they can both bring forward different sources of error.

Indeed, the irradiance reaching the ground are mainly influenced by clouds, aerosols and gases in the atmosphere. Therefore, if clear-sky conditions will indicate whether the quantity of aerosols and gases (ozone, carbon dioxide, etc.) which follow present climatologies in Meso-NH are representative of the actual conditions, irradiance under overcast conditions will be mainly sensitive to the properties of the clouds, like the cloud cover, the optical thickness, the cloud optical properties, *etc.*

In all cases, the variables are compared for $G_{\text{POA,meas}} > 200 \text{ W m}^{-2}$ which correspond to the periods where no low-irradiance effects of PV panels are expected and also allow to filter out values overnight which could bias the results. Furthermore, the clear-sky conditions are assumed met when the cloud optical thickness computed from both the Meso-NH simulated and observed variables are below 1.

7.3.1 Clear-sky conditions

The MRE and RMSE in modelled power under clear-sky conditions (Figure 7.3.1a) are equal to 1.48% and 11.65 W thus highlighting the good performance of Meso-NH in the absence of clouds. Figure 7.3.1b indicates that the global irradiance on a horizontal surface is on average well modelled though a slight negative bias can be observed. The direct irradiance (Figure 7.3.1c) presents those same characteristics except for some overestimated points, whereas the diffuse irradiance (Figure 7.3.1d) seems to present a saturation level leading to a quasi-systematic underestimation.

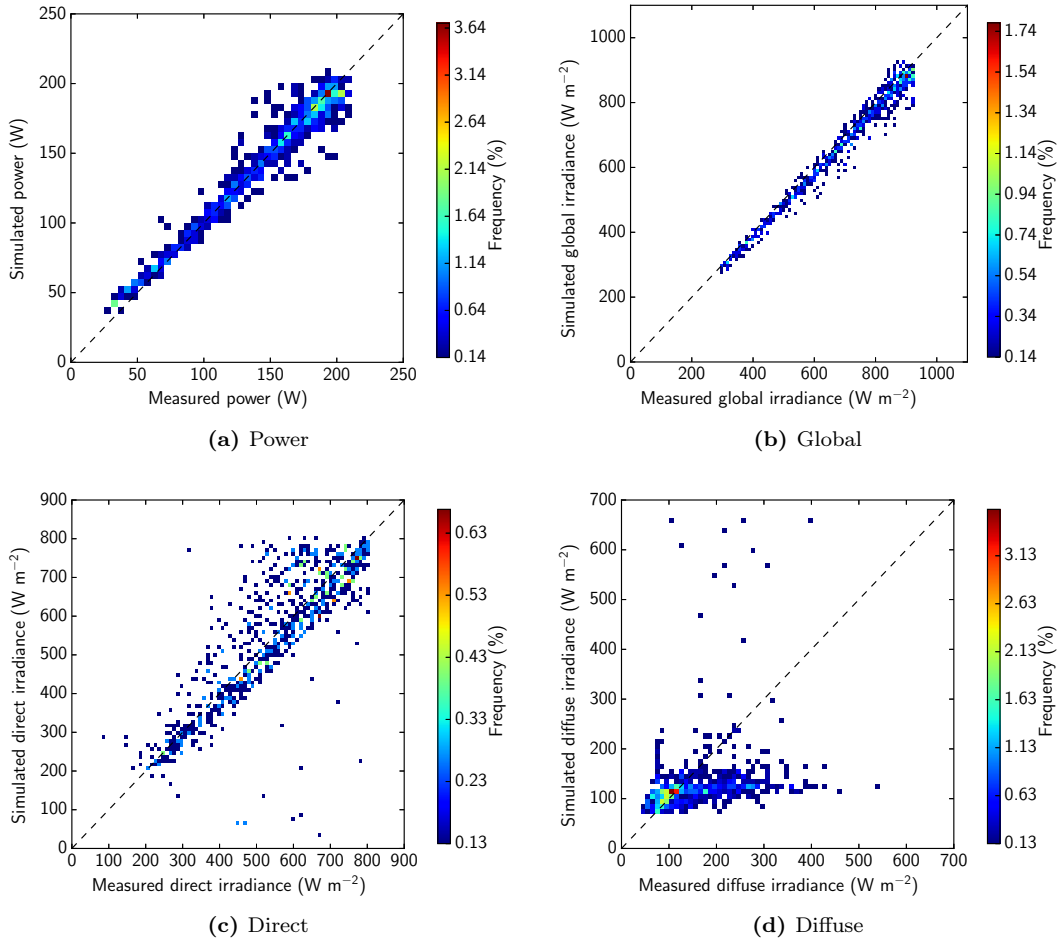


Figure 7.3.1: Modeled (Meso-NH + PV) versus measured power and irradiance under clear-sky conditions in June at the SIRTa. Each square has a resolution of 5 W for the power and 10 W m^{-2} for the irradiances

The analysis of spectral irradiances can provide further information concerning the cause of this underestimation trend. The spectrometre installed at the SIRTa only provides measurements over the 350–1050nm range meaning that only the 440–690nm band out of all six SW bands of Meso-NH can directly be compared. So as to provide a more thorough comparison, the spectralised GHI from the PV model is used and compared to the measurements over all

100nm-bands within the instrument’s range. The results given in Figure 7.3.2 indicate that the simulated spectral irradiance is clearly underestimated over 450–850nm which is consistent with a too high content of ozone according to its absorption bands (Figure 2.1.2) or aerosols which limit the irradiance reaching the ground by backward-scattering and absorbing radiation. However, further investigation is required to determine which is the real cause of this underestimation of irradiance. Also, the measurements of total ozone column and aerosols in the SARTA dataset turned out not to be complete enough to directly compare them to the values used in Meso-NH. Being able to retrieve such observations would allow to better identify how to improve the accuracy of Meso-NH at the SARTA under clear-sky conditions.

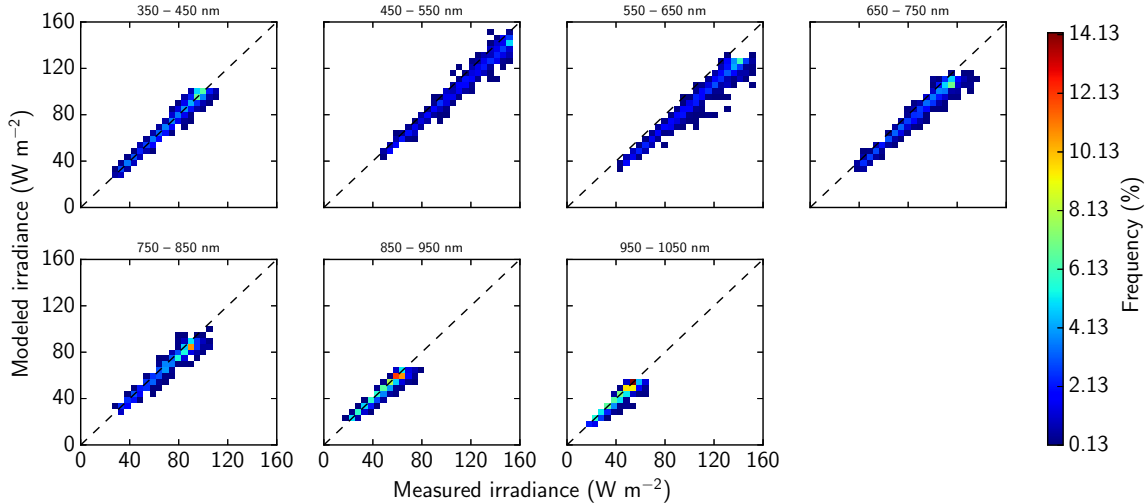


Figure 7.3.2: Modeled (Meso-NH + PV) versus measured spectral irradiance under clear-sky conditions in June at the SARTA, with a resolution of 5 W m^{-2}

7.3.2 All conditions

In the following, all sky conditions are analysed, therefore, on top of the clear-sky cases rightly identified by Meso-NH, all wrongly identified clear- or cloudy-sky conditions by Meso-NH and correctly identified cloudy conditions are taken into account.

The simulated global and direct irradiances compared to the measured ones (Figure 7.3.3a and Figure 7.3.3b) shows a high density around the first bisector corresponding mainly to the clear sky cases. The important underestimation in diffuse irradiance under clear-sky is also visible Figure 7.3.3c.

In overcast conditions, the global and direct irradiances are mainly overpredicted, thus explaining the global overestimation of the modeled power mentioned in Part 7.2 and also consistent with an underestimation of clouds. On the other hand, the cases where the simulated direct irradiance is wrongly estimated as close to zero (Figure 7.3.3b) correspond to events wrongly simulated as cloudy-sky by Meso-NH.

The diffuse irradiance is more intricate to analyse than direct irradiance as clouds both scatter and absorb which have opposite impacts on diffuse irradiance. Therefore, if the fraction of diffuse irradiance constantly grows with optical depth, its value evolves non-monotonously: as the cloud optical thickness increases, the scattering effect is first dominant with a growth in diffuse irradiance until the absorption counterbalances the scattering effect which then dominates: in a second phase, the diffuse irradiance decreases (Figure 2.3.3). In other terms, the

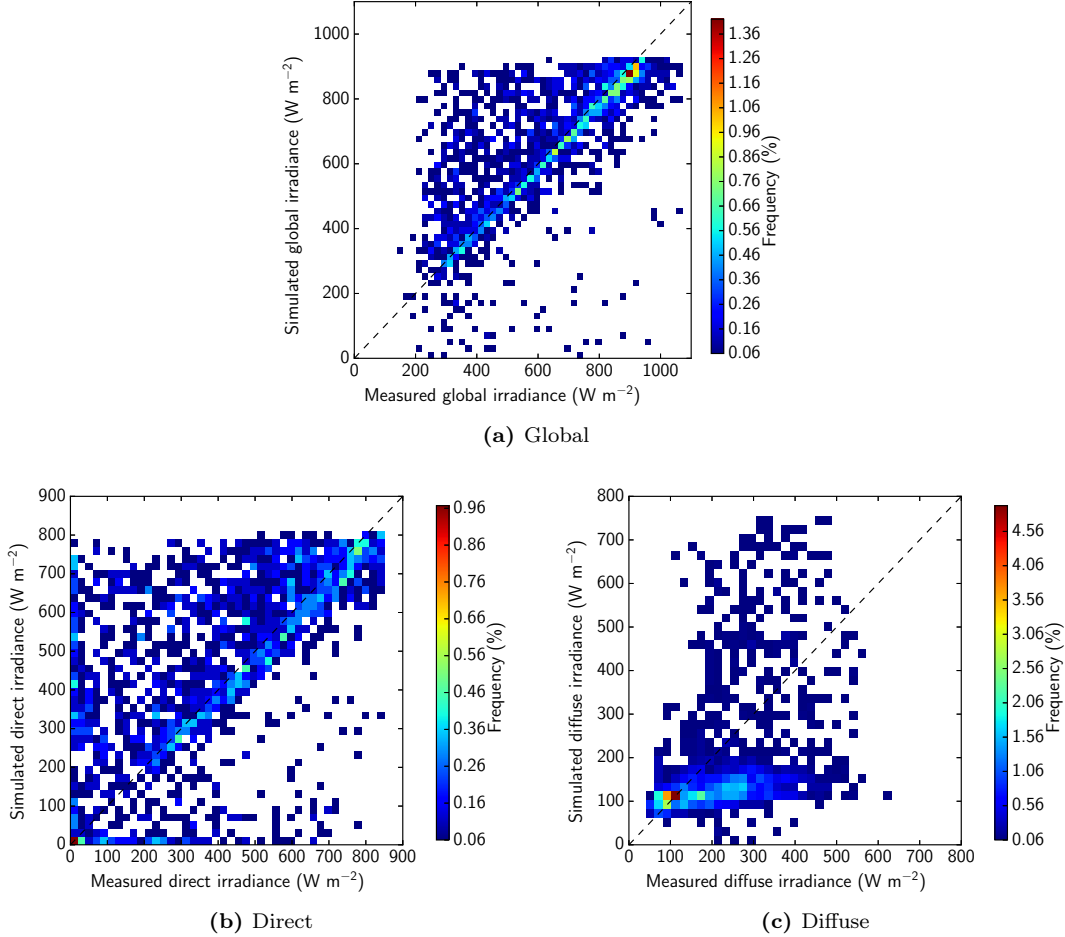


Figure 7.3.3: Modeled (MesoNH + PV) versus measured irradiance for all sky conditions in June at the SIRTA. Each square has a resolution of 20 W m^{-2} for the irradiances

events where the diffuse irradiance is importantly overestimated which can be noticed in Figure 7.3.3c correspond to cloudy-events wrongly modeled by small optical thicknesses whereas underestimations can originate from non-identified clear-sky events or from a cloud too optically thick.

In the cases of cloudy-sky conditions rightly identified by Meso-NH, errors in simulated irradiance can occur from the cloud cover or the cloud optical thickness. No measurements of cloud cover are available, however the maximum-random overlap hypothesis used in Meso-NH has been shown to generally underestimate the cloud cover (*Hogan & Bozzo 2016*). Therefore, changing the overlap hypothesis in Meso-NH should induce an amplification of the effects due to clouds in the simulations.

Estimations of the optical thickness for both simulated and measured sky conditions can be deduced following the method presented in Part 3.2. Figure 7.3.4 compares both optical thicknesses and confirms that the simulated optical thickness seems to saturate around 2, with only very few cases of thick clouds, which is coherent with the overestimation of direct and diffuse irradiances in overcast conditions, and confirms the possible explanation behind Figure 7.2.4b. Indeed, though these optical thicknesses are only estimations, it is unlikely that the uncertainty in the value can explain the difference between both measurements, especially that there is no influence of the SZA for each individual comparison as each compared timestep correspond to a given SZA.

The cloud optical thickness depends on the liquid water content and the effective radius of

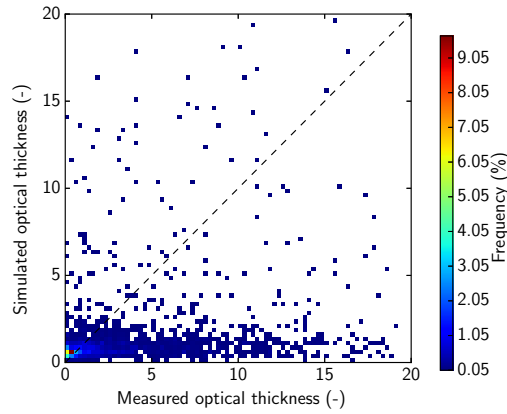


Figure 7.3.4: Modeled optical thickness from Meso-NH simulations and from observations for all sky conditions in June at the SIRTA. Each square has a resolution of 0.25

the droplets within the clouds thus providing two potential sources of error. The liquid water content simulated by Meso-NH has been retrieved thanks to the profiler but no observations are yet available for comparison. Therefore, a reason for this frequent saturation in optical thickness can not be determined at the present moment. However, the simulation of lower liquid water content or the use of a higher effective droplet radius than in reality can lead towards an underestimated optical thickness (equation (3.2.2)).

Besides the irradiance, the air temperature can also have an impact on PV production. Figure 7.3.5a compares the simulated and measured air temperature and shows a good modelisation by Meso-NH though the air temperature is often below the measured one. This underestimation is also compatible with the overestimation of the module power by the coupled model.

Last, the wind speed at 2 m is compared in Figure 7.3.5b. A large dispersion can be observed, however the post-processing of the 10 m-wind speed seems to work reasonably well. This post-processing step is important as the wind speed at 10 m can reach 11 m s^{-1} over the period of simulation. These higher wind speeds would cool the module down more, leading to more efficient operating conditions for the PV module and thus amplifying the global overestimation, which explains why the MRE of the coupled model would have been of 16.3% instead of 13.8% with the modelled 2m-wind speed.

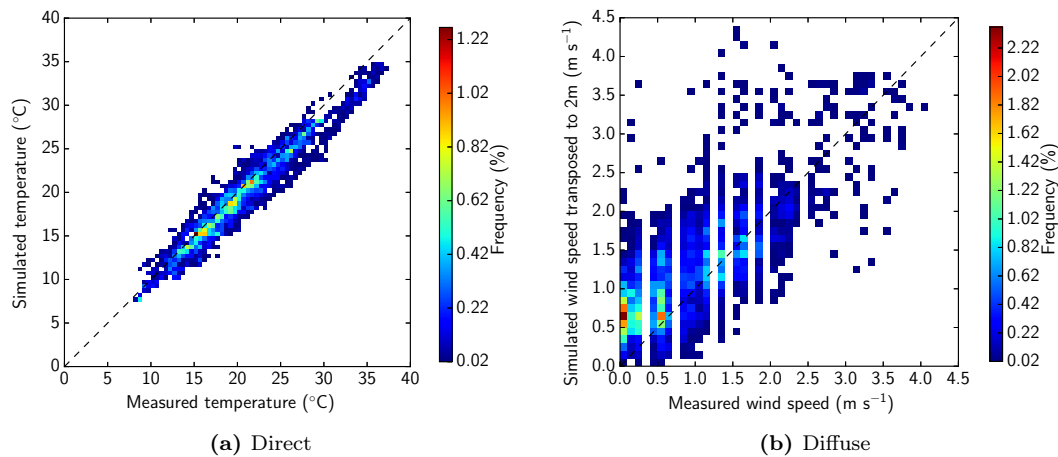


Figure 7.3.5: Modeled (MesoNH + PV) versus measured temperature and windspeed at 2m for all sky conditions in June at the SIRTA. Each square has a resolution of $0.5 \text{ }^\circ\text{C}$ or 0.1 m s^{-1}

CONCLUSION

8.1 Synthesis

The first achievement of this master's project is the development of a physically based PV model aimed at converting radiation outputs from atmospheric models or radiation measurements into PV production. One of its main specificities is its ability to physically account for the impact of the spectral distribution of solar irradiance. This is achieved via the spectralisation of broadband or narrow-band irradiance typical of observations or model outputs, according to reference high-resolution irradiance spectra. This spectralisation allows to add information on the distribution of irradiance within a band which is crucial when the sharp spectral dependence of PV materials has to be accounted for. The flexibility of the model allows it to process both refined spectral irradiances and broadband irradiances. Besides this spectral refinement, this model accounts for all steps relevant to the conversion of standard atmospheric variables into PV power: transposition of direct and diffuse fluxes into plane-of-array flux, optical losses at the interface of the solar panel, impact of temperature on the module efficiency, *etc.* Particular attention is paid for elementary models to be as physical as possible, in order to minimize the total number of free parameters of the model. This is done to ensure that the model remains applicable to any situation without requiring tuning. Each physical process can be modelled through a set of different options, the default ones having been selected through thorough comparison with *in situ* observations at the SIRTAs instrumental site. Its final format allows a user-friendly usage where the atmospheric conditions (temperature, wind speed, direct and diffuse spectral irradiances, spectral direct and diffuse ground albedo, solar zenith and azimuth angle), the characteristics of the module which are indicated on the manufacturer datasheet and the options are the only inputs required. The default options to be used have been assessed thanks to the measurements in June 2017 on the SIRTAs site though users can also decide which options to apply if wanted. The final PV model with the measured atmosphere at the SIRTAs simulated the power with a mean relative error of 0.2% in June and 3.7% in December 2017 for the monocrystalline silicon module installed on site, thus providing satisfactory results.

The model has then been used to study the impact of clouds on PV performance and indicates that clouds – by changing the contribution of direct and diffuse radiation and through spectral filtering – increase the module efficiency when considering the SW integrated irradiance. These results are in agreement with the literature.

The influence of the number of spectral bands provided by atmospheric models has also been investigated and shows that a lower level of knowledge leads to a loss in accuracy. More generally, this PV model proves that the global horizontal irradiance, which is the standard output of atmospheric models, is far from sufficient for PV modelling as it provides neither the angular nor the spectral properties of irradiance which are both critical for accurate modelling.

Starting from direct and diffuse fluxes improves the model, but increasing the spectral resolution of the atmospheric model can increase the quality of the model by a similar amount.

When compared to a simple PV model, the performance of the newly developed PV model is better, and highlights the relevance of accurately accounting for the spectral characteristics of the irradiance which is of uttermost importance in cloudy situations. This result is all the more promising that monocrystalline silicon cells are far from being the solar cells the most sensitive to spectral effects. Therefore a more drastic difference in performance is expected for PV modules with lower band gaps.

The PV model has been run on Meso-NH simulations for June 2017 at SIRTa. For this, all necessary variables have been extracted from Meso-NH and processed offline by the PV model. Comparison of simulated and measured PV production shows a mean relative error of 1.5% in clear-sky conditions but the latter increases to 13.8% when all sky conditions are considered.

Meso-NH simulations have been further analysed in order to understand the sources of error and with the ultimate goal of changing the parametrisations used (*e.g.* aerosols climatology, cloud optical properties, radiative transfer parametrisations) to improve the overall performance of the atmospheric model. The errors during clear-sky conditions are probably due to the climatology in ozone or aerosols applied in Meso-NH, though measurements of such variables would be required to confirm either of these hypotheses.

The higher errors during all-sky conditions mainly originated from the difficulty to accurately simulate the observed cloudy sky conditions. Sky conditions can be wrongly modelled as clear or cloudy by Meso-NH. However, even when Meso-NH correctly simulates a cloudy sky, the irradiance is often overestimated, which can be due to the underestimation of the total cloud cover or the cloud optical thickness. The lack of cloud cover measurements hinders further investigation of this possible explanation though the current overlap hypothesis is known to underestimate the cloud cover, therefore, a change in hypothesis would contribute towards a reduction in the relative error. The comparison of the optical thickness from the simulated and measured atmospheric conditions shows a frequent saturation of the simulated optical thickness below 2, which disables the creation of thicker clouds. This optical thickness can be due to lower liquid water content and a larger droplet size compared to reality.

Though the optimum goal of this research project is the implementation of a diagnostic tool in Meso-NH atmospheric model enabling PV power forecasting, much has been achieved during this master thesis towards this target, with the present success of an externally coupled model. The remaining tasks to reach the optimal goal are first to integrate the PV model into Meso-NH as the coupling is currently external, and second to assess the capacities in terms of forecasting as Meso-N has hitherto been forced every three hours by AROME analyses.

8.2 Outlook

Following this master project, future work can be carried out on several aspects.

First, sources of improvement within the PV model still remain. Most importantly, further validation should be carried out, with measurements from different locations or over other months of the year, which would allow a more statistically significant estimation of the error

and an evaluation of the uncertainty, but also the validation of the options used by default which have currently been determined over a restricted amount of data.

The PV model has been developed assuming that several spectral bands are supplied as an input, though the model is designed to accept any number of bands and hence also including broadband inputs. Indeed, the spectralisation step aims at refining the spectral resolution within each band by specifying the relative distribution along wavelengths but this technique is decreasingly accurate as the level of knowledge of the incoming irradiance deteriorates. Therefore, if a future use with restricted knowledge on the incoming irradiance is envisioned, it would be wise to add additional reference spectra for overcast conditions or the possibility of applying a correction factor in cases where only one band is provided.

Also, this spectral specificity of the developed code means that it is expected to have a positive impact on the accuracy for modules which are more sensitive to the spectral properties of radiation. It would be therefore interesting to test the model on other panels, especially for those of higher band gaps, where the impact is expected to be the biggest.

Another field of progress is the accuracy of Meso-NH simulations. For instance, it could be most beneficial to extract more measurements concerning the atmospheric conditions at the SIRTa in June, in particular the ozone, aerosol and more information on cloud properties from active remote sensing instruments, which would allow to further understand the errors arising from the atmospheric model. Climatologies and cloud optical properties parametrisations could consequently be updated in order to be closer to the real conditions at the SIRTa.

Moreover, ecRad has been recently implemented in Meso-NH; hence, launching Meso-NH simulations with this new radiative model would enable to simulate irradiances with fourteen shortwave bands (against six currently) as well as a better representation of the direct and diffuse radiation than the current scheme. Better angular and spectral properties are therefore expected and could contribute to an improvement in performance of the coupled model.

Also, in order to fully meet the initial optimum goal of this research project, the PV model must be implemented as an internal diagnostic tool into Meso-NH as it is currently being used externally. Furthermore, the forecasting accuracy of Meso-NH (or AROME) remains to be assessed for different forecasting horizons, especially in terms of radiation, in view of using the coupled model for power forecasting purposes.

Last, this newly developed PV model opens up new prospects, whether for operational or research projects.

For instance, the model can be used to produce climatology maps, thus providing a tool allowing to planify installations, study the choice of the module type depending on the localisation or devising an atlas of PV potential. A collaboration with the Direction of Meteorological Services at Météo-France is underway and the creation of an atlas over France thanks to AROME analyses is in progress.

Furthermore, the sensitivity of PV module to irradiance and more precisely to its angular and spectral properties, implies that PV production can potentially be used as a proxy of irradiance and in the long run be used for data assimilation. This prospect is all the more interesting that measurements of spectral or direct and diffuse irradiances are scarce whereas the installed PV capacity is soaring worldwide and generates a huge amount of data that could be processed, assuming that such data becomes easily accessible. This is an ambitious, though promising

venue for improving the parametrisation of radiative transfer in atmospheric models.

BIBLIOGRAPHY

- Almonacid, F., Rus, C., Pérez-Higueras, P. & Hontoria, L. (2011), ‘Calculation of the energy provided by a PV generator. Comparative study: conventional methods vs. artificial neural networks’, *Energy* **36**(1), 375–384.
- Amillo, A. M. G., Huld, T., Vourlioti, P., Müller, R. & Norton, M. (2015), ‘Application of satellite-based spectrally-resolved solar radiation data to PV performance studies’, *Energies* **8**(5), 3455–3488.
- Antonanzas, J., Osorio, N., Escobar, R., Urraca, R., Martinez-de Pison, F. & Antonanzas-Torres, F. (2016), ‘Review of photovoltaic power forecasting’, *Solar Energy* **136**, 78–111.
- Antonanzas, J., Pozo-Vázquez, D., Fernandez-Jimenez, L. & Martinez-de Pison, F. (2017), ‘The value of day-ahead forecasting for photovoltaics in the spanish electricity market’, *Solar Energy* **158**, 140–146.
- Badescu, V. (2002), ‘3D isotropic approximation for solar diffuse irradiance on tilted surfaces’, *Renewable Energy* **26**(2), 221–233.
- Berk, A., Bernstein, L. S. & Robertson, D. C. (1987), MODTRAN: A moderate resolution model for LOWTRAN, Technical report, Spectral Sciences Inc Burlington MA.
- Bohren, C. F. (1987), ‘Multiple scattering of light and some of its observable consequences’, *American Journal of Physics* **55**(6), 524–533.
- Bougeault, P., Mascart, P. & Chaboureaud, J. (2017), The Méso-NH atmospheric simulation system : scientific documentation, Technical report, Scientific documentation Tech. report. Météo-France/CNRM/GMME, Toulouse, France.
- Brandemuehl, M. & Beckman, W. (1980), ‘Transmission of diffuse radiation through CPC and flat plate collector glazings’, *Solar Energy* **24**(5), 511–513.
- Cano, D., Monget, J.-M., Albuisson, M., Guillard, H., Regas, N. & Wald, L. (1986), ‘A method for the determination of the global solar radiation from meteorological satellites data’, *Solar Energy* **37**(1), 31–39.
- Counihan, J. (1975), ‘Adiabatic atmospheric boundary layers: a review and analysis of data from the period 1880–1972’, *Atmospheric Environment (1967)* **9**(10), 871–905.
- Da Rosa, A. V. (2005), *Fundamentals of renewable energy processes*, 1. edn, Academic Press.
- Das, U. K., Tey, K. S., Seyedmahmoudian, M., Mekhilef, S., Idris, M. Y. I., Van Deventer, W., Horan, B. & Stojcevski, A. (2018), ‘Forecasting of photovoltaic power generation and model optimization: A review’, *Renewable and Sustainable Energy Reviews* **81**, 912–928.
- Davies, J. A. & Hay, J. E. (1980), Calculation of the solar radiation incident on a horizontal surface, in ‘proc. First can. Solar radiation data workshop. Ministry of supply and services, Canada’, pp. 32–58.

- De Soto, W., Klein, S. & Beckman, W. (2006), 'Improvement and validation of a model for photovoltaic array performance', *Solar Energy* **80**(1), 78–88.
- Diagne, M., David, M., Lauret, P., Boland, J. & Schmutz, N. (2013), 'Review of solar irradiance forecasting methods and a proposition for small-scale insular grids', *Renewable and Sustainable Energy Reviews* **27**, 65–76.
- Dirnberger, D., Blackburn, G., Müller, B. & Reise, C. (2015), 'On the impact of solar spectral irradiance on the yield of different PV technologies', *Solar Energy Materials and Solar Cells* **132**, 431–442.
- Ducrocq, V., Bouttier, F., Malardel, S., Montmerle, T. & Seity, Y. (2005), 'Le projet AROME', *La Houille Blanche* (2), 39–43.
- Duffie, J. A. & Beckman, W. A. (2013), *Solar engineering of thermal processes*, John Wiley & Sons.
- Dupré, O., Vaillon, R. & Green, M. A. (2016), *Thermal Behavior of Photovoltaic Devices: Physics and Engineering*, Springer, chapter Temperature Coefficients of Photovoltaic Devices.
- Erbs, D., Klein, S. & Duffie, J. (1982), 'Estimation of the diffuse radiation fraction for hourly, daily and monthly-average global radiation', *Solar Energy* **28**(4), 293–302.
- Evans, D. (1981), 'Simplified method for predicting photovoltaic array output', *Solar Energy* **27**(6), 555–560.
- Fouquart, Y. & Bonnel, B. (1980), 'Computations of solar heating of the earth's atmosphere—a new parameterization', *Beitraege zur Physik der Atmosphaere* **53**, 35–62.
- Fraunhofer Institute for Solar Energy Systems (2017), 'Photovoltaics report', Available at <https://www.ise.fraunhofer.de/content/dam/ise/de/documents/publications/studies/Photovoltaics-Report.pdf>, Accessed : January 2018 .
- Gal-Chen, T. & Somerville, R. C. (1975), 'On the use of a coordinate transformation for the solution of the Navier-Stokes equations', *Journal of Computational Physics* **17**(2), 209–228.
- Gangopadhyay, U., Jana, S. & Das, S. (2013), State of art of solar photovoltaic technology, in 'Conference Papers in Science', Vol. 2013, Hindawi Publishing Corporation.
- Ghitas, A. E. (2012), 'Studying the effect of spectral variations intensity of the incident solar radiation on the Si solar cells performance', *NRIAG Journal of Astronomy and Geophysics* **1**(2), 165–171.
- Gottschalg, R., Betts, T., Williams, S., Sauter, D., Infield, D. & Kearney, M. (2004), 'A critical appraisal of the factors affecting energy production from amorphous silicon photovoltaic arrays in a maritime climate', *Solar Energy* **77**(6), 909–916.
- Green, M. A. (1982), 'Accuracy of analytical expressions for solar cell fill factors', *Solar Cells* **7**(3), 337–340.
- Green, M. A., Hishikawa, Y., Warta, W., Dunlop, E. D., Levi, D. H., Hohl-Ebinger, J. & Ho-Baillie, A. W. (2017), 'Solar cell efficiency tables (version 50)', *Progress in Photovoltaics* **25**(7).

- Grell, G. A., Dudhia, J., Stauffer, D. R. et al. (1994), ‘A description of the fifth-generation Penn State/NCAR mesoscale model (MM5)’.
- Hale, G. M. & Querry, M. R. (1973), ‘Optical constants of water in the 200-nm to 200- μm wavelength region’, *Applied Optics* **12**(3), 555–563.
- Hogan, R. J. & Bozzo, A. (2016), *ECRAD: A new radiation scheme for the IFS*, European Centre for Medium-Range Weather Forecasts.
- Hogan, R. J., Schäfer, S. A., Klinger, C., Chiu, J. C. & Mayer, B. (2016), ‘Representing 3-d cloud radiation effects in two-stream schemes: 2. matrix formulation and broadband evaluation’, *Journal of Geophysical Research: Atmospheres* **121**(14), 8583–8599.
- Huld, T. & Amillo, A. M. G. (2015), ‘Estimating PV module performance over large geographical regions: The role of irradiance, air temperature, wind speed and solar spectrum’, *Energies* **8**(6), 5159–5181.
- IEA (2017), *Renewables 2017 - Analysis and Forecasts to 2022*, OECD Publishing.
- Ineichen, P., Perez, R., Seal, R., Maxwell, E. & Zalenka, A. (1992), ‘Dynamic global-to-direct irradiance conversion models’, *Ashrae Transactions* **98**(1), 354–369.
- Inman, R. H., Pedro, H. T. & Coimbra, C. F. (2013), ‘Solar forecasting methods for renewable energy integration’, *Progress in Energy and Combustion Science* **39**(6), 535–576.
- Jardine, C. N., Conibeer, G. J. & Lane, K. (2001), PV-COMPARE: direct comparison of eleven PV technologies at two locations in northern and southern Europe, in ‘Seventeenth EU PVSEC’.
- Jerez, S., Tobin, I., Vautard, R., Montávez, J. P., López-Romero, J. M., Thais, F., Bartok, B., Christensen, O. B., Colette, A., Déqué, M. et al. (2015), ‘The impact of climate change on photovoltaic power generation in Europe’, *Nature communications* **6**, 10014.
- Jimenez, P. A., Hacker, J. P., Dudhia, J., Haupt, S. E., Ruiz-Arias, J. A., Gueymard, C. A., Thompson, G., Eidhammer, T. & Deng, A. (2016), ‘WRF-Solar: Description and clear-sky assessment of an augmented NWP model for solar power prediction’, *Bulletin of the American Meteorological Society* **97**(7), 1249–1264.
- King, D. L., Boyson, W. E. & Kratochvil, J. A. (2004), Photovoltaic array performance model., Technical report, Sandia National Laboratories.
- Kirn, B. & Topic, M. (2017), ‘Diffuse and direct light solar spectra modeling in PV module performance rating’, *Solar Energy* **150**, 310–316.
- Klucher, T. M. (1979), ‘Evaluation of models to predict insolation on tilted surfaces’, *Solar Energy* **23**(2), 111–114.
- Kokhanovsky, A. (2004), ‘Optical properties of terrestrial clouds’, *Earth-Science Reviews* **64**(3-4), 189–241.
- Kokhanovsky, A. & Rozanov, V. (2003), ‘The reflection function of optically thick weakly absorbing turbid layers: a simple approximation’, *Journal of Quantitative Spectroscopy and Radiative Transfer* **77**(2), 165–175.

- Kopp, G. & Lean, J. L. (2011), ‘A new, lower value of total solar irradiance: Evidence and climate significance’, *Geophysical Research Letters* **38**(1).
- Kostylev, V. & Pavlovski, A. e. a. (2011), Solar power forecasting performance-towards industry standards, in ‘1st International Workshop on the Integration of Solar Power into Power Systems, Aarhus, Denmark’.
- Krauter, S. & Hanitsch, R. (1996), ‘Actual optical and thermal performance of PV-modules’, *Solar Energy Materials and Solar Cells* **41**, 557–574.
- Lafore, J., Stein, J., Asencio, N., Bougeault, P., Ducrocq, V., Duron, J., Fischer, C., HeÂreil, P., Mascart, P., Pinty, V. M. J. et al. (1998), ‘The Meso-NH Atmospheric Simulation System. Part I: adiabatic formulation and control simulations’, *Ann. Geophysicae* **16**, 90–109.
- Libois, Q. (2014), Evolution of snow physical properties on the Antarctic Plateau. Observing and modeling radiative transfer and snow metamorphism, Thesis, Université de Grenoble.
- Liou, K.-N. (2002), *An introduction to atmospheric radiation*, Vol. 84, Academic press.
- Lorenzo, E. (2003), ‘Energy collected and delivered by PV modules’, *Handbook of photovoltaic science and engineering* pp. 905–970.
- Loutzenhiser, P., Manz, H., Felsmann, C., Strachan, P., Frank, T. & Maxwell, G. (2007), ‘Empirical validation of models to compute solar irradiance on inclined surfaces for building energy simulation’, *Solar Energy* **81**(2), 254–267.
- Manwell, J. F., McGowan, J. G. & Rogers, A. L. (2010), *Wind energy explained: theory, design and application*, John Wiley & Sons.
- Martin, N. & Ruiz, J. (2001), ‘Calculation of the PV modules angular losses under field conditions by means of an analytical model’, *Solar Energy Materials and Solar Cells* **70**(1), 25–38.
- Mavromatakis, F., Vignola, F. & Marion, B. (2017), ‘Low irradiance losses of photovoltaic modules’, *Solar Energy* **157**, 496–506.
- Mayer, B. & Kylling, A. (2005), ‘The libRadtran software package for radiative transfer calculations-description and examples of use’, *Atmospheric Chemistry and Physics* **5**(7), 1855–1877.
- Messenger, R. & Ventre, J. (2004), *Photovoltaic Systems Engineering, Second Edition*, Taylor & Francis.
- Mlawer, E. J., Taubman, S. J., Brown, P. D., Iacono, M. J. & Clough, S. A. (1997), ‘Radiative transfer for inhomogeneous atmospheres: RRTM, a validated correlated-k model for the longwave’, *Journal of Geophysical Research: Atmospheres* **102**(D14), 16663–16682.
- Myers, D., Emery, K. & Gueymard, C. (2002), Proposed reference spectral irradiance standards to improve concentrating photovoltaic system design and performance evaluation, in ‘Photovoltaic Specialists Conference, 2002. Conference Record of the Twenty-Ninth IEEE’, IEEE, pp. 923–926.
- Myers, D. R. & Gueymard, C. A. (2004), Description and availability of the SMARTS spectral model for photovoltaic applications, in ‘SPIE proceedings series’, Society of Photo-Optical Instrumentation Engineers, pp. 56–67.

- Nofuentes, G., García-Domingo, B., Muñoz, J. & Chenlo, F. (2014), ‘Analysis of the dependence of the spectral factor of some PV technologies on the solar spectrum distribution’, *Applied Energy* **113**, 302–309.
- Pelland, S., Galanis, G. & Kallos, G. (2013), ‘Solar and photovoltaic forecasting through post-processing of the Global Environmental Multiscale numerical weather prediction model’, *Progress in photovoltaics: Research and Applications* **21**(3), 284–296.
- Perez, R., Ineichen, P., Seals, R., Michalsky, J. & Stewart, R. (1990), ‘Modeling daylight availability and irradiance components from direct and global irradiance’, *Solar Energy* **44**(5), 271–289.
- Perez, R., Seals, R., Ineichen, P., Stewart, R. & Menicucci, D. (1987), ‘A new simplified version of the Perez diffuse irradiance model for tilted surfaces’, *Solar Energy* **39**(3), 221–231.
- Petty, G. W. (2002), ‘Area-average solar radiative transfer in three-dimensionally inhomogeneous clouds: The independently scattering cloudlet model’, *Journal of the atmospheric sciences* **59**(20), 2910–2929.
- Polman, A., Knight, M., Garnett, E. C., Ehrler, B. & Sinke, W. C. (2016), ‘Photovoltaic materials: Present efficiencies and future challenges’, *Science* **352**(6283), aad4424.
- Qu, Z., Oumbe, A., Blanc, P., Espinar, B., Gesell, G., Gschwind, B., Klüser, L., Lefèvre, M., Sabet, L., Schroedter-Homscheidt, M. et al. (2017), ‘Fast radiative transfer parameterisation for assessing the surface solar irradiance: The heliosat-4 method’, *Meteorologische Zeitschrift* **26**(1), 33–57.
- Razykov, T. M., Ferekides, C. S., Morel, D., Stefanakos, E., Ullal, H. S. & Upadhyaya, H. M. (2011), ‘Solar photovoltaic electricity: Current status and future prospects’, *Solar Energy* **85**(8), 1580–1608.
- Reindl, D., Beckman, W. & Duffie, J. (1990a), ‘Evaluation of hourly tilted surface radiation models’, *Solar Energy* **45**(1), 9 – 17.
- Reindl, D. T., Beckman, W. A. & Duffie, J. A. (1990b), ‘Diffuse fraction correlations’, *Solar energy* **45**(1), 1–7.
- REN21 (2017), *Renewables 2017 Global Status Report*.
- Rieger, D., Steiner, A., Bachmann, V., Gasch, P., Förstner, J., Deetz, K., Vogel, B. & Vogel, H. (2017), ‘Impact of the 4 April 2014 Saharan dust outbreak on the photovoltaic power generation in Germany’, *Atmospheric Chemistry and Physics* **17**(21), 13391.
- Sabry, M. & Ghitas, A. E. (2007), ‘Influence of temperature on methods for determining silicon solar cell series resistance’, *Journal of Solar Energy Engineering* **129**(3), 331–335.
- Sampaio, P. G. V. & González, M. O. Q. (2017), ‘Photovoltaic solar energy: Conceptual framework’, *Renewable and Sustainable Energy Reviews* **74**, 590–601.
- Schaub, P., Mermoud, A., Guisan, O. & Mermoud, A. (1994), *Evaluation of the different losses involved in two photovoltaics systems*.
- Singh, P. & Ravindra, N. M. (2012), ‘Temperature dependence of solar cell performance—an analysis’, *Solar Energy Materials and Solar Cells* **101**, 36–45.

- Sjerps-Koomen, E., Alsema, E. & Turkenburg, W. (1996), ‘A simple model for PV module reflection losses under field conditions’, *Solar Energy* **57**(6), 421–432.
- Skamarock, W. C., Klemp, J. B., Dudhia, J., Gill, D. O., Barker, D. M., Wang, W. & Powers, J. G. (2005), A description of the advanced research WRF version 2, Technical report, National Center For Atmospheric Research Boulder Co Mesoscale and Microscale Meteorology Div.
- Skoplaki, E., Boudouvis, A. & Palyvos, J. (2008), ‘A simple correlation for the operating temperature of photovoltaic modules of arbitrary mounting’, *Solar Energy Materials and Solar Cells* **92**(11), 1393–1402.
- Slingo, A. (1989), ‘A gcm parameterization for the shortwave radiative properties of water clouds’, *Journal of the Atmospheric Sciences* **46**(10), 1419–1427.
- Stark, C. & Theristis, M. (2015), The impact of atmospheric parameters on the spectral performance of multiple photovoltaic technologies, *in* ‘Photovoltaic Specialist Conference (PVSC), 2015 IEEE 42nd’, IEEE, pp. 1–5.
- Warren, S. G. & Brandt, R. E. (2008), ‘Optical constants of ice from the ultraviolet to the microwave: A revised compilation’, *Journal of Geophysical Research: Atmospheres* **113**(D14).
- Yi, H., Bardosa, J., Nassar, J., Migan, A. & Bourdin, V. (2015), Modeling and measurement of spectral solar irradiance at SIRTAs: Applications to photovoltaic performance studies, Master’s thesis, Ecole Polytechnique, Palaiseau, France.

APPENDIX A

CLOUD OPTICAL THICKNESS FROM THE PHYSICAL PROPERTIES OF CLOUDS

A.1 Deriving the optical thickness physical expression

Determining the optical thickness thanks to the physical properties (LWC and r_{eff}) is equivalent to knowing the extinction coefficient as a function of altitude according to (3.2.1).

The extinction coefficient is determined by the number of drops per volume unit n_{drops} and their extinction surface C^{ext} (*Libois 2014, Liou 2002*):

$$\sigma_e = n_{\text{drops}} C^{\text{ext}} \quad (\text{A.1.1})$$

The extinction surface can be assumed to be the double of the apparent area Σ equal to πr_{eff}^2 under the hypothesis of spherical drops (*Libois 2014*):

$$C^{\text{ext}} = 2\Sigma = 2\pi r_{\text{eff}}^2 \quad (\text{A.1.2})$$

The number of drops per volume unit can be deduced from the definition of LWC and r_{eff} assuming monodisperse distribution of the droplet size:

$$n_{\text{drops}} = \frac{LWC}{\rho_w \frac{4}{3} \pi r_{\text{eff}}^3} \quad (\text{A.1.3})$$

Hence, one gets

$$\sigma_e = \frac{3 LWC}{2 \rho_w r_{\text{eff}}^3} \quad (\text{A.1.4})$$

A.2 Deriving the liquid water content from the liquid water mixing ratio

The liquid water content is not often directly provided in which case it must be derived from the liquid water mixing ratio.

By definition, the liquid water content is the mass of water in a cloud in the specified amount of dry air expressed in kg m^{-3} whereas the liquid water mixing ratio q_{liq} (dimensionless) the ratio of the mass of liquid water to the mass of dry air. These two variables are therefore directly by the air density ρ :

$$LWC = q_{\text{liq}} \times \rho = q_{\text{liq}} \times \frac{PM}{RT} \quad (\text{A.2.1})$$

with $M \approx 0.029 \text{ kg mol}^{-1}$ the molecular weight of dry air, R the gas constant, P the pressure

and T the temperature. In other terms, when used to compute the cloud optical thickness, the local pressure and temperature must also be known at all altitudes within the cloud.

APPENDIX B

REVIEW OF PV TECHNOLOGIES

The different PV technologies can be divided into three main groups, (*Sampaio & González 2017*) :

1. First generation technologies which are now fully commercialised and are based on silicon-crystalline technologies(c-Si) : monocrystalline (sc-Si) and multicrystalline (mc-Si);
2. Second generation technologies or thin film photovoltaic technologies, which are new on the market and include mainly the following families :
 - amorphous (a-Si) and micro-amorphous (a-Si/ μ c-Si) silicon;
 - cadmium telluride (CdTe);
 - copper indium selenide (CIGS) and copper, indium gallium diselenide (CIS);
3. Third generation technologies, which are still being developed or are still in demonstration, such as organic photovoltaic technologies.

When comparing photovoltaic technologies, different criteria must be considered : the cell efficiency, but also their behaviour with temperature or humidity, their cost, their life time and their ecological aspect.

B.1 First generation technologies

Crystalline silicon cells currently represent 90% of the PV cell market (*Sampaio & González 2017*). The main advantages of these cells are that silicon is abundant (it is the second most abundant element on Earth), stable and non-toxic. Furthermore, it is now a well-known technology and readily compatible with silicon-based microelectronics industry (*Sampaio & González 2017*). Its lifetime has also been demonstrated to be of more than 20 years.

B.1.1 Monocrystalline silicon m-Si

Monocrystalline silicon solar cells achieve high efficiencies (*Gangopadhyay et al. 2013*) but require very pure materials with perfect crystal structures (Czochralski process). Consequently, the energy requirements and manufacturing costs are high, leading to long energy return time (*Sampaio & González 2017*).

B.1.2 Polycrystalline silicon p-Si (or multicrystalline silicon mc-Si)

The drawbacks of m-Si has lead to the development of the polycrystalline silicon solar cell (p-Si or mc-Si) : thanks to lower standards for the crystals (which no longer need to be perfect), cost reduction and an increase in production rate can be achieved (*Sampaio & González 2017*). However, this goes hand in hand with a decrease in efficiency.

B.1.3 Thin films

Thin films are thinner than classical crystalline silicon modules. However, this means that the absorption of solar radiation must be improved to achieve similar efficiencies. This can be achieved by using materials with a broad absorption or by using different narrow-band absorbers which are superposed (*Razykov et al. 2011*).

Thin films generally require lower capital costs as the production and material costs are reduced : less material from the semiconductor needs to be manufactured (up to 99% less than crystalline solar cells) (*Gangopadhyay et al. 2013, Sampaio & González 2017*). This technology is also highly flexible, easy to install and can be manufactured in one step. They can therefore be applied on flexible and lightweight structures or easily integrated into building components.

However, their efficiency is considerably reduced compared to crystalline silicon systems (5–13 % instead of 11–20%), (*Sampaio & González 2017*)

B.1.4 Amorphous silicon (a-Si)

Amorphous silicon benefits from the Si elemental abundance and has a higher absorption coefficient than crystalline silicon. The deposition can be done for a wide range of temperatures (though room temperature deposition induces lower quality thus lower efficiency than if higher temperature are used) (*Sampaio & González 2017*) and the manufacturing technique is easily scalable.

Contrarily to crystalline silicon, the silicon atoms of the amorphous silicon (a-Si) cell are randomly located with each other leading to a larger gap (*Sampaio & González 2017*). Furthermore, the cell initially degraded by light as Si-H bonds are destroyed. The stabilized efficiency should thus be considered (only 6-7% for best commercial modules) (*Razykov et al. 2011, Sampaio & González 2017*).

B.1.5 Micro-amorph silicon (a-Si/ μ c-Si)

Micro-amorph silicon (a-Si/ μ c-Si) cells are constituted of two layers : an upper layer of a-Si (which converts shorter wavelengths of visible solar) and a lower layer of microcrystalline silicon (which is most effective in converting longer wavelengths). Higher efficiencies than a-Si can therefore be achieved (8-9 %) (*Sampaio & González 2017*)

B.1.6 Cadmium telluride (CdTe)

Cadmium telluride is often considered as the most promising thin film technology to reach low manufacturing costs and high efficiency, (*Sampaio & González 2017*), but has a non negligible drawback : Cadmium is toxic and environmental concerns has lead Cd to even be banned in some countries. Also, the availability of Te is an issue, as mass production of CdTe cells could lead to the scarcity of this raw material, hence also affecting the material cost (*Sampaio & González 2017*).

CdTe modules have many advantages, including the possibility to be deposited at low temperature (*Polman et al. 2016*), a cost-effective production, good performance in high temperatures and low-light conditions. Its steep absorption coefficient versus energy means that the current collection is good (*Polman et al. 2016*).

B.1.7 GaAs

The record efficiency for a single-junction solar cell under one-sun illumination (not concentrated) has been achieved by the GaAs solar cell (28.8% efficiency). Consequently, GaAs modules are used for applications where high efficiencies on small areas need to be achieved, such as space. GaAs modules were introduced in space power applications in the late 1980s as they have high efficiency and lower radiation-induced degradation than Si cells (*Razykov et al. 2011*)

The main drawback of GaAs modules is the use of arsenic – a toxic element – in the manufacture (*Sampaio & González 2017, Polman et al. 2016*), and the cost of Gallium.

B.1.8 Copper indium selenide (CIGS) and copper, indium gallium diselenide (CIS)

CIS and CIGS have high optical absorption coefficients, which enables the use of a very thin layer (*Sampaio & González 2017, Razykov et al. 2011*). The absorption varies close to the band gap, leading to current loss in the near-band gap spectral range (*Polman et al. 2016*). The manufacturing technique allows a high throughput processing of a low cost system. Furthermore, the resulting material is flexible, roll-able and light. Its tolerance to space radiation is also higher than silicon or GaAs which means that this technology is excellent for space applications given also that its lightweight and roll-able characteristics could reduce the overall cost of the space-deployable solar modules (including the launching costs) (*Razykov et al. 2011*).

However, this technology undergoes degradation under wet conditions (*Sampaio & González 2017*) and the scarcity of In could be an issue for increasing the CIGS market (*Polman et al. 2016, Razykov et al. 2011*)

B.1.9 Thin film c-Si, pc-Si

Other manufacturing techniques allow to create Si thin films (such as Crystalline Silicon on Glass (CSG), with the direct deposition of silicon on glass then by solid-phase crystallisation). The silicon can then be deposited on low-cost and module-sized substrates and in integrally interconnected structures (*Razykov et al. 2011*). The efficiency is drastically reduced (8.2% for c-Si thin films and 13.7% for p-Si thin films).

B.2 Third generation

B.2.1 Organic cells

Organic semiconductors are less expensive than inorganic semiconductors and the inexpensive roll-to-roll fabrication (high production rate and no technical challenges as there is no need for high temperature or vacuum conditions) makes this technology economically interesting for large-scale production. Furthermore, the organic PV cells are non-toxic, lightweight and can be manufactured into flexible modules of different shapes, colours and transparencies. The applications are much wider than those of other thin-film technologies (*Sampaio & González 2017, Razykov et al. 2011, Polman et al. 2016*).

The highest reported efficiency is currently 11.5% (*Polman et al. 2016*), which remains low.

The main challenge of organic cell devices is its durability as the organic materials degrade under illumination. However, with careful design and choice of materials, the lifetime can be increased.

B.2.2 Dye-Sensitized Solar Cells (DSSC)

Dye-Sensitized Solar Cells (DSSC) are hybrid cells as they are made of organic and inorganic materials. It differs from other PV cells by the separation of the light-absorbing mechanism (by the dye) from the transport mechanism of the charge carriers, (*Sampaio & González 2017*). Consequently, impure raw materials and a simple cell processing can be used, thus reducing the manufacturing cost. DSSC can also be fabricated in different colours and transparencies.

The efficiencies are promising though still low (on the order of 7-11 % only), but the main issue is the limited large-scale applications as organometallic dyes as ruthenium and porphyrins are difficult to synthesise and purify, and the availability of ruthenium is limited, (*Sampaio & González 2017*)

APPENDIX C

SIRTA DATASET

Table [C.0.1](#) provides information on the measured variables at the SIRTA (*e.g.* spectral range, accuracy, location).

Table C.0.1: Installed instruments, corresponding variables and accuracies

Instrument	Location	Variables	Time resolution	Specificities	Accuracy
–	Panels	Pmax_X, Tp_X, Vmax_X, Imax_X, Voc_X, Isc_X, FP_X for all five modules X	1min sampling, 10min average	–	–
Anemometre	Mounted with panels	WS_ms_2	10min average	–	–
Thermometre	Mounted with panels	AirTC	10min average	–	–
–	–	RH	10min average	–	–
–	–	rain_sum	10min average	–	–
CMP22 Kipp & Zonen Pyranometer	Approx 620m South of panels	Diffuse_Solar_Flux, Global_Solar_Flux	10min average	spectral range : 200 – 3600nm	Directionnal response : 5 W m^{-2} ^a
SHP1 Kipp & Zonen Pyrheliometer	Approx 620m South of panels	Direct_Solar_Flux	10min average	spectral range : 200 – 4000 nm	–
RG100 Solems Photodiode	Mounted with panels	POA	1min sampling, 10min average	spectral range : 400 – 1100 nm	$\pm 10\%$ ^b
CM3 Kipp & Zonen Pyranometre	Mounted with panels	CN3Dn	10s sampling, 10min average	spectral range : 300 – 3000 nm	Expected accuracy for daily sums: $\pm 10\%$, directional error (at 1000 W m^{-2}) $< +25 \text{ W m}^{-2}$ ^c
photometre (AERONET)	Approx 700m South of panels	Day_of_Year, AOD_1640nm, AOD_1020nm, AOD_870nm, AOD_675nm, AOD_560nm, AOD_440nm, AOD_380nm, AOD_340nm, Precipitable_Water(cm), 440-870_Angstrom_Exponent, 380-500_Angstrom_Exponent, 500-870_Angstrom_Exponent, 340-440_Angstrom_Exponent, Ozone(Dobson)	10min average	–	–
EKO MS-700 Spectroradiometer	–	Spectral irradiances	1min	spectral range : 350nm – 1050nm	Wavelength accuracy $< 0.3\text{nm}$, cosine response $< 7\%$ ^d

^a<http://www.kippzonen.com/Product/15/CMP22-Pyranometer>

^b<http://www.solems.com/detecteurs-de-rayonnement>

^c<https://www.campbellsci.com/cm3>

^d<https://eko-eu.com/products/solar-energy/spectroradiometers/ms-700n-spectroradiometer>

APPENDIX D

PV MODEL: SCIENTIFIC DOCUMENTATION

D.1 Main components of PV modeling

The operating power of a PV cell can be computed from the fill factor, the short-circuit current and the open-circuit voltage following

$$P = FF \times I_{SC} \times V_{OC} \quad (\text{D.1.1})$$

The PV model must therefore compute these three variables.

The fill factor depends on the series resistance, which can be computed from the manufacturer's datasheet specifications.

The operating properties of the solar cell also depend on the temperature, thus requiring to model the cell temperature.

Finally, the last essential ingredient is the photo-generated current, which results both from the spectral response of the solar cell and the cell-impacting irradiance.

The code can therefore be simply represented as in Figure [D.1.1](#).

D.2 Modelling the cell-impacting irradiance

Modelling the irradiance impacting the solar cells implies :

- Adding spectral resolution to the band simulated or measured direct and diffuse horizontal irradiances (in order to be able to apply a spectral response),
- Computing the spectral POA irradiance from those on a horizontal surface,
- Applying optical losses, to account for reflection at each interface and absorption of all layers preceding the solar cell.

D.2.1 Spectralisation

The spectralisation step is important due to the sensitivity of the solar cell to the wavelength. The irradiances, whether output by atmospheric models or measured, generally correspond to broadband values (*i.e.* integrated over the SW) or in the best case to narrow bands (like the six bands which can be retrieved from Meso-NH). However, in both cases, the spectral resolution is not fine enough to directly apply the spectral characteristics of the solar cell as the sharp cut of the spectral response at λ_{gap} does not necessarily match the boundary of a numerical band. The spectralisation step therefore aims at specifying the distribution of irradiance within the bands provided.

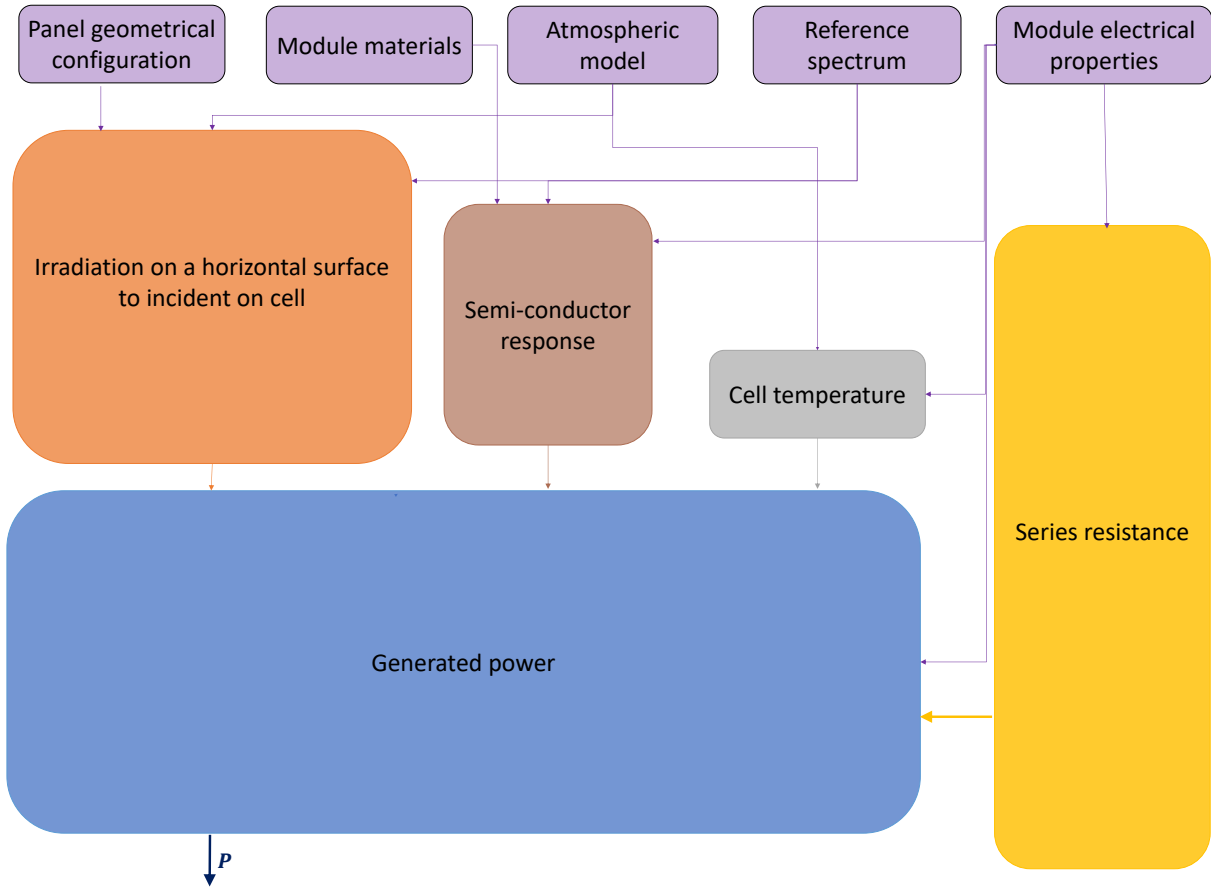


Figure D.1.1: Simplified diagram of the PV code

Accounting for the spectral resolution The ASTM G173-03 spectrum is the reference for the STC. Yet, it considers a specific state of the atmosphere whereas the surface irradiance spectrum is strongly variable with the air mass (or solar zenith angle SZA).

Furthermore, the ASTM G173-03 spectrum considers the irradiance on an inclined surface $\beta_{\text{STC}} = 37^\circ$ meaning that the transposition step has already been applied, and the spectrum for a different inclination would be different due to a change in contribution of the different subcomponents. A more optimal approach thus consists in spectralising the direct and diffuse irradiance separately on a horizontal surface, then applying the chosen transposition model to obtain the spectralised POA irradiance. Spectralising the direct and diffuse irradiances thus requires other reference spectra.

Figure D.2.1 shows the different MODTRAN-simulated spectra for various SZAs under clear-sky (USSA conditions). Figure D.2.1b corresponds to the spectra normalised by the total irradiance on the domain that silicon cells are sensitive to and highlights that the irradiance is not identically distributed over the wavelengths with varying SZA. This observation must therefore be accounted for in PV modelisation.

In order to account for the influence of SZA on the irradiance, spectral resolution is added to the direct and diffuse radiation by considering MODTRAN spectra simulated under USSA with the solar zenith angle ranging from 5° to 85° with an angle resolution of 5° . MODTRAN radiative transfer code provides both direct and diffuse irradiance at a high spectral resolution. The spectrum considered for the spectralisation is the SZA-interpolated spectrum from the eighteen simulated spectra. This hypothesis of linear behaviour for a SZA variation of less than

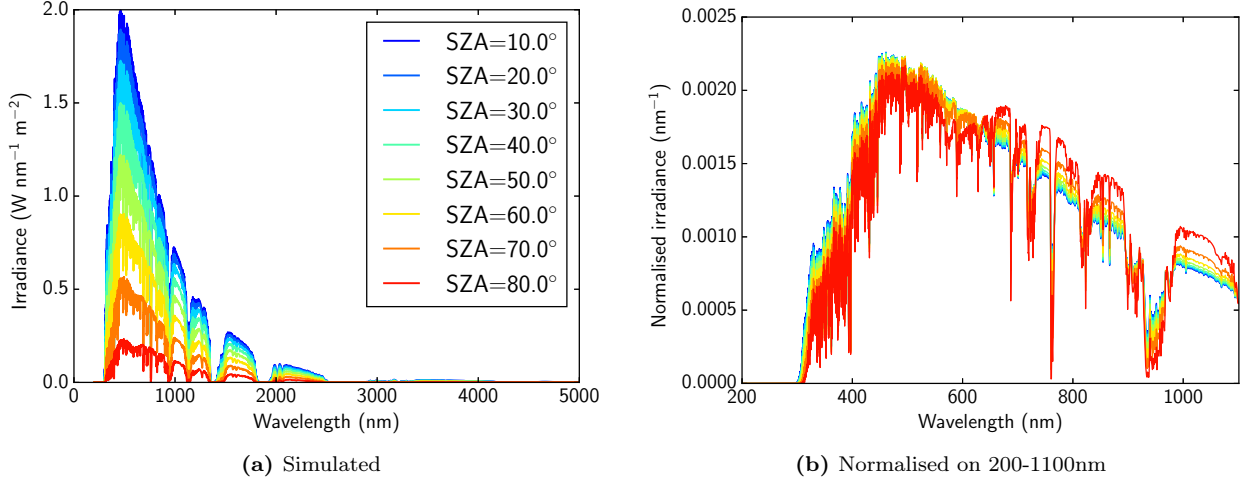


Figure D.2.1: MODTRAN-simulated spectra considering the USSA conditions with SZA varying between 10 and 80° and the same spectra normalised by their integral between 200nm and 1100nm.

5° is conformed by Figure D.2.2 which illustrates for different wavelengths the evolution of global spectral irradiance with SZA.

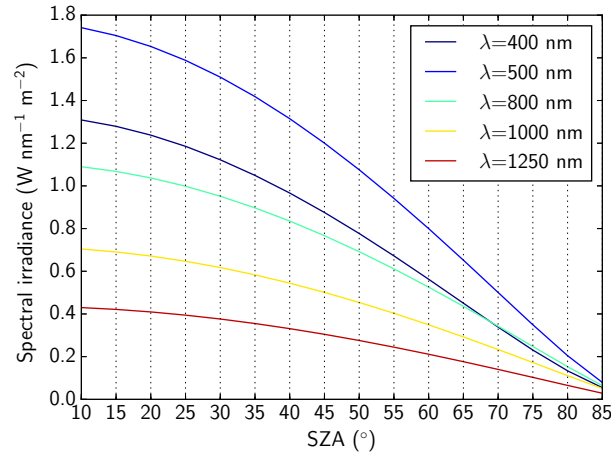


Figure D.2.2: Global spectral irradiance for different wavelengths and solar zenith angles.

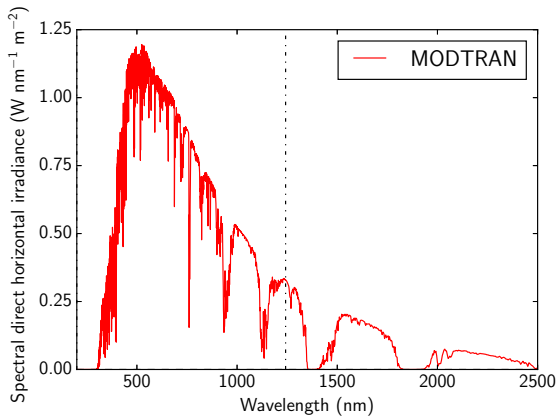
Applied method Given that the spectral signature is different for direct and diffuse radiation, both components are spectralised independently by considering the reference direct (resp.diffuse) component of the reference spectrum.

First, the reference spectrum G_{ref} is computed given the SZA by interpolating the MODTRAN spectra considering only the direct (or diffuse) component (Figure D.2.3a). The irradiance to be spectralised corresponds to the integration over a wavelength domain $I_k = [\lambda_k; \lambda_{k+1}]$ (Figure D.2.3b). This integrated value is spectralised by considering for $\lambda \in I_k = [\lambda_k; \lambda_{k+1}]$:

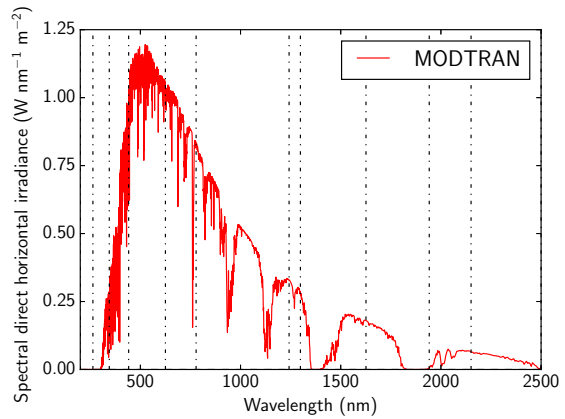
$$G(\lambda) = G(I_k) \cdot \frac{G_{ref}(\lambda)}{\int_{\lambda_k}^{\lambda_{k+1}} G_{ref}(\lambda) d\lambda} \quad (\text{D.2.1})$$

which leads to a spectrum of the same resolution and shape as the reference spectrum but with the same integrated irradiance as the input (Figure D.2.3c).

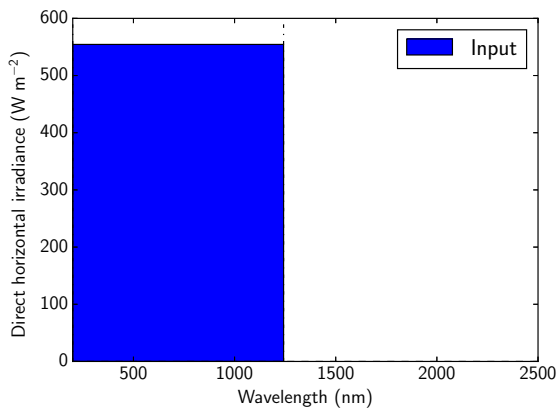
In the case of spectral irradiances given for different bands, the method is the same by



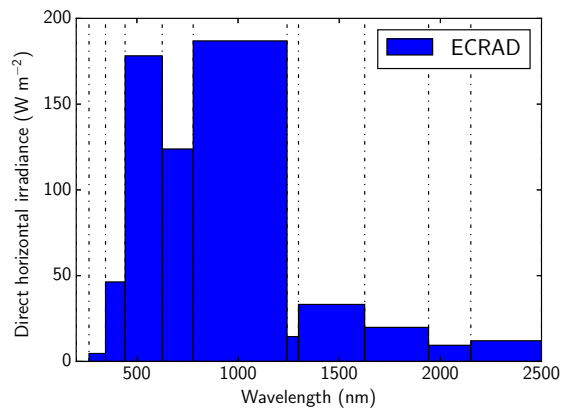
(a) Reference spectrum given the SZA



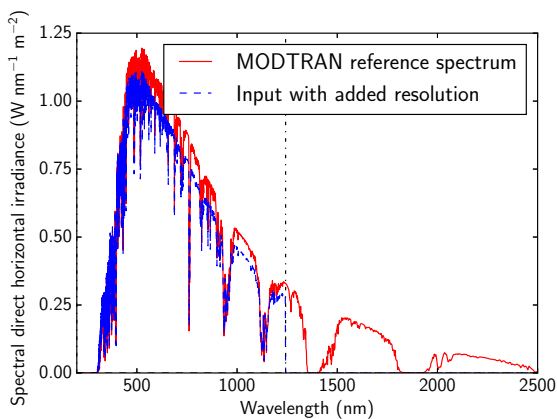
(a) Reference spectrum given the SZA



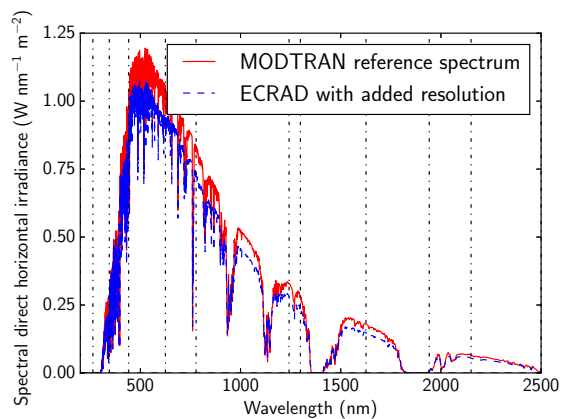
(b) Given irradiance



(b) Given irradiance



(c) Spectralisation



(c) Spectralisation

Figure D.2.3: Spectralisation method for a global irradiance. The example for an irradiance measured over 200-1100nm is given.

Figure D.2.4: Spectralisation method for given spectral irradiance. The dotted lines correspond to the different bands measured

treating each band independently, as shown in Figure D.2.4. This spectralisation thus does not aim at correcting the reference spectrum to the integrated value of the input irradiance, but rather to add information to the input on the relative spectral distribution within each band.

D.2.2 Transposition models

The POA irradiance results from the contribution of the beam, the ground-reflected and the diffuse component *Reindl et al. (1990a)*. Transposition models are then required to compute these contributions from irradiances on a horizontal surface.

D.2.2.1 Direct irradiance

The direct irradiance on a tilted plane is computed following

$$G_{b,POA} = \frac{\cos(\theta_b)}{\cos(SZA)} \cdot G_b \quad (D.2.2)$$

with θ_b the angle-of-incidence (AOI) for the direct irradiance on the tilted panel.

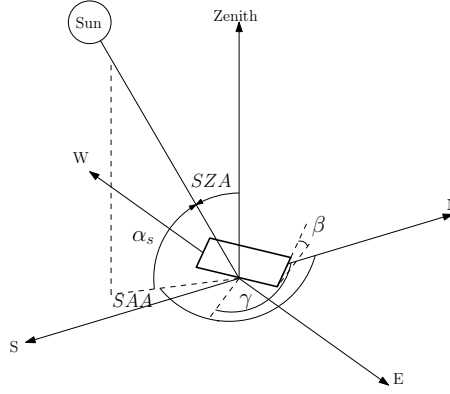


Figure D.2.5: Parameters defining the position of the sun and the orientation of the photovoltaic panel, adapted from *Duffie & Beckman (2013)*

The angle-of-incidence for the beam irradiance θ_b , is calculated thanks to (*Duffie & Beckman 2013*):

$$\begin{aligned} \cos(\theta_b) = & \sin(\delta) \sin(\phi) \cos(\beta) - \sin(\delta) \cos(\phi) \sin(\beta) \cos(\gamma) + \cos(\delta) \cos(\phi) \cos(\beta) \cos(\omega) \\ & + \cos(\delta) \sin(\phi) \sin(\beta) \cos(\gamma) \cos(\omega) + \cos(\delta) \sin(\beta) \sin(\gamma) \sin(\omega) \end{aligned} \quad (D.2.3)$$

or

$$\cos(\theta_b) = \cos(SZA) \cos(\beta) + \sin(SZA) \sin(\beta) \cos(SAA - \gamma) \quad (D.2.4)$$

with β and γ the inclination and azimuth angle of the module, (in general, the module is South-facing in the Northern hemisphere to maximize sun exposure), SZA and SAA the solar zenith and azimuth angles, δ the solar declination, ϕ the latitude and ω the hour angle, as illustrated in Figure D.2.5

D.2.2.2 Ground-reflected irradiance

The ground-reflected radiation is computed thanks to the contribution of the direct and diffuse radiation given the surface albedo ρ :

$$G_\rho = \rho_b G_b + \rho_d G_d \quad (D.2.5)$$

The ground-reflected radiation is most commonly modelled assuming isotropic reflectance, meaning that it is evenly distributed over all directions, leading to (*Reindl et al. 1990a*, *Loutzenhiser et al. 2007*, *Duffie & Beckman 2013*):

$$G_{\rho, \text{POA}} = \frac{1 - \cos(\beta)}{2} \cdot G_{\rho} \quad (\text{D.2.6})$$

under 2D isotropic assumption.

Certain researchers have developed anisotropic ground reflectance models, but these have never been validated due to the lack of experimental data (*Reindl et al. 1990a*). The models presented in the following for the diffuse component always consider isotropic ground-reflectance.

D.2.2.3 Sky-scattered (or diffuse) irradiance

The diffuse component is difficult to model as it depends on the position of the sun, and consequently on space and time. It is generally modelled by considering three subcomponents (*Reindl et al. 1990a*, *Loutzenhiser et al. 2007*) as illustrated in Figure D.2.6:

- a circumsolar diffuse subcomponent, which is due to the predominant forward scattering of solar radiation in the atmosphere by the aerosols;
- a horizon brightening subcomponent, which translates a higher diffuse radiation near the horizon due to an increase in radiation scattering and multiple internal reflection for long path lengths through the atmosphere;
- an isotropic diffuse subcomponent, which corresponds to the remaining irradiance and is assumed to be uniformly distributed over the sky dome.

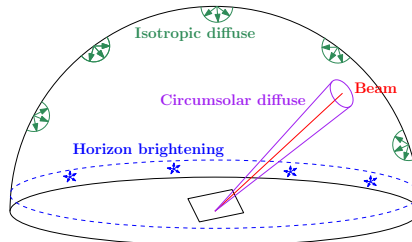


Figure D.2.6: Different subcomponents of the sky-scattered irradiance

The diffuse radiation on a tilted surface can be estimated by many transposition models, six of which are considered in the following. In all six of these models, the beam and ground-reflected components are treated as presented here-above (unless specified otherwise) but do not all consider the three diffuse subcomponents. These models are presented in order of complexity:

- Isotropic (2D) model is the simplest model, it assumes that all the diffuse radiation is uniformly distributed over the sky dome and all sky elements are only defined by the zenith angle. In this 2D approach, the azimuth angle is therefore not taken into account.
- Isotropic 3D model also assumes isotropic radiation but both azimuth and zenith angle of the radiance are considered contrary to the 2D model. With this model, the ground-reflected irradiance is also assumed 3D isotropic;

- Klucher model aims at correcting the errors in overcast skies under the isotropic model by adding a clearness index (*Klucher 1979*);
- Hay-Davies model also accounts for the circumsolar subcomponent (*Davies & Hay 1980*);
- Reindl model takes into account all isotropic diffuse, circumsolar radiation and horizontal brightening (*Reindl et al. 1990a*);
- Perez model considers empirically derived coefficients, as derived in *Perez et al. (1987, 1990)*, aiming at better modelling all three subcomponents. Only the coefficients provided in *Perez et al. (1990)* will be considered in the following.

D.2.2.4 Formulation of the different diffuse transposition models

Isotropic 2D model The isotropic model is the simplest model as it assumes that all the diffuse radiation is uniformly distributed over the sky dome (*Duffie & Beckman 2013*):

$$G_{d,POA} = \frac{1 + \cos(\beta)}{2} \cdot G_d \quad (\text{D.2.7})$$

leading to :

$$G_{POA, \text{isotropic}} = \frac{\cos(\theta)}{\cos(SZA)} \cdot G_b + \frac{1 + \cos(\beta)}{2} \cdot G_d + \frac{1 - \cos(\beta)}{2} \cdot G_\rho \quad (\text{D.2.8})$$

The expression $G_{d,POA}$ is theoretically derived in Appendix [D.2.2.5](#)

Isotropic 3D model In the 2D isotropic model, the azimuth angle of the radiance is neglected. In a 3D isotropic model, the azimuth angle of the radiance is taken into account, yielding (*Badescu 2002*)

$$G_{d,POA} = \frac{3 + \cos(2\beta)}{4} G_d \quad (\text{D.2.9})$$

and

$$G_{\rho,POA} = \frac{1 - \cos(2\beta)}{4} G_\rho \quad (\text{D.2.10})$$

which are derived in Appendix [D.2.2.5](#).

The global POA irradiance is then computed thanks to :

$$G_{POA, \text{isotropic3D}} = \frac{\cos(\theta)}{\cos(SZA)} \cdot G_b + \frac{3 + \cos(2\beta)}{4} \cdot G_d + \frac{1 - \cos(2\beta)}{4} \cdot G_\rho \quad (\text{D.2.11})$$

Klucher model *Klucher (1979)* found that the isotropic model provides a good estimation under overcast skies but underestimates the irradiance on a tilted surface under clear and partly cloudy conditions. *Klucher (1979)* thus developed the following model:

$$G_{d,POA0} = \frac{1 + \cos(\beta)}{2} \cdot \left[1 + F' \sin^3 \left(\frac{\beta}{2} \right) \right] \cdot [1 + F' \cos^2(\theta) \sin^3(SZA)] \cdot G_d \quad (\text{D.2.12})$$

with F' a clearness index defined by :

$$F' \equiv 1 - \left(\frac{G_d}{GHI} \right)^2 \quad (\text{D.2.13})$$

Hay-Davies model The Hay-Davies model takes into account the circumsolar subcomponent in the diffuse term. It uses the anisotropy index A' as defined in (D.2.14):

$$A' \equiv \frac{\text{DNI}}{G_{\text{extra}}} = \frac{G_b}{\cos(\text{SZA}) \times G_{\text{extra}}} \quad (\text{D.2.14})$$

with G_{extra} the direct extraterrestrial normal irradiance. This anisotropy index quantifies the fraction of diffuse irradiance to be treated as circumsolar, the remaining being considered isotropic diffuse (*Davies & Hay 1980*):

$$G_{d,\text{POA}} = \left[A' \cdot \frac{\cos(\theta)}{\cos(\text{SZA})} + (1 - A') \frac{1 + \cos(\beta)}{2} \right] \cdot G_d \quad (\text{D.2.15})$$

Under clear skies, the anisotropic index will be high thus increasing the weight of the circumsolar diffuse whereas under cloudy sky, the diffuse goes towards being all treated as isotropic.

Reindl model The Reindl model accounts for all isotropic diffuse, circumsolar radiation and horizontal brightening. Using the same definition of the anisotropy index A' as in (D.2.14), the diffuse component with *Reindl et al. (1990a)* is :

$$G_{d,\text{POA}} = \left[A' \cdot \frac{\cos(\theta)}{\cos(\text{SZA})} + (1 - A') \frac{1 + \cos(\beta)}{2} \cdot \left[1 + \sqrt{\frac{G_b}{\text{GHI}}} \sin^3 \left(\frac{\beta}{2} \right) \right] \right] \cdot G_d \quad (\text{D.2.16})$$

Perez model Perez models represent in more details all three subcomponents by using empirically derived coefficients.

Following *Perez et al. (1987, 1990)*, the diffuse component can be computed thanks to :

$$G_{d,\text{POA}} = \left[(1 - F_1) \cdot \left(\frac{1 + \cos(\beta)}{2} \right) + F_1 \frac{a}{b} + F_2 \sin(\beta) \right] \cdot G_d \quad (\text{D.2.17})$$

a and b are computed by :

$$a = \max(0^\circ, \cos(\theta)) \quad (\text{D.2.18})$$

and

$$b = \max(\cos(85^\circ), \cos(\theta)) \quad (\text{D.2.19})$$

F_1 and F_2 are the circumsolar and horizon brightening coefficients and depend on the insulation conditions. These conditions are parametrized by SZA, the brightness of the sky dome Δ , and its clearness ϵ , defined by (*Perez et al. 1987, 1990*):

$$\epsilon \equiv \frac{\frac{G_d + \text{GNI}}{G_d} + 1.041 \cdot \text{SZA}^3}{1 + 1.041 \cdot \text{SZA}^3} \quad (\text{D.2.20})$$

and

$$\Delta \equiv \text{AM} \cdot \frac{G_d}{G_{\text{extra}}}. \quad (\text{D.2.21})$$

ϵ variations express the transition from a totally overcast sky ($\epsilon = 1$) to a low turbidity clear sky ($\epsilon > 6.2$) whereas Δ variations reflect the opacity/thickness of the clouds.

The brightness coefficients are then computed thanks to empirical coefficients $f_{ij}, i \in 1, 2, j \in 1, 2, 3$.

Table D.2.1: Discrete sky clearness categories (*Perez et al. 1990*)

ϵ category	Lower bound	Upper bound
1. Overcast	1	1.065
2.	1.065	1.230
3.	1.230	1.500
4.	1.500	1.950
5.	1.950	2.800
6.	2.800	4.500
7.	4.500	6.200
8. Clear	6.200	∞

$$F_1 = \max(0, f_{11} + f_{12}\Delta + f_{13}\text{SZA}) \quad (\text{D.2.22})$$

$$F_1 = f_{21} + f_{22}\Delta + f_{23}\text{SZA} \quad (\text{D.2.23})$$

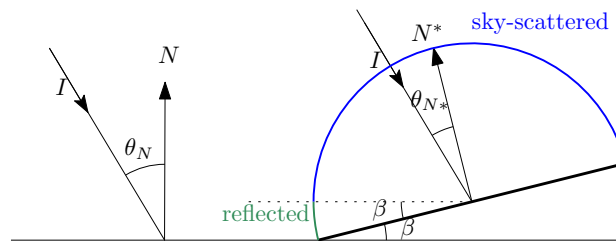
The empirical coefficients are based on two years of data from Carpentras and Trappes in France (*Perez et al. 1987*) or on data collected from 13 sites (10 U.S. locations as well as Geneva, Trappes and Carpentras) (*Perez et al. 1990*). These coefficients are given for each ϵ category as defined in Table D.2.1. *Perez et al. (1990)* conclude that the choice of the coefficients set is not critical such that only (*Perez et al. 1990*) model will be considered in this project.

Table D.2.2: Empirical values f_{ij} depending on the clearness category defined Table D.2.1 found in *Perez et al. (1990)*

ϵ category	f_{11}	f_{12}	f_{13}	f_{21}	f_{22}	f_{23}
1	-0.008	0.588	-0.062	-0.06	0.072	-0.022
2	0.13	0.683	-0.151	-0.019	0.066	-0.029
3	0.33	0.487	-0.221	0.055	-0.064	-0.026
4	0.568	0.187	-0.295	0.109	-0.152	-0.014
5	0.873	-0.392	-0.362	0.226	-0.462	0.001
6	1.132	-1.237	-0.412	0.288	-0.823	0.056
7	1.06	-1.6	-0.359	0.264	-1.127	0.131
8	0.678	-0.327	-0.25	0.156	-1.377	0.251

D.2.2.5 Deriving the 2D and 3D isotropic transposition models

In the following, the radiance (or intensity, in $\text{W m}^{-2} \text{sr}^{-1}$) is denoted by I . The subscripts d and ρ refer to diffuse and ground-reflected components. N and N^* correspond to the normal to the horizontal plane and to the tilted surface. The notations used in the following are illustrated in Figure D.2.7.


Figure D.2.7: Notations used for deriving the 2D and 3D isotropic diffusion formulation, adapted from *Badescu (2002)*.

2D isotropic model In the 2D isotropic model, the azimuth angle of the radiance is neglected. As the radiance is assumed isotropic, $I_d(\theta) = I_d$. One has:

$$G_d = \int_{-\frac{\pi}{2}}^{\frac{\pi}{2}} I_d \cos(\theta_N) d\theta_N = 2I_d \quad (\text{D.2.24})$$

and

$$G_{d,POA} = \int_{-\frac{\pi}{2}}^{\frac{\pi}{2}-\beta} I_d \cos(\theta_{N^*}) d\theta_{N^*} = (\cos(\beta) + 1) \cdot I_d \quad (\text{D.2.25})$$

yielding:

$$G_{d,POA} = \frac{1 + \cos(\beta)}{2} G_d \quad (\text{D.2.26})$$

Similarly, for the ground-reflected irradiance ($I_\rho(\theta) = I_\rho$):

$$G_\rho = \int_{-\frac{\pi}{2}}^{\frac{\pi}{2}} I_\rho \cos(\theta_N) d\theta_N = 2I_\rho \quad (\text{D.2.27})$$

and

$$G_{\rho,POA} = \int_{\frac{\pi}{2}-\beta}^{\frac{\pi}{2}} I_\rho \cos(\theta_{N^*}) d\theta_{N^*} = (1 - \cos(\beta)) \cdot I_\rho \quad (\text{D.2.28})$$

yielding:

$$G_{\rho,POA} = \frac{1 - \cos(\beta)}{2} G_\rho \quad (\text{D.2.29})$$

3D isotropic model In a 3D isotropic model, the azimuth angle of the radiance is taken into account, but one still has $I_\rho(\theta, \phi) = I_\rho$ and $I_d(\theta, \phi) = I_d$ thanks to the isotropic hypothesis.

For the sky-scattered irradiance, one gets :

$$\begin{aligned} G_d &= \int_0^{2\pi} \int_{-\frac{\pi}{2}}^{\frac{\pi}{2}} I_d \cos(\theta_N) \sin(\theta_N) d\theta_N d\phi \\ &= \int_0^{2\pi} d\phi \int_0^{\frac{\pi}{2}} I_d \frac{\sin(2\theta_N)}{2} d\theta_N \\ &= \pi I_d \end{aligned} \quad (\text{D.2.30})$$

and

$$\begin{aligned} G_{d,POA} &= \int_{\gamma-\frac{\pi}{2}}^{\gamma+\frac{\pi}{2}} d\phi \int_0^{\frac{\pi}{2}} I_d \cos(\theta_N) \sin(\theta_N) d\theta_N + \int_{\gamma+\frac{\pi}{2}}^{\gamma+\frac{3\pi}{2}} d\phi \int_0^{\frac{\pi}{2}-\beta} I_d \cos(\theta_N) \sin(\theta_N) d\theta_N \\ &= \int_{\gamma-\frac{\pi}{2}}^{\gamma+\frac{\pi}{2}} d\phi \int_0^{\frac{\pi}{2}} I_d \frac{\sin(2\theta_N)}{2} d\theta_N + \int_{\gamma+\frac{\pi}{2}}^{\gamma+\frac{3\pi}{2}} d\phi \int_0^{\frac{\pi}{2}-\beta} I_d \frac{\sin(2\theta_N)}{2} d\theta_N \\ &= \frac{\pi \times (\cos(2\beta) + 3)}{4} \cdot I_d \end{aligned} \quad (\text{D.2.31})$$

yielding:

$$G_{d,POA} = \frac{3 + \cos(2\beta)}{4} G_d \quad (\text{D.2.32})$$

Similarly, for the ground-reflected irradiance:

$$\begin{aligned} G_\rho &= \int_0^{2\pi} d\phi \int_0^{\frac{\pi}{2}} I_\rho \cos(\theta_N) \sin(\theta_N) d\theta_N \\ &= \pi I_\rho \end{aligned} \quad (\text{D.2.33})$$

and

$$\begin{aligned} G_{\rho,POA} &= \int_{\gamma-\frac{\pi}{2}}^{\gamma+\frac{\pi}{2}} d\phi \int_{\frac{\pi}{2}-\beta}^{\frac{\pi}{2}} I_\rho \cos(\theta_{N^*}) \sin(\theta_{N^*}) d\theta_{N^*} \\ &= \pi \frac{1 - \cos(2\beta)}{4} \cdot I_\rho \end{aligned} \quad (\text{D.2.34})$$

yielding:

$$G_{\rho,POA} = \frac{1 - \cos(2\beta)}{4} G_\rho \quad (\text{D.2.35})$$

D.2.2.6 Expected accuracies according to a literature review

Transposition models have been widely investigated in the past. The conclusions of two different studies are presented here.

Loutzenhiser et al. (2007) compares different transposition models with four building energy simulation codes and two 25 day periods in October and March/April, which allow to account for diverse atmospheric conditions and solar altitudes. The mean absolute differences for both periods were found to be: 13.7% and 14.9% for the isotropic sky model, 9.1% for the Hay–Davies model, 9.4% for the Reindl model, 13.2% for the Klucher model, between 6.6% and 9.0% for the different 1990 Perez models, and 7.9% for the 1987 Perez model. The isotropic sky model is found to provide the worst results and the Perez model performs the best in the studied case.

Pelland et al. (2013) explores PV forecast accuracy. The accuracy in rated power with Perez, isotropic, Hay-Davies and Reindl models are assessed. *Pelland et al. (2013)* concludes that the isotropic model has the highest mean absolute error but the smallest mean bias error. The other models have similar performances.

D.2.3 Optical losses

Optical losses must be modelled as they explain an increased loss in power at high angles-of-incidence. The optical losses take into account two phenomena:

1. the losses due to the absorption of each layer;
2. the losses due to reflection at each interface.

These two phenomena are taken into account by the transmission-absorption coefficient of a layer denoted by $\tau\alpha$:

$$\tau\alpha(\theta_r, \lambda) = A_\alpha(\theta_r, \lambda) \cdot T_\tau(\theta_r, \lambda) \quad (\text{D.2.36})$$

with A_α the absorption of the layer and T_τ the transmission coefficient at the interface.

D.2.3.1 Absorption : Beer–Bouguer–Lambert law

The absorption coefficient of a layer follows Beer–Bouguer–Lambert law:

$$A_\alpha(\theta_r, \lambda) = \exp\left(-\frac{K(\lambda)L}{\cos(\theta_r)}\right) \quad (\text{D.2.37})$$

with K the extinction coefficient of the medium (wavelength dependent), L the thickness of the layer, θ_r the angle of refraction (as illustrated in Figure D.2.8).

D.2.3.2 Transmission, reflection and refraction

Reflectance and transmission at an interface can be computed thanks to Fresnel equations (Figure D.2.8):

$$R_{\parallel} = \frac{\tan^2(\theta_i - \theta_r)}{\tan^2(\theta_i + \theta_r)} \quad (\text{D.2.38})$$

$$R_{\perp} = \frac{\sin^2(\theta_i - \theta_r)}{\sin^2(\theta_i + \theta_r)} \quad (\text{D.2.39})$$

$$T_{\parallel} = 1 - R_{\parallel} \quad (\text{D.2.40})$$

$$T_{\perp} = 1 - R_{\perp} \quad (\text{D.2.41})$$

with θ_i the incident angle (Figure D.2.8).

Assuming unpolarized light, the transmission coefficient can be computed thanks to

$$T_\tau = \frac{T_{\parallel} + T_{\perp}}{2} \quad (\text{D.2.42})$$

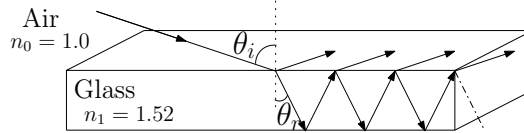


Figure D.2.8: Angles of incidence and refraction, adapted from *Krauter & Hanitsch (1996)*

The angle of refraction θ_r is given by Snell’s law

$$\theta_r = \arcsin\left(\frac{n_0}{n_1} \sin(\theta_i)\right) \quad (\text{D.2.43})$$

with n_0, n_1 the index of refraction of the two media (Figure D.2.8).

In reality, the PV module has several layers before the solar cells, each inducing reflection, refraction and absorption as illustrated in Figure D.2.9 implying iterating the previous expressions on all layers.

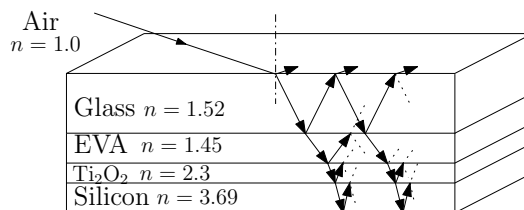


Figure D.2.9: Angles of incidence and refraction in a “three slab optical system” of a Si solar cell – ARC (TiO_2) = anti-reflective-coating, EVA = ethylene-vinyl-acetate, adapted from *Krauter & Hanitsch (1996)*

Transmission and reflection coefficients also theoretically depend on the wavelength. *Sjerps-Koomen et al. (1996)* computed the transmission coefficient for a range of angles of incidence at the most impacting wavelength for a Si solar cell (over 400–1200 nm). Figure D.2.10 illustrates the results, showing that the wavelength does not have a major influence on the transmittance coefficient. The optical losses applied in this photovoltaic model are assumed not to depend on the wavelength.

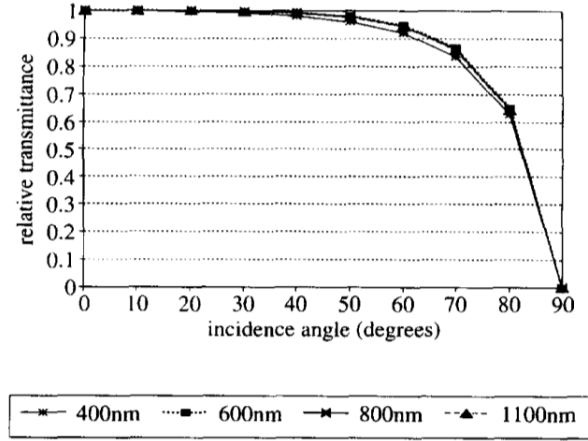


Figure D.2.10: Transmission coefficients relative to STC as a function of angle of incidence for different wavelengths, (*Sjerps-Koomen et al. 1996*)

D.2.3.3 Optical losses models

Based on Fresnel’s law The iteration of Fresnel and Snell laws enables to compute the reflection and refraction through all the layers. However, *Sjerps-Koomen et al. (1996)* shows that the transmission through the different layers of a PV module is well represented by a simple air-glass model (Figure D.2.11). The *Sjerps-Koomen et al. (1996)* model can easily be deduce from equations (D.2.38) – (D.2.42):

$$T = 1 - \frac{1}{2} \left(\frac{\sin^2(\theta_i - \theta_r)}{\sin^2(\theta_i + \theta_r)} + \frac{\tan^2(\theta_i - \theta_r)}{\tan^2(\theta_i + \theta_r)} \right) \quad (\text{D.2.44})$$

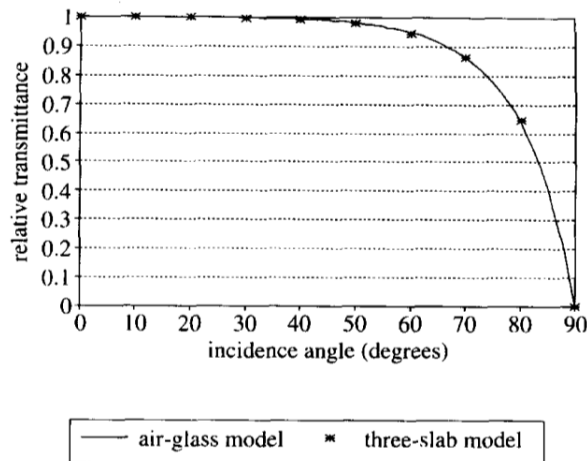


Figure D.2.11: Transmission coefficient relative to STC as a function of the angle of incidence for the simple air-glass and more complex “three-slab-layer” models, (*Sjerps-Koomen et al. 1996*)

De Soto et al. (2006) considers one simple air-glass model following *Sjerps-Koomen et al. (1996)* suggestion but considers nevertheless the absorption in the glass layer :

$$T = \exp\left(-\frac{KL}{\cos(\theta_r)}\right) \left[1 - \frac{1}{2} \left(\frac{\sin^2(\theta_i - \theta_r)}{\sin^2(\theta_i + \theta_r)} + \frac{\tan^2(\theta_i - \theta_r)}{\tan^2(\theta_i + \theta_r)}\right)\right] \quad (\text{D.2.45})$$

assuming unpolarized irradiance. *De Soto et al. (2006)* also applies the glazing extinction coefficient $K = 4 \text{ m}^{-1}$ of water white glass, the glazing thickness $L = 2 \text{ mm}$ and a refractive index of 1.526 for glass, which *De Soto et al. (2006)* considers as reasonable values for most PV modules.

ASHRAE models Another common model is the ASHRAE model (American Society of Heating, Refrigerating and Air-Conditioning Engineers):

$$\tau_{rel}(\theta) = 1 - b_0 \left(\frac{1}{\cos(\theta)} - 1\right) \quad (\text{D.2.46})$$

where with $b_0 = 0.05$ or $b_0 = 1$ for PV modules (*Schaub et al. 1994*).

Sjerps-Koomen et al. (1996) shows that the ASHRAE models with b_0 equal to 0.05 or 1 envelops the results with the simple “air-glass” model, thus advising to use the physical model. The ASHRAE method has therefore not been implemented in the photovoltaic model.

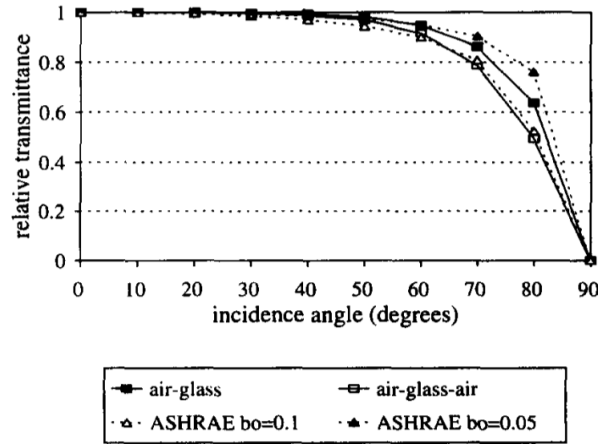


Figure D.2.12: Coefficient de transmission relatif aux STC (standard test conditions) en fonction de l’angle d’incidence selon différentes méthodes, (*Sjerps-Koomen et al. 1996*)

Martin and Ruiz models *Martin & Ruiz (2001)* derives angular losses (AL) for direct, diffuse and ground-reflected radiation neglecting absorption as the losses due to absorption as assumed to vary similarly to transmittance with the angle of incidence:

– for direct radiation :

$$AL_B(\theta) = 1 - \frac{\exp\left(-\frac{\cos(\theta)}{a_r}\right) - \exp\left(-\frac{1}{a_r}\right)}{1 - \exp\left(-\frac{1}{a_r}\right)} \quad (\text{D.2.47})$$

– for the radiation scattered by the sky:

$$AL_D(\beta) = 1 - \exp \left[-\frac{1}{a_r} \left[c_1 \left(\sin(\beta) + \frac{\pi - \beta - \sin(\beta)}{1 + \cos(\beta)} \right) + c_2 \left(\sin(\beta) + \frac{\pi - \beta - \sin(\beta)}{1 + \cos(\beta)} \right)^2 \right] \right] \quad (\text{D.2.48})$$

– for the radiation reflected by the ground :

$$AL_\rho(\beta) = 1 - \exp \left[-\frac{1}{a_r} \left[c_1 \left(\sin(\beta) + \frac{\beta - \sin(\beta)}{1 - \cos(\beta)} \right) + c_2 \left(\sin(\beta) + \frac{\beta - \sin(\beta)}{1 - \cos(\beta)} \right)^2 \right] \right] \quad (\text{D.2.49})$$

with $c_1 = \frac{4}{3\pi}$ and c_2 linearly depending on a_r . The a_r , c_1 and c_2 coefficients are fitted parameter to experimental data (and are tabuled in *Martin & Ruiz (2001)*).

D.2.3.4 Angle of incidence

Fresnel's theory uses the angle of incidence of the incoming radiation. The angle of incidence for the beam irradiance θ_b is perfectly defined and can be derived thanks to (D.2.3). However, the sky-scattered and ground-reflected irradiances do not have a single incident angle but are distributed over a range of incident angles. The aim is therefore to define an effective (or beam equivalent) incidence angle.

The transmittance of sky-scattered and ground-reflected irradiances are defined by the integration over the range of solid angle :

$$\tau_x = \frac{\int \tau_b(\theta) I_x \cos(\theta) \sin(\theta) d\theta d\phi}{\int I_x \cos(\theta) \sin(\theta) d\theta d\phi} \quad (\text{D.2.50})$$

with τ_b the transmittance for beam radiation and x representing the sky-scattered or ground-reflected irradiances.

Assuming the sky-scattered and ground-reflected irradiances are isotropic, *Brandemuehl & Beckman (1980)* solves the integral in (D.2.50) numerically for both irradiances for different glazing systems and inclination angles. *Brandemuehl & Beckman (1980)* then defines the “effective beam radiation incidence angle” for diffused (θ_d) and ground-reflected (θ_ρ) irradiance as the angles such that $\tau_d = \tau_b(\theta_d)$ and $\tau_\rho = \tau_b(\theta_\rho)$. Figure D.2.13 shows the effective beam radiation incidence angle for a range of inclination angles and glazing systems.

Brandemuehl & Beckman (1980) derives by least-square-curve-fits the following approximations for the ground-reflected radiation effective angle :

$$\theta_\rho = 90 - 0.5788\beta + 0.002693\beta^2 \quad (\text{D.2.51})$$

and the sky-scattered radiation effective angle :

$$\theta_d = 59.68 - 0.1388\beta + 0.001497\beta^2 \quad (\text{D.2.52})$$

with the inclination angle β in degrees. These approximations are valid for one or two cover glazing systems with $1.34 < n < 1.526$ and extinction lengths smaller than 0.0524 which are criteria generally met for common panels.

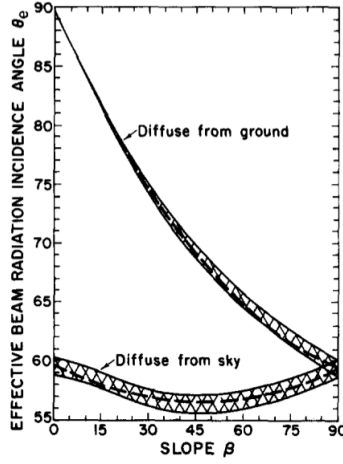


Figure D.2.13: Effective beam radiation incidence angle of sky-scattered and ground-reflected irradiances on a tilted surface, (*Brandemuehl & Beckman 1980*). The banded region corresponds to all simulations with one or two cover glazing systems with $1.34 < n < 1.526$ and extinction lengths smaller than 0.0524

D.2.3.5 Considered optical models in the PV model

Four optical models are therefore considered,

- two theoretically derived from optical laws :
 - “Air-glass reflection and absorption” (as in *De Soto et al. (2006)*)
 - “Air-glass reflection” (as advised by *Sjerps-Koomen et al. (1996)*)
- two models based on empirical values for $a_r = 0.157$ (Air/Glass/Si) and $a_r = 0.17$ (typical value for m-Si modules with clean surfaces) in *Martin & Ruiz (2001)*

Martin & Ruiz (2001) distinguishes the different components (beam, scattered, ground-reflected) whereas the two other models provide a method to compute the transmitted irradiance as a function of the angle of incidence. These two methods are therefore applied with the angle-of-incidence of the beam irradiance, and the effective beam irradiance incidence angle of diffuse and ground-reflected irradiance as defined by *Brandemuehl & Beckman (1980)* and presented above.

Furthermore, the reflection and reflection-absorption models based on Fresnel are not defined for $\theta = 0^\circ$ as the denominators of the sine and tan functions equal zero. One can however set the reflection values to their limit for $\theta = 0^\circ$:

$$R_{\parallel}(\theta = 0) = \frac{\left(1 - \frac{n_0}{n_1}\right)^2}{\left(1 + \frac{n_0}{n_1}\right)^2} \quad (\text{D.2.53})$$

$$R_{\perp}(\theta = 0) = \frac{\left(1 - \frac{n_0}{n_1}\right)^2}{\left(1 + \frac{n_0}{n_1}\right)^2} \quad (\text{D.2.54})$$

such that $T_r = 1 - \frac{\left(1 - \frac{n_0}{n_1}\right)^2}{\left(1 + \frac{n_0}{n_1}\right)^2}$ under unpolarised hypothesis.

D.3 Cell temperature

D.3.1 A simplified approach to steady-state energy balance

The steady-state energy balance indicates that the PV electrical power equals the difference between the absorbed and dissipated power. In other terms (*Skoplaki et al. 2008*):

$$\eta_c G_{POA} = (\tau\alpha)G_{POA} - U_L(T_c - T_a) \quad (\text{D.3.1})$$

with η_c the cell efficiency, $\tau\alpha$ the transmission-absorption coefficient and U_L the thermal loss coefficient. Considering the NTE/NOCT conditions, the thermal loss coefficient equals

$$U_{L,NOCT} = \frac{(\tau\alpha)G_{NOCT}}{NOCT - T_{a,NOCT}} \quad (\text{D.3.2})$$

and with (D.3.1), one gets:

$$T_c = T_a + \frac{G_{POA}}{G_{NOCT}} \cdot (NOCT - T_{a,NOCT}) \cdot \frac{U_{L,NOCT}}{U_L} \left[1 - \frac{\eta_c}{\tau\alpha} \right] \quad (\text{D.3.3})$$

with the cell electrical efficiency denoted by η_c which can be deduced by $\eta_c = \frac{P_{MPP,STC}}{1000 \text{ W m}^{-2}}$, τ the transmittance of the glazing, α the solar absorptance of the PV layer, and U_L the thermal loss coefficient.

The definition of $C_{T,P_{MPP}}$ yields ¹:

$$\eta_c \approx \eta_{c,STC} (1 + C_{T,P_{MPP}}(T_c - T_{c,STC})) \quad (\text{D.3.4})$$

The previous equation neglects the influence of the solar radiation on the cell efficiency, which is often assumed (*Evans 1981*).

(D.3.3) and (D.3.4) give ²:

$$T_c = \frac{T_a + \frac{G_{POA}}{G_{NOCT}} \cdot (NOCT - T_{a,NOCT}) \cdot \frac{U_{L,NOCT}}{U_L} \left[1 - \frac{\eta_{STC}}{\tau\alpha} (1 - C_{T,P_{MPP}} T_{c,STC}) \right]}{1 - \frac{G_{POA}}{G_{NOCT}} \cdot (NOCT - T_{a,NOCT}) \cdot \frac{U_{L,NOCT}}{U_L} \cdot \frac{\eta_{STC} C_{T,P_{MPP}}}{\tau\alpha}} \quad (\text{D.3.5})$$

thus providing a theoretical approach to the cell temperature, but requiring the knowledge of several unknown parameters such as U_L .

D.3.2 Considered temperature models

Three models to compute the cell temperature are studied :

- a “simple model”, which only considers the cell temperature dependence on ambient temperature and POA irradiance :

$$T_c = T_a + \frac{G_{POA}}{G_{NOCT}} \cdot (NOCT - T_{a,NOCT}) \quad (\text{D.3.6})$$

- *King et al. (2004)* model, which first computes the module temperature from the ambient temperature, POA irradiance and wind speed thanks to empirically fitted coefficients tab-

¹We consider here $C_{T,P_{MPP}}$ the algebraic value, whereas in *Skoplaki et al. (2008)*, $\beta_{ref} = |C_{T,P_{MPP}}|$ thus leading to a change in sign before the temperature coefficient of the maximum power in the cell efficiency equation

²Be careful to the change in sign, idem as previous footnote

ulated in *King et al. (2004)* then applying an empirically defined temperature difference to deduce the cell temperature;

- *Skoplaki et al. (2008)* model, which is based on the energy balance presented above and hypothesis on the thermal loss coefficient U_L .

A model including the effect of wind is preferable since the cooling effect of wind can change the module performance by over 5% in hot windy areas (*Huld & Amillo 2015*).

D.3.3 Detailed temperature models

Simple model The simplest model consists in considering only the cell temperature dependence on ambient temperature and POA irradiance:

$$T_c = T_a + k \times G_{POA} \quad (\text{D.3.7})$$

with k , known as the Ross parameter, expressing the rise in temperature with the incident solar flux. This linear model requires an estimation of k which is not straightforward before the installation. However, certain tabulated values exist in the literature (*Skoplaki et al. 2008*).

A similar equation can be derived from (D.3.3) by assuming a constant U_L and knowing that $\frac{\eta_c}{\tau\alpha} \ll 1$:

$$T_c = T_a + \frac{G_{POA}}{G_{NOCT}} \times (NOCT - T_{a,NOCT}) \quad (\text{D.3.8})$$

Skoplaki model The thermal loss coefficient U_L takes into account three heat transfer coefficients:

1. radiation;
2. free convection;
3. forced (wind) convection.

According to *Skoplaki et al. (2008)*, radiation and free convection only have a minor effect on the cell temperature computed thanks to (D.3.5). The thermal loss coefficient can be approximated by the forced wind convection h_w :

$$U_L \approx h_w \quad (\text{D.3.9})$$

Considering also that the second denominator term in (D.3.5) is small compared to one, *Skoplaki et al. (2008)* derives a new cell temperature model:

$$T_c = T_a + \frac{G_{POA}}{G_{NOCT}} \cdot (NOCT - T_{a,NOCT}) \cdot \frac{h_{w,NOCT}}{h_w} \left[1 - \frac{\eta_{STC}}{\tau\alpha} (1 - C_{T,P_{MPP}} T_{STC}) \right] \quad (\text{D.3.10})$$

with $\tau\alpha \approx 0.9$.

The forced wind convection can be computed thanks to *Skoplaki et al. (2008)*:

- the free stream wind speed in the windward side of the PV module V_f (Skoplaki model 1):

$$h_w = 8.91 + 2.0V_f \quad (\text{D.3.11})$$

– the local wind speed V_w , following Nusselt-Jürges relation (Skoplaki model 2):

$$h_w = 5.7 + 3.8V_w \quad (\text{D.3.12})$$

The previous formulation is in theory limited to free-standing arrays. Similarly to the Ross parameter k , *Skoplaki et al. (2008)* also introduces a mounting coefficient ω , which is defined as the ratio of the Ross parameter to the free-standing Ross parameter in an alternative formulation of the cell temperature for other mountings:

$$T_c = T_a + \omega \times \frac{G_{POA}}{G_{NOCT}} \cdot (NOCT - T_{a,NOCT}) \cdot \frac{h_{w,NOCT}}{h_w} \left[1 - \frac{\eta_{STC}}{\tau\alpha} (1 - C_{T,PMP} T_{STC}) \right] \quad (\text{D.3.13})$$

Four different approaches are therefore considered for the Skoplaki model in the PV model:

1. Skoplaki model 1, where the measured wind speed is considered being equal to the free stream wind speed in the windward side of the PV module V_f (following equations (D.3.10) and (D.3.11));
2. Skoplaki model 2, where the measured wind speed is considered being equal to the local wind speed V_w (following equations (D.3.10) and (D.3.12));
3. Skoplaki model 2, but by considering a “standard” cell efficiency based on p-Si technology and the definition of NOCT (*Skoplaki et al. 2008*) (“Skoplaki 2 constant”):

$$T_c = T_a + \frac{0.25}{h_w} G_{POA} = T_a + \frac{0.25}{5.7 + 3.8V_w} G_{POA} \quad (\text{D.3.14})$$

4. Skoplaki model 2 without neglecting the irradiance intensity in the cell efficiency (“Skoplaki 2 irradiance”):

$$T_c = T_a + \frac{G_{POA}}{G_{NOCT}} \cdot (NOCT - T_{a,NOCT}) \cdot \frac{5.7 + 3.8V_{w,NOCT}}{5.7 + 3.8V_w} \left[1 - \frac{\eta_{STC}}{\tau\alpha} (1 - C_{T,PMP} T_{STC} + \gamma \log_{10}(G_{POA})) \right] \quad (\text{D.3.15})$$

with $\gamma \approx 0.12$ the intensity coefficient of cell efficiency (*Skoplaki et al. 2008*).

King model *King et al. (2004)* use another approach, by deducing the cell temperature from the module temperature following:

$$T_c = T_{\text{mod}} + \frac{G_{POA}}{G_{\text{ref}}} \times \Delta T \quad (\text{D.3.16})$$

where ΔT for $G_{\text{ref}} = 1000 \text{ W m}^{-2}$ is tabulated (Table D.3.1).

The module temperature is then modelled by (*King et al. 2004*):

$$T_{\text{mod}} = G_{POA} \exp(a + b \times WS_{10m}) + T_a \quad (\text{D.3.17})$$

with a and b two empirically defined parameters which are tabulated depending on the module-type and the mount (Table D.3.1), and WS_{10m} the wind speed at the standard meteorological height of 10m height.

The cell temperature is generally different to the module temperature by typically 2 to 3 °C for flat-plate modules in an open-rack mount but with a thermally insulated back surface, this

temperature difference can be neglected, (*King et al. 2004*).

Table D.3.1: Empirically determined a , b and ΔT coefficients for given module-types and mounts, (*King et al. 2004*)

Module-type	Mount	a	b	ΔT (°C)
Glass/cell/glass	Open rack	-3.47	-0.594	3
Glass/cell/glass	Close roof mount	-2.98	-0.0471	1
Glass/cell/polymer sheet	Open rack	-3.56	-0.075	3
Glass/cell/polymer sheet	Insulated back	-2.81	-0.0455	0
Polymer/thin-film/steel	Open rack	-3.58	-0.113	3
22X Linear Concentrator	Tracker	-3.23	-0.13	13

D.4 Spectral response and cell photocurrent in STC conditions

As a reminder, the quantum efficiency with an ideal approach is defined by (2.2.16), whereas the spectral response is derived from (2.2.18)

D.4.0.1 Modelled quantum efficiency and spectral response

As explained in Part 2.2.7 and illustrated in Figure D.4.1, the quantum efficiency is far from being ideal.

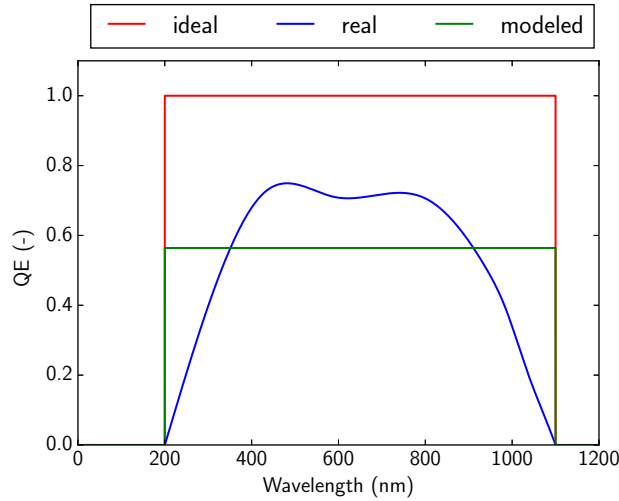


Figure D.4.1: Ideal, real and modelled quantum efficiency of a solar cell.

Without any further information on the shape of the QE curve, the quantum efficiency can be modelled with a constant value:

$$QE_{modeled}(\lambda) = \alpha \times \mathbb{1}_{\lambda < \lambda_{gap}} \quad (\text{D.4.1})$$

meaning

$$SR_{modeled}(\lambda) = \alpha \times SR_{ideal}(\lambda) \quad (\text{D.4.2})$$

This constant is chosen to satisfy:

$$\int SR_{real}G_{c,ASTM}d\lambda = \int SR_{modeled}G_{c,ASTM}d\lambda \quad (D.4.3)$$

$$\iff \alpha \int SR_{ideal}G_{c,ASTM}d\lambda = J_{SC,STC} \quad (D.4.4)$$

such that the density current is correctly computed with the cell-impacting irradiance resulting from an incoming ASTM reference spectra in the plane-of-array.

The constant can therefore be deduced thanks to the STC conditions following :

$$\alpha = \frac{J_{SC,STC}}{\int SR_{ideal}G_{c,ASTM}d\lambda} \quad (D.4.5)$$

This constant remains however dependent on the module considered, as the ideal spectral response relies on λ_{gap} which is technology-specific, and $J_{SC,STC}$ is specified by the manufacturer for a given module.

D.4.0.2 Reference spectrum incident to the cell

The calculation of the corrected quantum efficiency (or spectral response) requires the cell-impacting irradiance under STC, the cell-impacting irradiance being the POA irradiance after applying the optical losses. Yet, the provided ASTM G173-03 spectrum corresponds to the POA irradiance. As the optical losses depend on the nature of the radiation (direct, diffuse or ground-reflected) an optical loss cannot be directly determined for the POA irradiance. Consequently, the MODTRAN equivalent spectrum for STC is used to compute the overall optical losses in STC which is then applied to the ASTM G173-03 spectrum.

D.5 Photocurrent

Given the definition of the spectral response as well as the the short-circuit current temperature coefficient, the short-circuit current for various irradiances and temperatures is computed thanks to:

$$I_{SC} = \left[\int SR_{modeled}(\lambda)G(\lambda)d\lambda \right] \cdot (1 + C_{T,I_{SC}} \cdot (T_c - T_{c,STC})) \quad (D.5.1)$$

D.6 Operating power

D.6.1 Computing V_{OC} for different temperatures and irradiances to STC conditions

Applying (2.2.5) for V_{OC} (*i.e.* $I = 0$), one gets:

$$V_{OC} = V_t \ln \left(\frac{I_{SC}}{I_0} \right) \quad (D.6.1)$$

meaning there is a logarithmic relationship between V_{OC} and the short-circuit irradiance (or photocurrent) thus linking it to the irradiance. Yet, the open-circuit voltage is mainly dependent on the cell temperature due to the thermal voltage term.

D.6.1.1 A simple approach

A first simple approach consists in translating the V_{OC} from STC to the operating conditions by varying the incoming irradiance then the temperature.

First, the open-circuit voltage is expressed for a change in incoming irradiance at a fixed temperature. Then, one gets from (D.6.1)

$$I_0(G_{c,STC}, T_{c,STC}) = I_{SC,STC} \exp\left(-\frac{V_{OC,STC}}{V_t,STC}\right) \quad (D.6.2)$$

leading to

$$V_{OC}(G_c, T_{c,STC}, I_{SC}) = V_{OC,STC} + V_t(T_{c,STC}) \ln\left(\frac{I_{SC}}{I_{SC,STC}}\right) \quad (D.6.3)$$

with G_c the irradiance impacting the cell, which directly influences the photocurrent.

One can then apply the open-circuit voltage temperature coefficient to consider the change in temperature. The expression for V_{OC} thus follows:

$$V_{OC}(G_c, T_c) = \left(V_{OC,STC} + V_t(T_{c,STC}) \left(\frac{I_{SC}}{I_{SC,STC}} \right) \right) \cdot (1 + C_{T,V_{OC}} \cdot (T_c - T_{c,STC})) \quad (D.6.4)$$

D.6.1.2 A more physical approach

A second approach consists in understanding physically where the temperature dependence arises from I_0 . I_0 is highly sensitive to temperature, and [Singh & Ravindra \(2012\)](#) recalls that it can be expressed according to :

$$I_0(T_c) = CT_c^3 \cdot \exp\left(-\frac{E_g}{nkT_c}\right) \quad (D.6.5)$$

with C a constant. The constant factor C for a given module can be computed thanks to the characteristics at STC conditions in (D.6.5) and (D.6.1) yielding:

$$C = I_{SC,STC} \left(\frac{1}{T_{c,STC}} \right)^3 \exp\left(\frac{\frac{E_g}{q} - V_{OC,STC}}{V_t(T_{c,STC})}\right) \quad (D.6.6)$$

Neglecting the change in energy-gap with temperature, I_0 can be computed thanks to:

$$I_0(T_c) = I_{SC,STC} \exp\left(-\frac{V_{OC,STC}}{V_t(T_{c,STC})}\right) \cdot \left(\frac{T_c}{T_{c,STC}}\right)^3 \cdot \exp\left(\frac{E_g}{q} \cdot \left(\frac{1}{V_t(T_{c,STC})} - \frac{1}{V_t(T_c)}\right)\right) \quad (D.6.7)$$

The open-circuit voltage can then be computed by inserting D.6.7 in

$$V_{OC}(G_c, T_c) = V_t(T_c) \ln\left(\frac{I_{SC}(G_c, T_c)}{I_0(T_c)}\right) \quad (D.6.8)$$

D.6.2 Fill factor

[Green \(1982\)](#) presents several analytical expressions for solar cell fill factors as well as their accuracy.

D.6.2.1 Available methods

Neglecting the shunt and series resistance When the shunt and series resistance are negligible, the ideal fill factor FF can be computed thanks to:

$$FF_0 = \frac{v_{OC} - \ln(v_{OC} + 0.72)}{v_{OC} + 1} \quad (D.6.9)$$

with $v_{OC} = \frac{V_{OC}}{V_t}$. For $v_{OC} > 10$ this expression is accurate to the fourth decimal.

Neglecting the shunt resistance The fill factor decreases with series resistance. When the series resistance R_s is not neglected, the fill factor can be deduced from the ideal fill factor FF_0 following

$$FF_s = FF_0 \cdot (1 - r_s) \quad (D.6.10)$$

with r_s the normalized series resistance: $r_s = \frac{R_s}{V_{OC}/I_{SC}}$.

The expression (D.6.10) is more than 2% accurate for $v_{OC} > 10$ and $r_s < 0.4$. A more complex expression is more accurate, with an error of up to four digits in the third decimal for $v_{OC} > 10$ and $r_s < 0.4$:

$$FF_s = FF_0 \cdot (1 - 1.1r_s) + \frac{r_s^2}{5.4} \quad (D.6.11)$$

Neglecting the series resistance The shunt resistance also decreases the fill factor. When the series resistance is negligible, the fill factor can be approximated with the normalised shunt resistance $r_{sh} = \frac{R_{sh}}{V_{OC}/I_{SC}}$, accurate to the third decimal for $v_{OC} > 10$ and $r_{sh} > 2.5$:

$$FF_{sh} = FF_0 \cdot \left(1 - \frac{v_{OC} + 0.7 FF_0}{v_{OC} r_{sh}}\right) \quad (D.6.12)$$

Neglecting neither the shunt resistance nor the series resistance Eventually, if both shunt and series resistance are to be accounted for, the fill factor an accuracy better than a few percent can be achieved following:

$$FF = FF_s \cdot \left(1 - \frac{v_{OC} + 0.7 FF_s}{v_{OC} r_{sh}}\right) \quad (D.6.13)$$

providing $v_{OC} > 10$ and $r_s + \frac{1}{r_{sh}} < 0.4$

D.6.2.2 Chosen methods

In the photovoltaic model, the shunt resistance is neglected, such that only the two formulations (D.6.10) and (D.6.11), hereafter named “simple” and “complex”, are currently implement.

D.7 Series resistance

The series resistance R_s is required to compute the fill factor, as mentioned in the previous part. As a first approximation, the series resistance is assumed constant, meaning that R_s can be retrieved from a known value of FF by inverting the [Green \(1982\)](#) model used, that is to say by inverting (D.6.10):

$$R_s = \left(1 - \frac{FF_{STC}}{FF_{0,STC}}\right) \frac{V_{OC,STC}}{I_{SC,STC}} \quad (D.7.1)$$

or by considering the roots of (D.6.11) in the STC.

This method can be applied as the fill factor is known in STC thanks to the $I_{SC,STC}, V_{OC,STC}$ and $P_{MPP,STC}$ provided by the manufacturer datasheet, given the definition of the fill factor (2.2.8):

$$FF_{STC} = \frac{P_{MPP,STC}}{I_{SC,STC} \times V_{OC,STC}} \quad (D.7.2)$$

D.8 Overview

To summarize, the Figure D.8.1 provides an overview of the photovoltaic model and its sub-components.

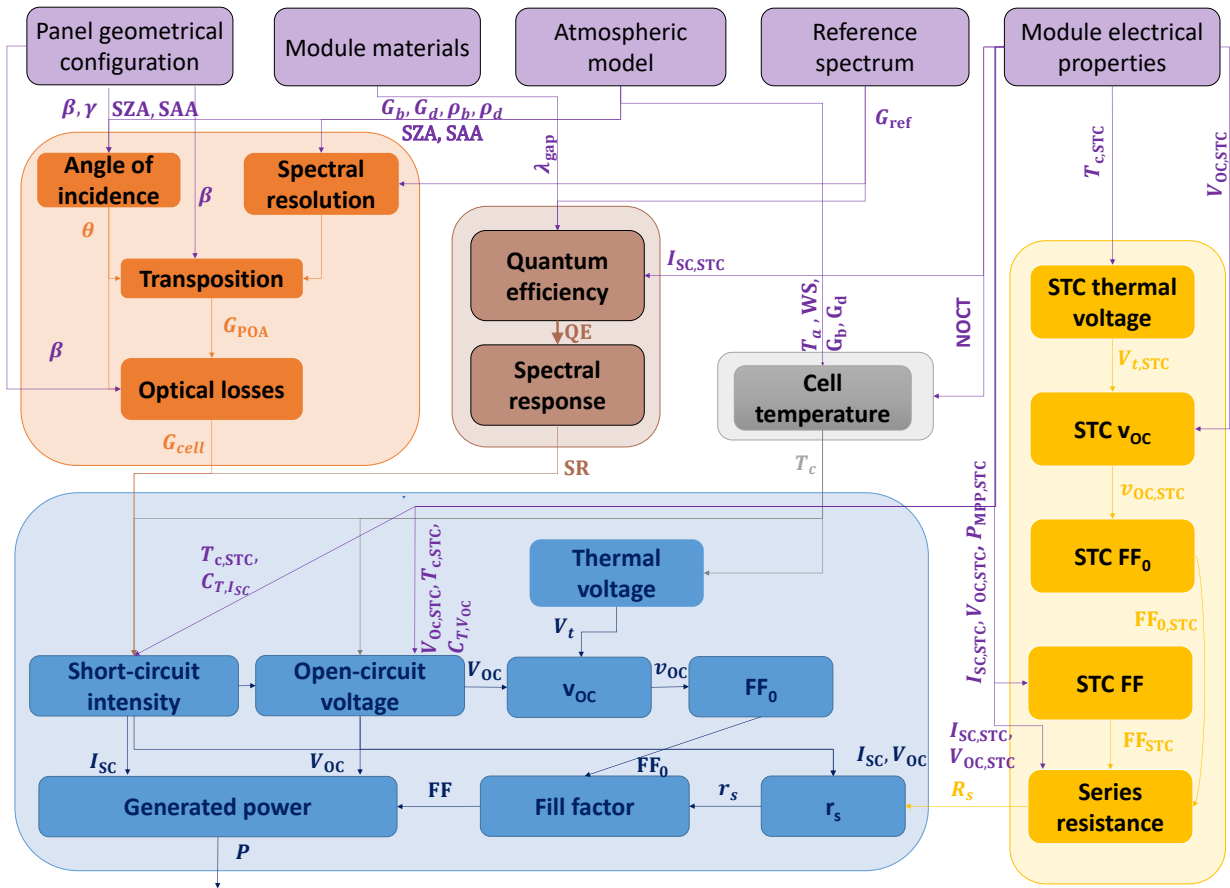


Figure D.8.1: Detailed diagram of the PV code

APPENDIX E

FURTHER INTO THE VALIDATION OF CELL TEMPERATURE MODELS

E.1 Converting wind speeds for the King model

Figure E.1.1 illustrates the influence of the α exponent for the wind speed power law chosen on the modelled module temperature. If the model had no biases, the optimised exponent should correspond to the physical α . Consequently, the optimised exponent should be independent to the chosen PV module. Table E.1.1¹ shows that the optimised exponent greatly depends on the module. Consequently, no correction is applied ($\alpha = 0$).

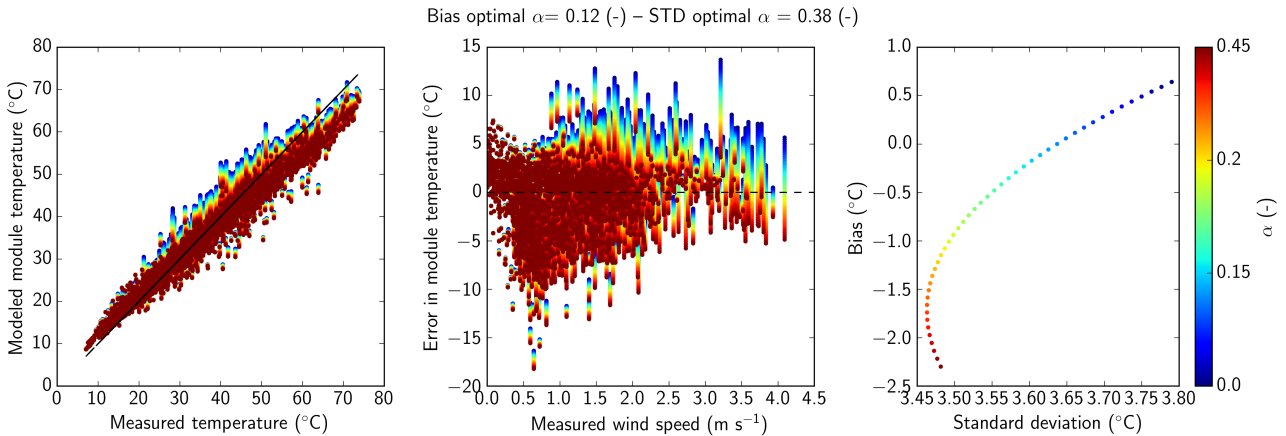


Figure E.1.1: Modeled module temperature for different values of α and corresponding bias and standard deviation.

Table E.1.1: Optimised α for the different modules, based on the optimisation criteria (bias or standard deviation).

	Optimised α (-)	
	Bias	Standard deviation
First Solar	0.00	0.28
France Watts	0.12	0.21
Panasonic	0.0	0.41
Sharp	0.25	0.45

¹The error in temperature modelling is too important for the Panasonic module such that no correction provides the best fit

E.2 Adapting the NOCT for the Skoplaki model

The Skoplaki model requires the NOCT, which is provided by the manufacturer (and a certain uncertainty) or is unknown (France Watts). NOCTs are generally between 44 and 47°C.

Figure E.2.1 provides a sensitivity analysis of the modelled cell temperature for the France Watts module (and guessed NOCT = 45 °C). Figure E.2.1 shows that the modelled temperature with Skoplaki model is sensitive to the NOCT and underlines the importance of this parameter for precise modelling.

The optimised value for the unknown France Watt NOCT is 53 – 54 °C, the resulting errors (illustrated in Figure E.2.2) are small compared to the original assumption. However, this NOCT is unexpected since it is high compared to typical values.

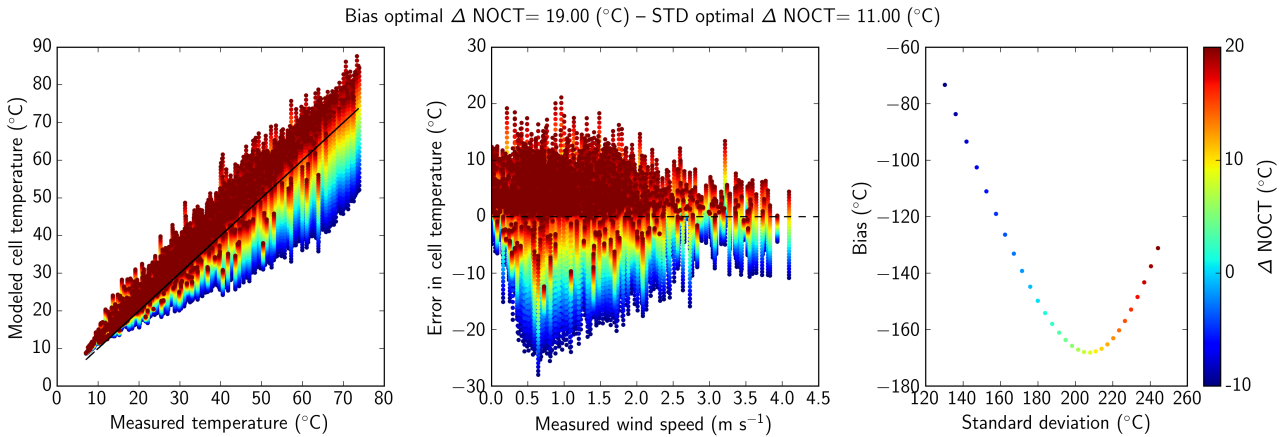


Figure E.2.1: Errors in cell temperature modelling using Skoplaki 2 model over a range of NOCTs.

An analysis of optimal $\Delta\text{NOCT} = \text{NOCT}_{\text{optimal}} - \text{NOCT}$ has been undertaken for all four modules, in order to understand if this difference is intrinsic to the model. Table E.2.1 shows the optimal ΔNOCT for all four technologies based on a minimal bias or standard deviation. Considering the differences, this correction is not justified by the model. Consequently, no correction of NOCT shall be applied in the future.

Table E.2.1: Optimised ΔNOCT for the different modules, based on the optimisation criteria (bias or standard deviation).

	Optimised ΔNOCT (°C)	
	Bias	Standard deviation
First Solar	7	5
France Watts	8	9
Panasonic	19	1
Sharp	5	5

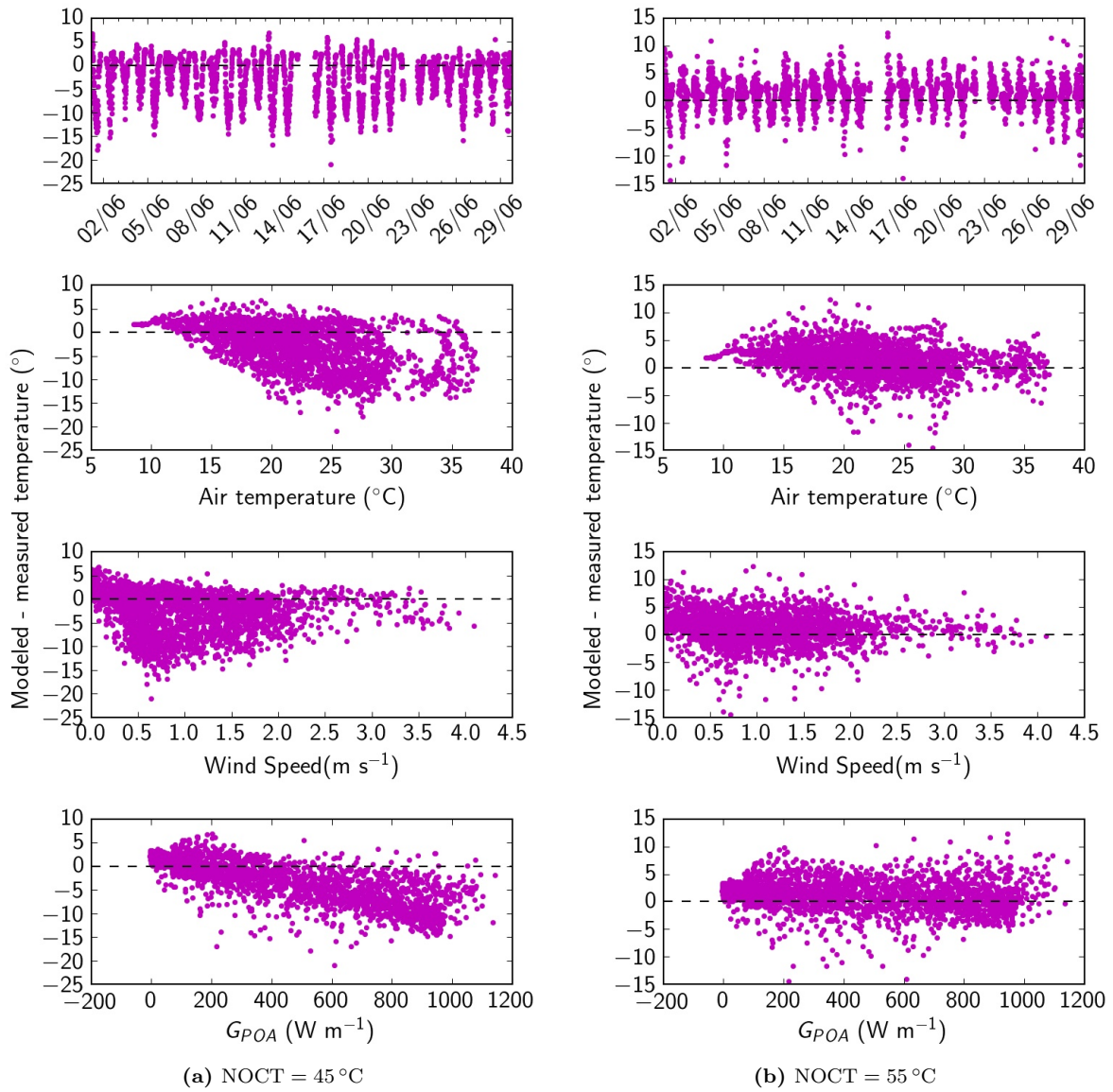


Figure E.2.2: Errors in cell temperature modelling using Skoplaki 2 model, without (a) or with (b) $\Delta NOCT = 10\text{ }^{\circ}\text{C}$